Retrieval of equivalent currents by the use of an integral representation and the extinction theorem --- radome applications

Persson, Kristin

2010

Licentiate dissertation

Retrieval of equivalent currents by the use of an integral representation and the extinction theorem — radome applications

Kristin Persson

Retrieval of equivalent currents by the use of an integral representation and the extinction theorem — radome applications

Kristin Persson

Licentiate Dissertation
Electromagnetic Theory

Lund University
Lund, Sweden
2010

Abstract

The aim of this thesis is to solve an inverse source problem. The approach is based on an integral representation together with the extinction theorem. Both a scalar and a full-wave integral representation are implemented and solved by a Method of Moment procedure. The body of revolution enables usage of a Fourier transform to reduce the dimensions of the problem. A singular value decomposition is utilized to suppress singular values in the inversion process. A nose-cone radome is diagnosed by recreating the equivalent surface currents on its surface from measured near fields. It is shown how the radome interacts with the field, creating beam deflection, pattern distortion, *etc.*. The phase shift of the field due to the transmission through the radome, *i.e.*, the insertion phase delay, is visualized. Disturbances due to defects, not detectable in the measured near field, are correctly localized by the equivalent surface currents. The alteration of side and flash lobes, together with the introduction of scattering due to the defects, are also visualized. Verification is made by comparison between the calculated and measured far field.

Populärvetenskaplig sammanfattning (in Swedish)

Användningen av elektromagnetiska fält är en naturlig del i det moderna samhället. I vår dagliga miljö är vi beroende av informationen och energin som de elektromagnetiska vågorna transporterar. Som exempel kan nämnas mobiltelefonsamtal, uppvärmning av mat i mikrovågsugnen, användning av internet och radarövervakning på flygplatser.

För att konstruera en antenn så att korrekta fält sänds ut är det viktigt att kunna studera det elektromagnetiska fältets utseende på antennytan. En sådan studie kan peka på var felaktigheter är lokaliserade samt hjälpa till att optimera antennen. Fälten på ytan kan inte direkt mätas upp. Ett sådant försök resulterar i mätfel pga. växelverkan mellan antennen och mätproben. Istället mäts fältet upp en bit bort från antennen och beräkningar görs för att bestämma hur källorna, det vill säga fälten på antennytan, ser ut. Detta är ett inverst källproblem.

I denna avhandling löses det inversa källproblemet med hjälp av en integralrepresentation tillsammans med utsläckningssatsen (eng. extinction theorem). Implementeringen baseras på en momentkod (eng. Method of Moments). I artikel I–II används en skalär integralrepresentation. I artikel III implementeras en vektorvärd integralrepresentation vilken tar hänsyn till växelverkan mellan fältets komponenter. Det inversa problemet är fel ställt, vilket innebär att små fel i mätdata kan förstärkas och ge upphov till stora felaktiga bidrag i källbeskrivningen. Här minskas denna påverkan genom att använda en singulärvärdesuppdelning (eng. Singular Value Decomposition, SVD) i inverteringsprocessen.

Metoden har använts för att diagnostisera en radom (noskon som skyddar en radarantenn). En reflektorantenn innanför en konformad radom alstrar ett elektromagnetiskt fält. Det elektriska fältet mäts upp på en cylindrisk yta en bit utanför radomen i närfältszonen, vid frekvenserna $8 - 12$ GHz. Tre olika fall har studerats; ingen radom som täcker antennen, radomen på plats, samt en defekt radom placerad över antennen. Det uppmätta elektriska fältet "backas" med hjälp av beräkningar tillbaka till radomytan. Genom att studera tredimensionella bilder av fältkomponenternas amplitud och fas på radomytan, visas hur fältet förändras då radomen är placerad över antennen. Bland annat minskar huvudloben, och sidlober uppkommer. Fasens förändring (eng. Insertion phase delay, IPD) är ett sätt att mäta radomens prestanda vid tillverkning, och här visas en metod som har potential att ersätta den idag vanliga manuella mätningen.

Den defekta radomen har två kopparbitar fastsatta på ytan. När det uppmätta fältet studeras kan man se att något är fel, men inte orsaken till felet. Då fältet "backas" syns defekternas placering tydligt. Man ser även hur kopparbitarna förändrar bakåtloberna, samt att det uppkommer spridningseffekter. Metoden har verifierats genom en jämförelse med uppmätt fjärrfält.

List of included papers

This dissertation consists of a General Introduction and the following scientific papers:

I. K. Persson and M. Gustafsson. Reconstruction of equivalent currents using a near-field data transformation – with radome applications, *Progress in Electromagnetics Research*, vol. 54, pp. 179–198, 2005.

II. K. Persson and M. Gustafsson. Reconstruction of equivalent currents using the scalar surface integral representation, Technical Report LUTEDX/(TEAT-7131), pp. 1–25, 2005, Department of Electrical and Information Technology, Lund University, Sweden. `http://www.eit.lth.se`

III. K. Persson, M. Gustafsson, and G. Kristensson. Reconstruction and visualization of equivalent currents on a radome surface using an integral representation formulation, Technical Report LUTEDX/(TEAT-7184), pp. 1–45, 2010, Department of Electrical and Information Technology, Lund University, Sweden. `http://www.eit.lth.se`[1]

Other publications by the author

IV. K. Persson and M. Gustafsson. Reconstruction of equivalent currents using a near-field data transformation - with radome applications, Technical Report LUTEDX/(TEAT-7125), pp. 1–15, 2004, Department of Electrical and Information Technology, Lund University, Sweden.[2] `http://www.eit.lth.se`

V. K. Persson and M. Gustafsson. Reconstruction of equivalent currents using a near-field data transformation - with radome applications, *Proceedings EMB04*, Computational Electromagnetics - Methods and Applications (EMB 04), Göteborg, Sweden, pp. 124–131, October 18–19, 2004.

VI. K. Persson and M. Gustafsson. Near field to equivalent currents transformation with radome applications, *Proceedings International Symposium on Electromagnetic Theory*, International Symposium on Electromagnetic Theory (URSI EMTS 2004), Pisa, Italy, pp. 1122–1124, May 23–27, 2004.[3]

VII. K. Persson, M. Gustafsson, and G. Kristensson. Experimental validation of reconstructed equivalent currents on a radome, *International Conference on Electromagnetic Near-Field Characterization & Imaging (ICONIC 2005)*, Barcelona, Spain, pp. 35-40, June 8–10, 2005.

---

[1]Submitted for publication.
[2]This report is a longer and more detailed version of the publication in I.
[3]Young Scientist Award.

VIII. K. Persson, M. Gustafsson, and G. Kristensson. Usage of a surface integral representation to reconstruct equivalent currents - with radome applications, *Proceedings of Radiovetenskap och kommunikation*, Nordic Conference on Radio Science and Communications (RVK 05), Linköping, Sweden, June 14–16, 2005.

IX. S. Nordebo, M. Gustafsson, K. Persson. Sensitivity analysis for antenna near-field imaging. *IEEE Transactions on Signal Processing*, vol. 55, no. 1, pp. 94-101, 2007.

Summary of included papers

Paper I - Reconstruction of equivalent currents using a near-field data transformation – with radome applications

This paper shows how the near-field amplitude of a scalar electric field can be reconstructed on a radome surface close to the source of radiation. The method is based on a scalar surface integral representation together with the extinction theorem. The representation describes an inverse source problem with the scalar electric field and its normal derivative on the radome surface as unknowns. The experimental set-up is axially symmetric, such that the complexity of the problem can be reduced by employing a Fourier transform. The linear system is regularized by the singular value decomposition (SVD). The measurement set-up consists of a reflector antenna and a radome. The height of the radome corresponds to 29 wavelength at 8 GHz. The electric near field is measured on a cylindrical surface. Three different configurations are considered in the frequency range $8 - 12$ GHz: no radome, the radome, and the defect radome present. The defect radome has two copper plates attached to its surface. The formulation is first validated for synthetic data and an error estimation is performed. It is then showed that the measured electric field can be reconstructed on the radome surface in an accurate way, where *e.g.*, the copper plates, not seen in the measured near field, are detected. The used technique is also verified by comparing the far field, calculated from the reconstructed fields, to measured far field.
The author of this dissertation has carried out most of the analysis, and she is responsible for the numerical simulations, and the writing of the paper.

Paper II - Reconstruction of equivalent currents using the scalar surface integral representation

This paper is a continuation of Paper I in the sense that the numerical analysis of the radome is investigated further. The phase of the electric field is taken into account. The phase delay caused by the radome, referred to as insertion phase delay (IPD), is studied. It is also shown that the manufacturing errors, not shown in the measured near-field data, can be focused and detected by reconstructing the phase shift due to the propagation though the radome. Different ways of visualizing the results are also discussed and presented in order to show which knowledge that can be extracted from the measured near field.
The author of this dissertation has carried out most of the analysis, and she is responsible for the numerical simulations, and the writing of the paper.

Paper III - Reconstruction and visualization of equivalent currents on a radome surface using an integral representation formulation

In this paper, the inverse source problem is solved by utilizing a vector-valued integral representation combined with a vector-valued integral equation originating from the extinction theorem. The coupling between the components of the fields increases the complexity of the problem. The problem is solved in a similar way as the scalar case, *i.e.*, the integral representation and equation are written as linear systems and solved by a Method of Moment approach. An SVD is employed to invert the matrices and the singular values are suppressed to regularize the problem. The three radome configurations are investigated at $8\,\mathrm{GHz}$, and all components of the measured field are now analyzed, *i.e.*, both co- and cross components of the equivalent currents are reconstructed. It is shown in what way the radome changes the radiation pattern and causes the main lobe to deflect. The copper plates attached to the radome alter the measured electric field. However, the cause of the distortion is not seen in the near field. Here, it is shown that both components of the magnetic equivalent current can be used to localize these effects. The influence of the radome on the phase of the field, *i.e.*, the IPD, is also investigated. A calculation of the thickness of the radome wall from the calculated IPD verifies the results. The results in this paper show that the method is promising and can eventually be employed for industrial use.

The author of this dissertation has carried out most of the analysis, and she is responsible for the numerical simulations in parts, and the writing of the paper.

Acknowledgments

Contents

General Introduction

Kristin Persson
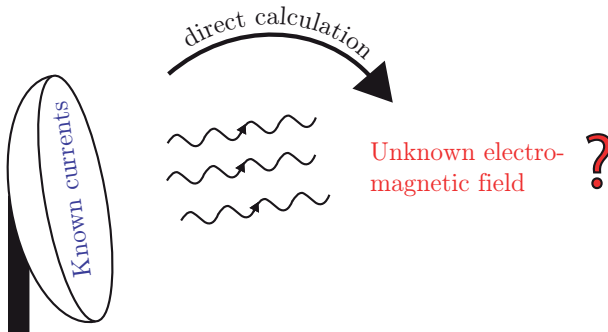
Figure 1: A direct source problem.

1   Introduction

Radiation means that energy is emitted by a radiating body, *e.g.*, an antenna. The energy then propagates out in the surrounding medium. The cause of the radiation are currents on the radiator.

In a direct problem, see Figure 1, the sources are given and the currents are known. The goal is to calculate the radiated field in the media surrounding the radiator. This problem is well understood but often computationally challenging [8]. The result is uniquely determined [43], which means that if the currents are known, the electromagnetic field can be expressed in one unique way.

The aim of this thesis is to solve the inverse source problem — to find the sources of a given electromagnetic field. In the inverse problem, the electromagnetic field is known on a surface some distance away from the radiating body, see Figure 2. The cause of the radiation is unknown, *i.e.*, the challenge is to reconstruct the currents on the radiator or on a surface surrounding it. The inverse source problem is not uniquely determined, since adding a non-radiating source/current does not modify the electric and magnetic fields on the measurement surface [18, 38, 42, 64, 69]. That is, one cannot claim that all sources/currents are found since there might be components that do not contribute to the measured field. Another problem with the inverse source problem is that a small perturbation in the measured field can cause large inaccuracies in the reconstructed currents.

In order to give an understanding of the problem, how it is solved, the application areas, and the interesting interpretations of the results, the sections below are arranged as follows; Section 2 points out the reasons for the interest in the inverse source problem by identifying different areas of applications. The work of other researchers within the area and some of their applications are covered in Section 3. Section 4 describes the method where an integral representation is combined with the extinction theorem, which is the basis for this thesis. The details of this derivation are found in Appendix A. Finally, future challenges and conclusions are discussed in Section 5.
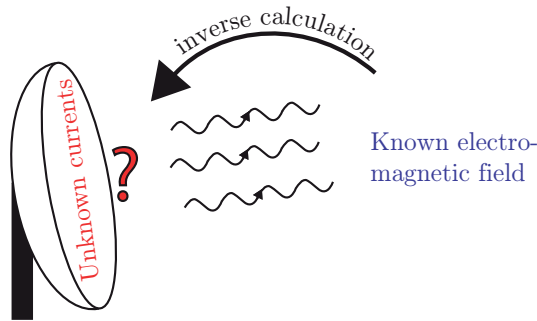
Figure 2: An inverse source problem.

2   Applications

The currents, describing the source of the radiation, can serve as an instrument of diagnostics. For example, antennas need to be diagnosed to find malfunctioning parts. In wireless communication, it is important to have tools to specify the radiation of mobile phones and the safety distance of base stations' antennas. Another example is electronic equipment interacting with other electronic devices — the electromagnetic compatibility problem (EMC). To minimize this interaction and to find out shielding strategies, the sources must be known.

A radome is a structure designed to protect its enclosed antenna against environmental effects, see Figure 3. A review of the radome concept can be found in [51]. For instance, the nose cone of an airplane covers its radar antenna. Other places where radomes protect radiating equipment are on high towers, on board ships, in surveillance bases *etc.*. The radome will inevitable interact and change the field radiated by the antenna in unwanted ways, *e.g.*, creation of high side lobes causes increased clutter, false-alarm rate and susceptibility to jamming. Moreover, the main lobe is deflected (boresight error) and attenuated, whereas reflections cause interferometry phase errors. In order to analyze and minimize these disturbances, *i.e.*, to make the radome as transparent as possible at the operating frequencies, it is of great importance to diagnose how the electromagnetic fields interact with the radome.

It is also significant to have a powerful tool to determine the insertion phase delay (IPD), also known as the electrical thickness of the radome. The IPD is one of the specified qualities that characterize a radome. It is traditionally measured by locating two horn antennas in such a way that the incident angle of the field becomes the Brewster angle. This choice of incident angle minimizes the reflected field, *i.e.*, the disturbances due to back scattering into the radiating horn antenna are reduced [17, 52]. To calculate the IPD, the phase of the transmitted field is subtracted by the phase of the measured field with no radome present between the horn antennas. This process is very time consuming, since it has to be repeated
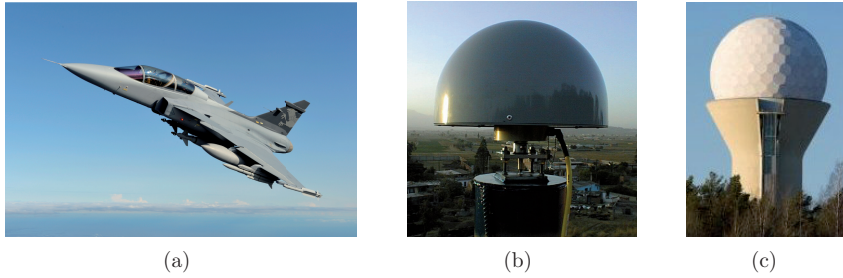
Figure 3: Different radome applications: a) Aeroplane. Copyright Gripen International. Photo: Katsuhiko Tokunaga. b) Station monitoring tectonic motions of the volcano Popocatepetl in Mexico. Photo courtesy of Enrique Cabral-Cano. c) Aircraft surveillance, Bromma airport, Sweden. Photo courtesy of Maciej Swic.

several times to cover the whole radome surface.

Another crucial utilization is within the design process of a radome. This task includes numerical calculations of the alteration of the electric field as it passes through the radome wall [4, 5, 57]. To get reliable results it is crucial that the representation of the field radiated from the antenna, *i.e.*, the input data, is well known. This field cannot be measured directly, since it is very difficult to measure the electromagnetic fields close to a radiating body or scatterer. The reason is that the measurement probe itself can interact with the measured field and contaminate the measurement.

3   Solution methodologies

The inverse source problem attracts a lot of attention. The main difference between the various techniques depends on the geometry of the surface where the field is measured, and the geometry of the body where the fields are to be reconstructed. The material of the body of the equivalent currents also differs. The most common ones are the perfect magnetic conductor (PMC), the perfect electric conductor (PEC), or air. Some methods require *a priori* information of the object, and some use iterative solvers. Also, the demand for computer capacity differs among the techniques. The following paragraphs give a overview of different approaches and their usage.

3.1   Plane wave spectrum

One of the first techniques developed and a numerically fast method is the use of the plane wave spectrum (PWS) [10, 16, 23, 25, 44, 71]. This technique expands the measured field in plane waves. The PWS is equal to the Fourier transformation of the radiated far field. The near field on a plane, arbitrarily close to the antenna, can then be obtained through an inverse Fourier transform. Both spherical and planar

measurement surfaces can be used as well as measurements in the near field or in the far field, since accurate transformations between the different geometries and the fields are available [11].

The PWS has been used to determine the specific absorption rate (SAR) of mobile phones [21]. Instead of scanning the electric field strength in the whole volume of the phantom, it is enough to measure the amplitude of the electric field on two planes. The phase of the electric field is retrieved by an iterative process [74] and the expansion of the field in its plane wave spectrum is utilized to evaluate the electric field and thereby the SAR on other planes in the phantom. The method has also been utilized to localize defects, *i.e.*, patches of Eccosorb attached to a planar array [37]. Another application is the reconstruction of the near field on the surface of a parabolic antenna where an iterative scheme and certain approximations make it possible to find the fields on the non-planar surface [53–55].

3.2   Modal expansion

A modal expansion of the field can be utilized if the reconstruction surface is cylindrical or spherical [24, 40]. The field is then described as a sum of cylindrical or spherical vector waves. The radial part of the expansion is expressed in cylindrical or spherical Bessel functions, respectively. The angular part contains trigonometric functions, and in the spherical case Associated Legendre functions [70]. The resolution obtained with spherical wave expansion (SWE) can be higher than the resolution achieved when using plane wave spectrum [22]. However, the method is only valid outside the smallest sphere enclosing the radiating body, *i.e.*, equivalent currents on the radiating body cannot be obtained unless the body is a sphere. This method has been used to calculate the insertion phase delay (IPD) and detect defects, *i.e.*, deviations in the dielectric constant and wall thickness on a spherical radome [22].

The SWE has also been employed in antenna near-field imaging problems to find the relation between accuracy and resolution [45, 46]. The Cramér-Rao bound gives a lower bound on the estimation error and a fundamental physical limit on system accuracy. This bound is related, via the Fisher information matrix [28], to the resolution as a function of the number of vector waves included [45]. The mathematical frame-work is applied to an electric field, measured on a cylindrical surface, and it is shown in which regions the result is trustworthy.

In [41] the authors have investigated how constraints, *e.g.*, zero reactive power, in a Lagrangian formulation, can optimize the spherical vector wave technique. More general geometries, *e.g.*, needle shaped objects and flat disks, can be handled by expanding the field in spheroidal wave functions [61, 62]. As with the spherical vector waves, the solution is only valid outside the smallest spheroid enclosing the radiating body. Also, the Lagrangian optimization approach with constraints are developed for this expansion [63].

A combination of SWE and PWE (plane wave expansion) has been employed by [13]. The electric field of a spherical near-field measurement is expanded in spherical vector waves. Utilizing an extended transform of [19], the field is expressed

in its plane wave spectrum, whereby the field on a plane close to the origin can be retrieved through an inverse fast Fourier transform. The method combines the high resolution of SWE with the ability to come very close to the antenna under test provided by PWE. This diagnostic technique is demonstrated by introducing errors, *i.e.*, feed tilt, Gaussian shaped metallic bump, and dishes of aluminum, on an offset reflector antenna. These deviations can then be found in the recreated field on a plane surface just in front of the antenna [14].

Another combination of modal expansion and PWE is utilized by [76], where the safety perimeter of base station antennas is investigated. The electric field is measured on a cylindrical surface, it is expanded in cylindrical vector waves and the far field is calculated. The far field is then expanded in PWS and the field on different planes close to the antenna is retrieved. This approach does not take the presence of the reactive near field into account, since this is negligible at the safety distances of interest.

3.3   Integral representations

To be able to handle a wider class of geometries, diagnostic techniques based on integral equations to describe the electromagnetic field can be utilized, *i.e.*, a linear inverse source problem is solved by a method of moment (MoM) approach. The drawback is the computational complexity. The equivalent currents of the source are recreated on a surface arbitrarily close to the source.

If the object on which the currents are to be reconstructed is metallic, *i.e.*, a perfect electric conductor (PEC), either the electric or magnetic field integral equation (EFIE or MFIE) can be employed. The methods differ by the field used as the source term — the electric field in EFIE, and the magnetic field in MFIE, respectively. MFIE only applies to closed surfaces whereas EFIE can be used for both open and closed surfaces. The EFIE has been employed in [67] to calculate the near field of a cylindrical PEC via the surface currents. The PEC also has aperture holes of various sizes to show how to find and diagnose leakage points in metallic objects, *i.e.*, wires.

Both EFIE and MFIE have problems with spurious resonances. However, this effect can be reduced by using a combination of the two, *i.e.*, the combined field integral equation (CFIE), since the resonances of EFIE differ from the ones of MFIE [9, 47]. A description of other used combinations are found in *e.g.*, [30]. Yet another approach to avoid spurious resonances was proposed in [68, 72]. Here the MFIE is combined with an integral equation where the source term is located on an imaginary dual surface inside the scatterer. One advantage of this method over the CFIE is that the use of both the operators of the EFIE and MFIE is avoided. The dual-surface EFIE and MFIE are employed to recreate surface currents on a PEC of cubic or azimuthal geometry [58, 59, 73].

Even if the surface where the reconstructed currents are calculated is not a PEC, the above methods, *i.e.*, EFIE and MFIE, can be employed by using an equivalence principle where the volume inside the surface containing the sources is replaced by a PEC or a PMC (perfect magnetic conductor) [8]. This approach

has been used by [33, 35, 48, 49, 56, 66], where the equivalent currents, either the magnetic or electric, are reconstructed on a plane in front of the antenna from near-field measurements over arbitrary geometries. This technique is convenient when diagnosing flat antenna structures, *e.g.*, in [36], where an equivalent magnetic current together with *a priori* knowledge of the antennas geometry is utilized to diagnose a low-directivity printed antenna. In [26], the technique together with an iterative solver based on the conjugate gradient method, is used to diagnose radiated noise on a plane over a power electronic circuit. A development of this method is given in [34] where the antenna is enclosed by two infinite planes, one in front of the antenna and one on its back, on which the magnetic equivalent current is recreated. This technique is used to find the safety perimeter of a base station antenna by recreating the radiating field on planes at various distances in front of and behind the antenna. In [75] the radiation pattern from superspheroidally shaped dielectric radomes enclosing dipole arrays is calculated using the equivalence principle to get a combined integral equation, which is solved by an adaptive integral solver. Further references within the area are given in [39], where a volume integral equation is utilized.

An integral representation, relating both the unknowns, *i.e.*, the electric and magnetic currents, to the measured electric field, is used together with the additional condition that the normal component of the surface currents are zero in [1, 3]. The linear equation system is solved by the conjugate gradient method. In [3], the electric current on the walls of a PEC, pyramidal horn antenna, is visualized. Under certain circumstances, such that reconstruction on planar surfaces or bodies of PEC, only one of the currents needs to be taken into account. This simplification is used in [32] where defect elements in antenna arrays and irregularities in the surface of a reflector antenna are detected. Also, [20] solves an integral representation using fast multipoles and an iterative solver based on generalized minimal residual (GMRES). The electric equivalent current is reconstructed on PEC plane in front of a reflector antenna and a monopole located on the chassis of a car. Even other optimization techniques have been proposed to solve the problem. In [6, 7] neural networks are used, and in [2] a cost function is introduced to find the location of EM transmitters. Further references in this subject can be found in [12].

4   Integral representation and extinction theorem

In this thesis a technique using the integral representations to relate the unknown equivalent currents to a known measured near field is proposed. In addition to the integral representation, an integral equation, originating from the extinction theorem, is used. The use of the the extinction theorem together with the integral representation guaranties that the sources of the reconstructed currents only exist inside the enclosing volume, see Paper I-III. The equivalent currents can be reconstructed on a surface arbitrarily close to the antenna. No *a priori* information of the material just inside the surface is utilized.

The aim is to recreate the equivalent currents on a radome-shaped surface from
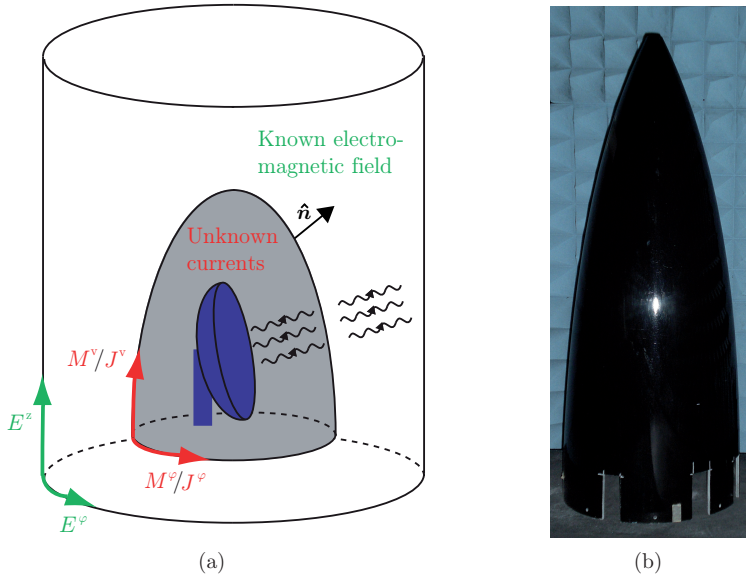
Figure 4: a) The set-up showing the reflector antenna, the radome, and the cylindrical surface. b) The radome used in the measurements. The missing pieces at the bottom have been used for material characterization.

measured electric near field collected on a cylindrical surface. The equivalent currents are the tangential components of the electric and magnetic fields on the radome surface [8], *i.e.*,

$$\begin{cases} \boldsymbol{J} = \hat{\boldsymbol{n}} \times \boldsymbol{H} \\ \boldsymbol{M} = -\,\hat{\boldsymbol{n}} \times \boldsymbol{E} \end{cases} \tag{4.1}$$

where $\boldsymbol{J}$ is the electric current, $\boldsymbol{M}$ is the magnetic current, $\boldsymbol{E}$ is the electric field, $\boldsymbol{H}$ is the magnetic field, and $\hat{\boldsymbol{n}}$ is the outward pointing unit vector. Figure 4a depicts the set-up, and Figure 4b shows a photo of the radome used in the measurements. The equivalent currents and the electric field are parametrized into one component along the height (J^{v}, M^{v}, E^{z}) and one azimuthal component (J^{φ}, M^{φ}, E^{φ}). The radiation from the antenna interacts with the radome. This interaction is visualized by recreating the equivalent currents on the radome surface.

In Paper I, a scalar integral representation is derived. One integral representation relates the unknown currents to the measured near-field data. The extinction theorem gives a second equation, stating that the integral is zero if the observation point lies on a surface inside the radome. The scalar approach is relevant since the co-component, *i.e.*, E^{z}, dominates in the measured field. The system of equations are solved by a Method of Moments (MoM) procedure. The radome and the measurement surface have azimuthal symmetry, *i.e.*, a Fourier transform can be employed to decouple the equations and to reduce the computational complexity.

A singular value decomposition (SVD) is used to invert and regularize the matrix, *i.e.*, remove singular values below a cut off level. The code is verified by using synthetic data, where the error is shown to be below $-60\,\mathrm{dB}$. Measured near-field data, originating from a reflector antenna, and collected on a cylindrical surface is then investigated. Three different configurations are studied, one with just the antenna, one with a radome enclosing the antenna, and finally one where a defect radome is placed over the antenna. The amplitude of the reconstructed currents are visualized in the frequency range $8 - 12\,\mathrm{GHz}$, revealing diffraction effects. Introduced defects on the radome, *i.e.*, copper plates, not visible in the near field data are localized in the equivalent currents. The results are verified by calculating the far field from the reconstructed currents. This far-field pattern agrees very well with measurements.

The aim in Paper II is to obtain the phase of the reconstructed currents, *e.g.*, the insertion phase delay (IPD). The phase of the recreated currents is visualized and analyzed in the frequency range $8 - 12\,\mathrm{GHz}$. The thickness of the radome wall is approximated in order to validate the calculated phase shift. Different ways of visualizing the amplitude and phase of the equivalent currents are also discussed and presented in order to show which knowledge that can be extracted from the measured near field.

In Paper III the analysis is derived for the full-wave electric field, *i.e.*, the cross component are no longer assumed to be negligible. The integral representation is evaluated at the radome surface instead of on a surface inside the radome which gives a classical integral equation. That is, an integral equation that relates the unknown equivalent currents to each other on the radome surface, *i.e.*,

$$\hat{\boldsymbol{n}}(\boldsymbol{r}) \times \iint\limits_{S_{\mathrm{radome}}} \left\{ \mathrm{j}\omega\mu_0 \; g(\boldsymbol{r}',\boldsymbol{r})\boldsymbol{J}(\boldsymbol{r}') - \mathrm{j}\frac{1}{\omega\epsilon_0} \; \nabla'g(\boldsymbol{r}',\boldsymbol{r})\big[\nabla'_S \cdot \boldsymbol{J}(\boldsymbol{r}')\big] \right.$$
$$\left. - \nabla'g(\boldsymbol{r}',\boldsymbol{r}) \times \boldsymbol{M}(\boldsymbol{r}') \right\} \, \mathrm{d}S' = \frac{1}{2}\,\boldsymbol{M}(\boldsymbol{r}) \qquad \boldsymbol{r} \in S_{\mathrm{radome}}$$

where $g(\boldsymbol{r}',\boldsymbol{r})$ is the free space Green's function, $\hat{\boldsymbol{n}}$ is the outward pointing normal of the radome surface, and ∇_S is the surface divergence [15]. When necessary, the integrals are interpreted as Cauchy's principal value [15, 50]. The integral representation relates, as before, the equivalent currents to the measured near field, *i.e.*,

$$\iint\limits_{S_{\mathrm{radome}}} \left\{ -\mathrm{j}\omega\mu_0 \; g(\boldsymbol{r}',\boldsymbol{r})\boldsymbol{J}(\boldsymbol{r}') + \mathrm{j}\frac{1}{\omega\epsilon_0} \; \nabla'g(\boldsymbol{r}',\boldsymbol{r})\big[\nabla'_S \cdot \boldsymbol{J}(\boldsymbol{r}')\big] \right.$$
$$\left. + \nabla'g(\boldsymbol{r}',\boldsymbol{r}) \times \boldsymbol{M}(\boldsymbol{r}') \right\} \, \mathrm{d}S' = \boldsymbol{E}(\boldsymbol{r}) \qquad \boldsymbol{r} \text{ outside } S_{\mathrm{radome}}$$

The approach of solution is the same as in Paper I-II. However, the expressions now contain coupled vector-valued fields and singular integrals. A detailed derivation of the representations is found in Appendix A.

The equivalent magnetic current is investigated at $8\,\mathrm{GHz}$, see Figures 5 and 6. In Paper III the diffraction and transmission losses caused by the radome and the
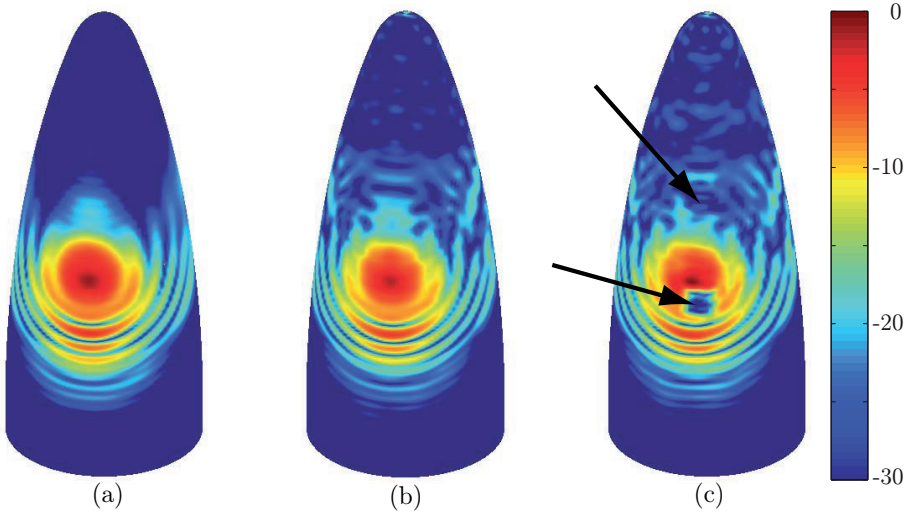
Figure 5: The recreated $|M^\varphi|$-component on the front side of the radome. All values are normalized with the largest value of $|M^\varphi|$ when the defect radome is present and shown in dB-scale. (a) No radome present. (b) Radome present. (c) Defect radome present. The arrows point out the locations of the copper plates.

defect radome are depicted for both the co- and cross-polarized component. Also flash lobes caused by the radome are visualized. The effects of the defects, *i.e.*, copper plates, are localized in both the amplitude and phase components. However, to get the exact positions a combination of all components need to be analyzed. The results are verified by a comparison with the scalar code in Paper I. The results agree very well considering the cross-component is assumed to be zero in the scalar code. The phase shift due to the radome, *i.e.*, the IPD, is visualized and the results are promising which might lead to an alternative way of diagnosing radomes in the future.

5   General conclusions and future challenges

This thesis shows the potentials of the integral representation and the extinction theorem in solving the inverse source problem. In Paper I-II, the scalar representation is explored. In Paper III, the vector-valued representation is investigated by visualizing the reconstructed equivalent magnetic current on a radome surface. Future challenges are to analyze if also the electric equivalent current on the radome surface can contribute to more knowledge. Moreover, investigation of the frequency dependence of the radome, using the full-wave representation, is planned. A closely related question is the resolution of the equivalent currents. An initial investigation of this work is found in [45], where the problem is solved with spherical vector waves.
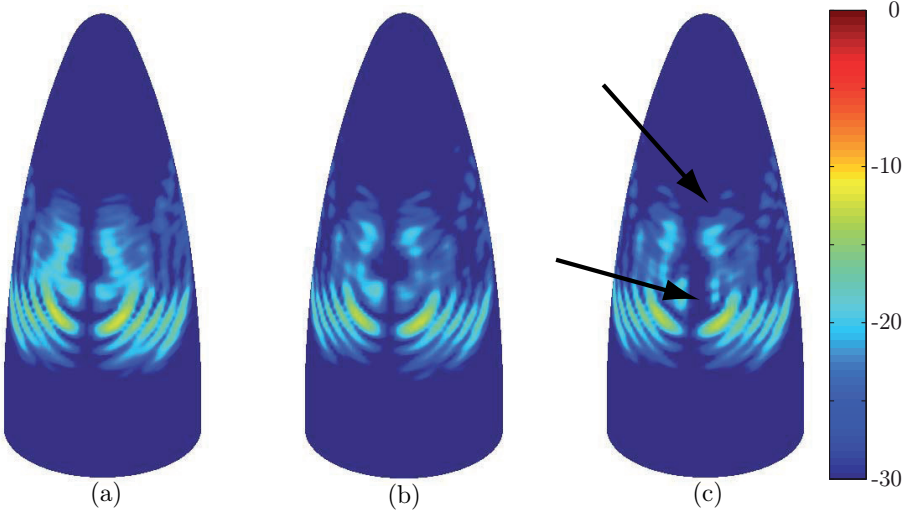
Figure 6: The recreated $|M^v|$-component on the front side of the radome. All values are normalized with the largest value of $|M^v|$ when the defect radome is present and shown in dB-scale. (a) No radome present. (b) Radome present. (c) Defect radome present. The arrows point out the locations of the copper plates.

This paper gives a relation between the accuracy and resolution in the problem, and calculates in which areas the solution is reliable.

The results reported in this thesis show great potential, and the method of calculating the IPD can hopefully be implemented for industrial use. Another exciting challenge is to combine the method with the transmission of the field through the radome [4].
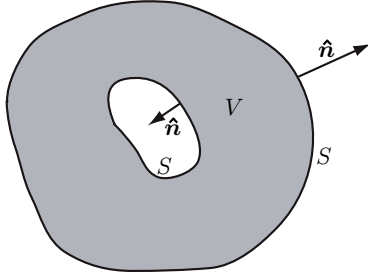
Figure 7: The domain V of integration.

Appendix A   Integral representations

There are several ways to derive the integral representations of the Maxwell equations [15, 27, 43, 65]. In this appendix, one way is demonstrated [31].

The surface integral representation expresses the electromagnetic field in a homogeneous and isotropic region in terms of its values on the bounding surface. The representation states that if the electromagnetic field on a surface of a volume is known, the electromagnetic field in the volume can be determined. The representation is derived starting with two arbitrary scalar fields, $\phi(\boldsymbol{r})$ and $\psi(\boldsymbol{r})$ and the divergence relation

$$\nabla \cdot [\phi(\boldsymbol{r})\nabla\psi(\boldsymbol{r}) - \psi(\boldsymbol{r})\nabla\phi(\boldsymbol{r})] = \phi(\boldsymbol{r})\nabla^2\psi(\boldsymbol{r}) - \psi(\boldsymbol{r})\nabla^2\phi(\boldsymbol{r}) \qquad \text{(A.1)}$$

The scalar fields are defined in a bounded domain V. The domain V is bounded by the surface S with outward pointing normal vector $\hat{\boldsymbol{n}}(\boldsymbol{r})$, see Figure 7. The surface does not have to be a surface that separates two different materials, but can be an arbitrary surface in space.

Integration of (A.1) over the volume V and the use of the divergence theorem give *the Green's second formula*, i.e.,

$$\iint_S [\phi(\boldsymbol{r})\nabla\psi(\boldsymbol{r}) - \psi(\boldsymbol{r})\nabla\phi(\boldsymbol{r})] \cdot \hat{\boldsymbol{n}}(\boldsymbol{r})\ \mathrm{d}S = \iiint_V \left[\phi(\boldsymbol{r})\nabla^2\psi(\boldsymbol{r}) - \psi(\boldsymbol{r})\nabla^2\phi(\boldsymbol{r})\right]\ \mathrm{d}v$$

$$\text{(A.2)}$$

Proceeding to the representation of vector fields, let the scalar field $\phi(\boldsymbol{r})$ in (A.2) be $[\boldsymbol{a} \cdot \boldsymbol{F}(\boldsymbol{r})]$, where $\boldsymbol{a}$ is an arbitrary constant vector and $\boldsymbol{F}(\boldsymbol{r})$ is a vector field. We have

$$\iint_S \left\{[\boldsymbol{a} \cdot \boldsymbol{F}(\boldsymbol{r})]\nabla\psi(\boldsymbol{r}) - \psi(\boldsymbol{r})\nabla[\boldsymbol{a} \cdot \boldsymbol{F}(\boldsymbol{r})]\right\} \cdot \hat{\boldsymbol{n}}(\boldsymbol{r})\ \mathrm{d}S$$

$$= \iiint_V \left\{[\boldsymbol{a} \cdot \boldsymbol{F}(\boldsymbol{r})]\nabla^2\psi(\boldsymbol{r}) - \psi(\boldsymbol{r})\nabla^2[\boldsymbol{a} \cdot \boldsymbol{F}(\boldsymbol{r})]\right\}\ \mathrm{d}v$$
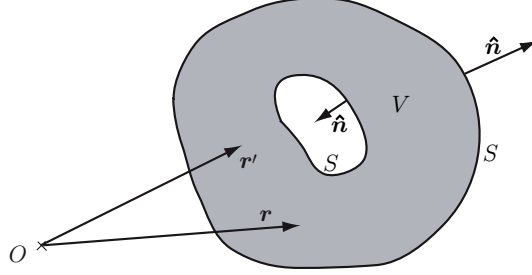
Figure 8: The domain V of integration. The variable of integration is denoted $\boldsymbol{r}'$ and the observation point $\boldsymbol{r}$.

Tedious algebra using differentiation rules of the Nabla-operator and the divergence theorem give

$$
\iint\limits_{S} \left(\psi(\boldsymbol{r})\big\{\hat{\boldsymbol{n}}(\boldsymbol{r}) \times [\nabla \times \boldsymbol{F}(\boldsymbol{r})]\big\} + \nabla\psi(\boldsymbol{r})\big[\hat{\boldsymbol{n}}(\boldsymbol{r}) \cdot \boldsymbol{F}(\boldsymbol{r})\big] \right.
$$

$$
\left. - \psi(\boldsymbol{r})\big[\nabla \cdot \boldsymbol{F}(\boldsymbol{r})\big]\hat{\boldsymbol{n}}(\boldsymbol{r}) - \nabla\psi(\boldsymbol{r}) \times \big[\hat{\boldsymbol{n}}(\boldsymbol{r}) \times \boldsymbol{F}(\boldsymbol{r})\big] \right) \, \mathrm{d}S
$$

$$
= \iiint\limits_{V} \left(\boldsymbol{F}(\boldsymbol{r})\,\nabla^2\psi(\boldsymbol{r}) + \psi(\boldsymbol{r})\big\{\nabla \times [\nabla \times \boldsymbol{F}(\boldsymbol{r})] - \nabla[\nabla \cdot \boldsymbol{F}(\boldsymbol{r})]\big\} \right) \, \mathrm{d}v \quad \text{(A.3)}
$$

which is *the Green's vector formula*. This equation is the foundation for finding integral representations of vector fields.

A.1   Introduction of the scalar free space Green's function

Let the scalar field ψ in (A.3) be the scalar Green's function,

$$
g(\boldsymbol{r},\boldsymbol{r}') = \frac{\mathrm{e}^{-\mathrm{j}k|\boldsymbol{r}-\boldsymbol{r}'|}}{4\pi|\boldsymbol{r}-\boldsymbol{r}'|}
$$

using the time conventions $\mathrm{e}^{\mathrm{j}\omega t}$. The variable of integration is denoted $\boldsymbol{r}'$ and the observation point $\boldsymbol{r}$, see Figure 8. Assume $\boldsymbol{r} \notin S$. The Green's function satisfies,

$$
\nabla^2 g(\boldsymbol{r},\boldsymbol{r}') + k^2 g(\boldsymbol{r},\boldsymbol{r}') = 0 \qquad\qquad \boldsymbol{r}' \neq \boldsymbol{r} \qquad\qquad \text{(A.4)}
$$
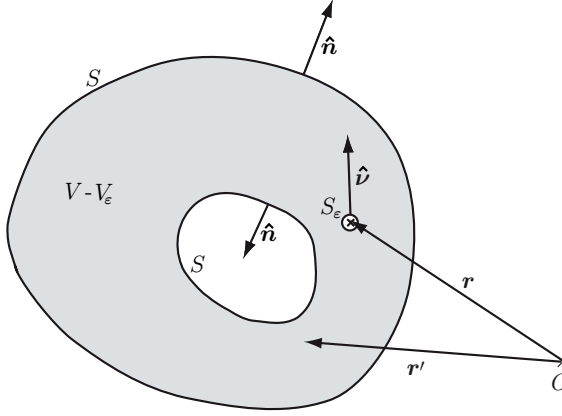
Figure 9: The geometry for the evaluation of the limit process. The volume V is punctuated by a ball of radius ϵ centered at the observation point $\boldsymbol{r}$. The bounding surface of this ball is S_ϵ and its volume is denoted V_ϵ. The variable of integration is denoted $\boldsymbol{r}'$.

where k is the wave number of the material. Replacing ψ in (A.3) with the scalar Green's function gives

$$\iint\limits_S \left(g(\boldsymbol{r},\boldsymbol{r}')\big\{\hat{\boldsymbol{n}}(\boldsymbol{r}') \times \big[\nabla' \times \boldsymbol{F}(\boldsymbol{r}')\big]\big\} + \nabla'g(\boldsymbol{r},\boldsymbol{r}')\big[\hat{\boldsymbol{n}}(\boldsymbol{r}') \cdot \boldsymbol{F}(\boldsymbol{r}')\big] \right.$$

$$\left. - g(\boldsymbol{r},\boldsymbol{r}')\big[\nabla' \cdot \boldsymbol{F}(\boldsymbol{r}')\big]\hat{\boldsymbol{n}}(\boldsymbol{r}') - \nabla'g(\boldsymbol{r},\boldsymbol{r}') \times \big[\hat{\boldsymbol{n}}(\boldsymbol{r}') \times \boldsymbol{F}(\boldsymbol{r}')\big] \right) \, \mathrm{d}S'$$

$$= \iiint\limits_V \left(g(\boldsymbol{r},\boldsymbol{r}')\big\{\nabla' \times \big[\nabla' \times \boldsymbol{F}(\boldsymbol{r}')\big] - \nabla'\big[\nabla' \cdot \boldsymbol{F}(\boldsymbol{r}')\big] - k^2\boldsymbol{F}(\boldsymbol{r}')\big\} \right) \, \mathrm{d}v' \quad (A.5)$$

where (A.4) is used. The Green's function is singular at the point $\boldsymbol{r}' = \boldsymbol{r}$. That is, the representation (A.5) is only valid when $\boldsymbol{r}' \neq \boldsymbol{r}$. The singularity can be treated in several ways. Here, the integrals are investigated in the limit of classical integrals. That is, a small ball V_ϵ, centered at the singularity $\boldsymbol{r}$, is excluded. The radius of this ball is ϵ and its spherical bounding surface is denoted S_ϵ, see Figure 9. Letting the radius of the sphere approach zero, in (A.5), gives

$$\iint\limits_S \cdots \, \mathrm{d}S' + \lim_{\boldsymbol{r}' \to \boldsymbol{r}} \iint\limits_{S_\epsilon} \cdots \, \mathrm{d}S' = \iiint\limits_V \cdots \, \mathrm{d}v' - \lim_{\boldsymbol{r}' \to \boldsymbol{r}} \iiint\limits_{V_\epsilon} \cdots \, \mathrm{d}v' \qquad (A.6)$$

The surface S_ϵ is parameterized in spherical coordinates, $i.e.$, $\epsilon \leqslant 0$, $0 \leqslant \varphi \leqslant 2\pi$, and $0 \leqslant \theta \leqslant \pi$, with $\hat{\boldsymbol{e}}_z$ as the symmetry axis. The used notation is, $cf.$, Figure 10,

$$\begin{aligned} \epsilon &= |\boldsymbol{r}' - \boldsymbol{r}| & \mathrm{d}S &= \epsilon^2 \sin\theta \, \mathrm{d}\varphi \, \mathrm{d}\theta \\ \hat{\boldsymbol{n}} &= -\hat{\boldsymbol{\nu}} & \mathrm{d}v &= \epsilon^2 \sin\theta \, \mathrm{d}\epsilon \, \mathrm{d}\varphi \, \mathrm{d}\theta \end{aligned} \qquad (A.7)$$
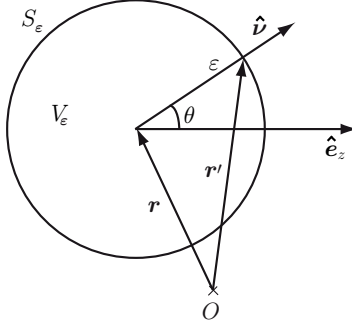
Figure 10: The geometry for the evaluation of integrals over the sphere S_ϵ.

$$\hat{\boldsymbol{\nu}} = \frac{\boldsymbol{r}' - \boldsymbol{r}}{\epsilon} = \cos\varphi\sin\theta\,\hat{\boldsymbol{e}}_x + \sin\varphi\sin\theta\,\hat{\boldsymbol{e}}_y + \cos\theta\,\hat{\boldsymbol{e}}_z$$

$$\nabla' g(\boldsymbol{r}, \boldsymbol{r}') = \frac{(\boldsymbol{r} - \boldsymbol{r}')\,\mathrm{e}^{-\mathrm{j}k|\boldsymbol{r}-\boldsymbol{r}'|}}{4\pi|\boldsymbol{r} - \boldsymbol{r}'|^3}\left[1 + \mathrm{j}k|\boldsymbol{r} - \boldsymbol{r}'|\right] = \hat{\boldsymbol{n}}\,\frac{\mathrm{e}^{-\mathrm{j}k\epsilon}}{4\pi\epsilon}\left[\frac{1}{\epsilon} + \mathrm{j}k\right] \tag{A.8}$$

where $\hat{\boldsymbol{e}}$ denotes the Cartesian orthonormal basis vectors in the x-, y-, and z-direction, respectively.

In the integrals over the small sphere S_ϵ, the normal unit vector $\hat{\boldsymbol{\nu}}$ varies rapidly over the integral domain while the fields $\boldsymbol{F}$, $[\nabla \cdot \boldsymbol{F}]$, $[\nabla \times \boldsymbol{F}]$, $\{\nabla \times [\nabla \times \boldsymbol{F}]\}$, and $\{\nabla[\nabla \cdot \boldsymbol{F}]\}$ are assumed to vary more slowly. Provided these fields are smooth (*e.g.*, Hölder continuous), the mean value theorem for integrals implies that in the limit of $\epsilon \to 0$ the fields can be evaluated at the singular point $\boldsymbol{r}$ [15]. Letting $\epsilon \to 0$, *i.e.*, $\boldsymbol{r}' \to \boldsymbol{r}$, results in the following limits for the different parts in (A.5).

$$\lim_{\epsilon\to0} \iint_{S_\epsilon} g(\boldsymbol{r}, \boldsymbol{r}')\left\{\hat{\boldsymbol{n}}(\boldsymbol{r}') \times \left[\nabla' \times \boldsymbol{F}(\boldsymbol{r}')\right]\right\}\,\mathrm{d}S'$$

$$= \lim_{\epsilon\to0} \iint_{S_\epsilon} \frac{\mathrm{e}^{-\mathrm{j}k\epsilon}}{4\pi\epsilon}\left\{\hat{\boldsymbol{n}}(\boldsymbol{r}') \times \left[\nabla' \times \boldsymbol{F}(\boldsymbol{r}')\right]\right\}\epsilon^2\sin\theta'\,\mathrm{d}\varphi'\,\mathrm{d}\theta' = \boldsymbol{0}$$

$$\lim_{\epsilon\to0} \iint_{S_\epsilon} \nabla' g(\boldsymbol{r}, \boldsymbol{r}')\left[\hat{\boldsymbol{n}}(\boldsymbol{r}') \cdot \boldsymbol{F}(\boldsymbol{r}')\right]\,\mathrm{d}S'$$

$$= \lim_{\epsilon\to0} \iint_{S_\epsilon} \hat{\boldsymbol{n}}(\boldsymbol{r}')\,\frac{\mathrm{e}^{-\mathrm{j}k\epsilon}}{4\pi\epsilon}\left[\frac{1}{\epsilon} + \mathrm{j}k\right]\left[\hat{\boldsymbol{n}}(\boldsymbol{r}') \cdot \boldsymbol{F}(\boldsymbol{r}')\right]\epsilon^2\sin\theta'\,\mathrm{d}\varphi'\,\mathrm{d}\theta'$$

$$= \frac{1}{4\pi} \iint_{S_\epsilon} \hat{\boldsymbol{n}}(\boldsymbol{r}')\left[\hat{\boldsymbol{n}}(\boldsymbol{r}') \cdot \boldsymbol{F}(\boldsymbol{r})\right]\sin\theta'\,\mathrm{d}\varphi'\,\mathrm{d}\theta'$$

$$
= \frac{1}{4\pi} \int\limits_{\theta'=0}^{\pi} \int\limits_{\varphi'=0}^{2\pi} \Big\{ \big[\cos\varphi' \sin\theta'\, \hat{\bm{e}}_x + \sin\varphi' \sin\theta'\, \hat{\bm{e}}_y + \cos\theta'\, \hat{\bm{e}}_z \big]
$$

$$
\cdot \big[F_x(\bm{r}) \cos\varphi' \sin\theta' + F_y(\bm{r}) \sin\varphi' \sin\theta' + F_z(\bm{r}) \cos\theta' \big] \sin\theta' \Big\}\, \mathrm{d}\varphi'\, \mathrm{d}\theta'
$$

$$
= \frac{1}{4\pi} \Big[\frac{4\pi}{3} F_x(\bm{r})\, \hat{\bm{e}}_x + \frac{4\pi}{3} F_y(\bm{r})\, \hat{\bm{e}}_y + \frac{4\pi}{3} F_z(\bm{r})\, \hat{\bm{e}}_z \Big] = \frac{1}{3} \bm{F}(\bm{r})
$$

$$
\lim_{\epsilon\to 0} \iint\limits_{S_\epsilon} g(\bm{r}, \bm{r}') \big[\nabla' \cdot \bm{F}(\bm{r}') \big] \hat{\bm{n}}(\bm{r}')\, \mathrm{d}S'
$$

$$
= \lim_{\epsilon\to 0} \iint\limits_{S_\epsilon} \frac{\mathrm{e}^{-\mathrm{j}k\epsilon}}{4\pi\epsilon} \big[\nabla' \cdot \bm{F}(\bm{r}') \big] \hat{\bm{n}}(\bm{r}')\, \epsilon^2 \sin\theta'\, \mathrm{d}\varphi'\, \mathrm{d}\theta' = \bm{0}
$$

$$
\lim_{\epsilon\to 0} \iint\limits_{S_\epsilon} \nabla' g(\bm{r}, \bm{r}') \times \big[\hat{\bm{n}}(\bm{r}') \times \bm{F}(\bm{r}') \big]\, \mathrm{d}S'
$$

$$
= \lim_{\epsilon\to 0} \iint\limits_{S_\epsilon} \hat{\bm{n}}(\bm{r}') \frac{\mathrm{e}^{-\mathrm{j}k\epsilon}}{4\pi\epsilon} \Big[\frac{1}{\epsilon} + \mathrm{j}k \Big] \times \big[\hat{\bm{n}}(\bm{r}') \times \bm{F}(\bm{r}') \big]\, \epsilon^2 \sin\theta'\, \mathrm{d}\varphi'\, \mathrm{d}\theta'
$$

$$
= \frac{1}{4\pi} \iint\limits_{S_\epsilon} \hat{\bm{n}}(\bm{r}') \times \big[\hat{\bm{n}}(\bm{r}') \times \bm{F}(\bm{r}) \big] \sin\theta'\, \mathrm{d}\varphi'\, \mathrm{d}\theta'
$$

$$
= \frac{1}{4\pi} \iint\limits_{S_\epsilon} \Big\{ \hat{\bm{n}}(\bm{r}') \big[\hat{\bm{n}}(\bm{r}') \cdot \bm{F}(\bm{r}) \big] - \bm{F}(\bm{r}) \big[\hat{\bm{n}}(\bm{r}') \cdot \hat{\bm{n}}(\bm{r}') \big] \Big\} \sin\theta'\, \mathrm{d}\varphi'\, \mathrm{d}\theta'
$$

$$
= \frac{1}{4\pi} \Big[\frac{4\pi}{3} \bm{F}(\bm{r}) - 4\pi \bm{F}(\bm{r}) \Big] = -\frac{2}{3} \bm{F}(\bm{r})
$$

$$
\lim_{\epsilon\to 0} \iiint\limits_{V_\epsilon} g(\bm{r}, \bm{r}') \Big\{ \nabla' \times \big[\nabla' \times \bm{F}(\bm{r}') \big] - \nabla' \big[\nabla' \cdot \bm{F}(\bm{r}') \big] - k^2 \bm{F}(\bm{r}') \Big\}\, \mathrm{d}v'
$$

$$
= \lim_{\epsilon\to 0} \iiint\limits_{V_\epsilon} \frac{\mathrm{e}^{-\mathrm{j}k\epsilon}}{4\pi\epsilon} \Big\{ \nabla' \times \big[\nabla' \times \bm{F}(\bm{r}') \big] - \nabla' \big[\nabla' \cdot \bm{F}(\bm{r}') \big]
$$

$$
- k^2 \bm{F}(\bm{r}') \Big\}\, \epsilon^2 \sin\theta'\, \mathrm{d}\epsilon\, \mathrm{d}\varphi'\, \mathrm{d}\theta' = \bm{0}
$$

The parts are inserted into (A.6) giving

$$
\iint\limits_{S} \dots\, \mathrm{d}S' + \bm{F}(\bm{r}) = \iiint\limits_{V} \dots\, \mathrm{d}v' - \bm{0} \qquad \bm{r} \in V
$$

Including the region without singularities, *i.e.*, $\boldsymbol{r} \notin V$, from (A.5), gives

$$\iiint\limits_{V} \left(g(\boldsymbol{r},\boldsymbol{r}')\Big\{\nabla' \times \big[\nabla' \times \boldsymbol{F}(\boldsymbol{r}')\big] - \nabla'\big[\nabla' \cdot \boldsymbol{F}(\boldsymbol{r}')\big] - k^2\boldsymbol{F}(\boldsymbol{r}')\Big\} \right) \mathrm{d}v'$$

$$- \iint\limits_{S} \left(g(\boldsymbol{r},\boldsymbol{r}')\Big\{\hat{\boldsymbol{n}}(\boldsymbol{r}') \times \big[\nabla' \times \boldsymbol{F}(\boldsymbol{r}')\big]\Big\} + \nabla'g(\boldsymbol{r},\boldsymbol{r}')\big[\hat{\boldsymbol{n}}(\boldsymbol{r}') \cdot \boldsymbol{F}(\boldsymbol{r}')\big] \right.$$

$$\left. - g(\boldsymbol{r},\boldsymbol{r}')\big[\nabla' \cdot \boldsymbol{F}(\boldsymbol{r}')\big]\hat{\boldsymbol{n}}(\boldsymbol{r}') - \nabla'g(\boldsymbol{r},\boldsymbol{r}') \times \big[\hat{\boldsymbol{n}}(\boldsymbol{r}') \times \boldsymbol{F}(\boldsymbol{r}')\big] \right) \mathrm{d}S' \tag{A.9}$$

$$= \begin{cases} \boldsymbol{F}(\boldsymbol{r}) & \boldsymbol{r} \in V \\ \boldsymbol{0} & \boldsymbol{r} \notin V \end{cases}$$

This is a general representation of a vector field $\boldsymbol{F}$. The field $\boldsymbol{F}$ is represented as a volume integral of its values in V and as a surface integral of its values over the bounding surface S of V. If these integrals are evaluated at a point $\boldsymbol{r}$ that lies outside the volume V, these integrals cancel each other — the extinction theorem. It is important to notice that this does not necessarily mean that the field $\boldsymbol{F}$ is identically zero outside the volume V — only the values of the integrals cancel.

A.2 Introduction of the Maxwell equations

So far, the vector field $\boldsymbol{F}$ has been an arbitrary vector field. This field can be chosen as the electric or magnetic field that satisfies the source free Maxwell equations with the time convention $\mathrm{e}^{\mathrm{j}\omega t}$, *i.e.*,

$$\begin{cases} \nabla \times \boldsymbol{E} = -\mathrm{j}\omega\boldsymbol{B} \\ \nabla \times \boldsymbol{H} = \mathrm{j}\omega\boldsymbol{D} \end{cases} \tag{A.10}$$

The constitutive relations in a homogeneous, isotropic region are given by

$$\begin{cases} \boldsymbol{D} = \epsilon_0\epsilon\boldsymbol{E} \\ \boldsymbol{B} = \mu_0\mu\boldsymbol{H} \end{cases} \tag{A.11}$$

Combination of (A.10) and (A.11) give

$$\begin{cases} \nabla \times \boldsymbol{E} = -\mathrm{j}\omega\mu_0\mu\boldsymbol{H} \\ \nabla \times \boldsymbol{H} = \mathrm{j}\omega\epsilon_0\epsilon\boldsymbol{E} \end{cases} \tag{A.12}$$

$$\begin{cases} \nabla \times (\nabla \times \boldsymbol{E}) = k^2\boldsymbol{E} \\ \nabla \times (\nabla \times \boldsymbol{H}) = k^2\boldsymbol{H} \end{cases} \tag{A.13}$$

$$\begin{cases} \nabla \cdot \boldsymbol{E} = 0 \\ \nabla \cdot \boldsymbol{H} = 0 \end{cases} \tag{A.14}$$

where ϵ_0 is the permittivity of vacuum, ϵ the relative permittivity, μ_0 the permeability of vacuum, μ the relative permeability, ω the angular frequency, and $k = \omega\sqrt{\epsilon_0\mu_0\epsilon\mu}$ the wave number.

Letting $\boldsymbol{F}$ be the electric field $\boldsymbol{E}$ in (A.9) gives together with (A.12)-(A.14) *a surface integral representation for the electric field*, *i.e.*,

$$\iint\limits_{S} \left\{ j\omega\mu_0\mu\ g(\boldsymbol{r},\boldsymbol{r}')\big[\hat{\boldsymbol{n}}(\boldsymbol{r}')\times\boldsymbol{H}(\boldsymbol{r}')\big] - \nabla'g(\boldsymbol{r},\boldsymbol{r}')\big[\hat{\boldsymbol{n}}(\boldsymbol{r}')\cdot\boldsymbol{E}(\boldsymbol{r}')\big] \right.$$

$$\left. + \nabla'g(\boldsymbol{r},\boldsymbol{r}')\times\big[\hat{\boldsymbol{n}}(\boldsymbol{r}')\times\boldsymbol{E}(\boldsymbol{r}')\big] \right\}\,\mathrm{d}S' = \begin{cases} \boldsymbol{E}(\boldsymbol{r}) & \boldsymbol{r}\ \text{inside}\ S \\ 0 & \boldsymbol{r}\ \text{outside}\ S \end{cases} \quad (\text{A}.15)$$

where the surface S is shown in Figure 8. Observe that the volume integral is zero and only the surface integral remains. The relative permittivity ϵ and the relative permeability μ may depend on the angular frequency ω, *i.e.*, the material can be dispersive, but constant as a function of space (homogeneous material). If $\boldsymbol{F}$ is interchanged by the magnetic field $\boldsymbol{H}$, a *surface integral representation for the magnetic field* is attained. The integral representation (A.15) contains both the normal and the tangential components of the electromagnetic field. In practice, it is more convenient to work only with the tangential fields. The normal component, *i.e.*, the second term in (A.15), can be written in terms of a tangential component by an application of the Maxwell equations (A.10)-(A.11), *i.e.*,

$$\hat{\boldsymbol{n}}(\boldsymbol{r})\cdot\boldsymbol{E}(\boldsymbol{r}) = -j\frac{1}{\omega\epsilon_0\epsilon}\ \hat{\boldsymbol{n}}(\boldsymbol{r})\cdot\big[\nabla\times\boldsymbol{H}(\boldsymbol{r})\big] = j\frac{1}{\omega\epsilon_0\epsilon}\nabla_S\cdot\big[\hat{\boldsymbol{n}}(\boldsymbol{r})\times\boldsymbol{H}(\boldsymbol{r})\big]$$

where the identity $\nabla_S\cdot(\hat{\boldsymbol{n}}\times\boldsymbol{a}) = -\hat{\boldsymbol{n}}\cdot(\nabla\times\boldsymbol{a})$ is used with $\boldsymbol{a}$ denoting an arbitrary vector and $\nabla_S\cdot$ the surface divergence [15]. That gives *a surface integral representation for the electric field* consisting of only tangential components on the surface S, *i.e.*,

$$\iint\limits_{S} \left(j\omega\mu_0\mu\ g(\boldsymbol{r},\boldsymbol{r}')\big[\hat{\boldsymbol{n}}(\boldsymbol{r}')\times\boldsymbol{H}(\boldsymbol{r}')\big] - j\frac{1}{\omega\epsilon_0\epsilon}\ \nabla'g(\boldsymbol{r},\boldsymbol{r}')\big\{\nabla'_S\cdot\big[\hat{\boldsymbol{n}}(\boldsymbol{r}')\times\boldsymbol{H}(\boldsymbol{r}')\big]\big\} \right.$$

$$\left. + \nabla'g(\boldsymbol{r},\boldsymbol{r}')\times\big[\hat{\boldsymbol{n}}(\boldsymbol{r}')\times\boldsymbol{E}(\boldsymbol{r}')\big] \right)\,\mathrm{d}S' = \begin{cases} \boldsymbol{E}(\boldsymbol{r}) & \boldsymbol{r}\ \text{inside}\ S \\ 0 & \boldsymbol{r}\ \text{outside}\ S \end{cases} \quad (\text{A}.16)$$

A.3   Values of the integral equations on the surface S

The integral representation in (A.16) is defined for all $\boldsymbol{r}\notin S$. To include the surface into the domain it must be studied what happens as $\boldsymbol{r}$ approaches S. At this stage it is not even clear that these limit values exist at all. The integrands in (A.16) become singular as $\boldsymbol{r}$ moves toward the surface. This singularity can be treated in several ways. Here, a classic approach is used, where the limit is investigated by adding a half sphere from the outside and the inside, respectively.

Figure 11: (a) The geometry for the evaluation of the limit process. In the limit the surface $(S' = S_{\text{punc}} \cup S_\epsilon) \to S$ and $V_{\text{punc}} \to V$. (b) The parameterization of the half sphere S_ϵ. Observe that $\hat{\boldsymbol{n}} = -\hat{\boldsymbol{\nu}}$.

Starting with the approach from the outside, the integral representation is, see (A.16)

$$\iint\limits_S \left(\mathrm{j}\omega\mu_0\mu \ g(\boldsymbol{r},\boldsymbol{r}')\big[\hat{\boldsymbol{n}}(\boldsymbol{r}') \times \boldsymbol{H}(\boldsymbol{r}')\big] - \mathrm{j}\frac{1}{\omega\epsilon_0\epsilon} \ \nabla' g(\boldsymbol{r},\boldsymbol{r}')\Big\{\nabla'_S \cdot \big[\hat{\boldsymbol{n}}(\boldsymbol{r}') \times \boldsymbol{H}(\boldsymbol{r}')\big]\Big\} \right.$$

$$\left. + \nabla' g(\boldsymbol{r},\boldsymbol{r}') \times \big[\hat{\boldsymbol{n}}(\boldsymbol{r}') \times \boldsymbol{E}(\boldsymbol{r}')\big] \right) \mathrm{d}S' = \boldsymbol{0} \qquad \boldsymbol{r} \notin V$$

It is applied to a volume V_{punc} which is slightly deformed compared to the original volume V, *i.e.*, a small half ball of radius ϵ is excluded. The bounding surface of the volume V_{punc} is denoted S' and consists of two parts: the punctuated surface S_{punc}, and a half sphere S_ϵ of radius ϵ, *i.e.*, $S' = S_{\text{punc}} \cup S_\epsilon$, see Figure 11a. In the limit $\epsilon \to 0$ the surface $S' \to S$ and $V_{\text{punc}} \to V$, *i.e.*,

$$\lim_{\boldsymbol{r}' \to \boldsymbol{r}} \iint\limits_{S'} \ ... \ \mathrm{d}S' = \iint\limits_S \!\!\!\!\!\!\!\!\!\!\!\! - \ \ ... \ \mathrm{d}S' + \lim_{\boldsymbol{r}' \to \boldsymbol{r}} \iint\limits_{S_\epsilon} \ ... \ \mathrm{d}S' \qquad (A.17)$$

where the integral $\iint - ... \ \mathrm{d}S$ denotes Cauchy's principal value [50].

To investigate the limit of the integral over the surface S_ϵ, this surface is parameterized by the spherical angles $0 \leqslant \varphi \leqslant 2\pi$ and $0 \leqslant \theta \leqslant \pi/2$ with the direction $\boldsymbol{e}_z$ as the symmetry axis, see Figure 11b and (A.7)-(A.8). The normal unit vector $\hat{\boldsymbol{\nu}}$ varies rapidly over the small half sphere S_ϵ, while the electromagnetic fields $\boldsymbol{E}$ and $\boldsymbol{H}$ are assumed to vary more slowly. Provided these fields are smooth (*e.g.*, Hölder continuous), the mean value theorem for integrals implies that in the limit of $\epsilon \to 0$ the fields can be evaluated at the point $\boldsymbol{r}$ [15]. Letting $\epsilon \to 0$, in the integrals over

S_ϵ, give the following limits[1]

$$\lim_{\epsilon \to 0} \iint\limits_{S_\epsilon} g(\boldsymbol{r}, \boldsymbol{r}') \big[\hat{\boldsymbol{n}}(\boldsymbol{r}') \times \boldsymbol{H}(\boldsymbol{r}')\big] \, \mathrm{d}S'$$

$$= \lim_{\epsilon \to 0} \iint\limits_{S_\epsilon} \frac{\mathrm{e}^{-\mathrm{j}k\epsilon}}{4\pi\epsilon} \big[-\hat{\boldsymbol{\nu}}(\boldsymbol{r}') \times \boldsymbol{H}(\boldsymbol{r}')\big] \, \epsilon^2 \sin\theta' \, \mathrm{d}\varphi' \, \mathrm{d}\theta' = \boldsymbol{0}$$

$$\lim_{\epsilon \to 0} \iint\limits_{S_\epsilon} -\mathrm{j}\frac{1}{\omega\epsilon_0\epsilon_\mathrm{r}} \, \nabla' g(\boldsymbol{r}, \boldsymbol{r}') \Big\{ \nabla'_S \cdot \big[\hat{\boldsymbol{n}}(\boldsymbol{r}') \times \boldsymbol{H}(\boldsymbol{r}')\big] \Big\} \, \mathrm{d}S'$$

$$= \lim_{\epsilon \to 0} \iint\limits_{S_\epsilon} -\nabla' g(\boldsymbol{r}, \boldsymbol{r}') \big[\hat{\boldsymbol{n}}(\boldsymbol{r}') \cdot \boldsymbol{E}(\boldsymbol{r}')\big] \, \mathrm{d}S'$$

$$= \lim_{\epsilon \to 0} \iint\limits_{S_\epsilon} \hat{\boldsymbol{\nu}}(\boldsymbol{r}') \frac{\mathrm{e}^{-\mathrm{j}k\epsilon}}{4\pi\epsilon} \left[\frac{1}{\epsilon} + \mathrm{j}k\right] \big[-\hat{\boldsymbol{\nu}}(\boldsymbol{r}') \cdot \boldsymbol{E}(\boldsymbol{r}')\big] \, \epsilon^2 \sin\theta' \, \mathrm{d}\varphi' \, \mathrm{d}\theta'$$

$$= -\frac{1}{4\pi} \iint\limits_{S_\epsilon} \hat{\boldsymbol{\nu}}(\boldsymbol{r}') \big[\hat{\boldsymbol{\nu}}(\boldsymbol{r}') \cdot \boldsymbol{E}(\boldsymbol{r})\big] \sin\theta' \, \mathrm{d}\varphi' \, \mathrm{d}\theta'$$

$$= -\frac{1}{4\pi} \int\limits_{\theta'=0}^{\pi/2} \int\limits_{\varphi'=0}^{2\pi} \Big\{ \big[\cos\varphi' \sin\theta' \, \hat{\boldsymbol{e}}_x + \sin\varphi' \sin\theta' \, \hat{\boldsymbol{e}}_y + \cos\theta' \, \hat{\boldsymbol{e}}_z\big]$$

$$\cdot \big[E_x(\boldsymbol{r}) \cos\varphi' \sin\theta' + E_y(\boldsymbol{r}) \sin\varphi' \sin\theta' + E_z(\boldsymbol{r}) \cos\theta'\big] \, \sin\theta' \Big\} \, \mathrm{d}\varphi' \, \mathrm{d}\theta'$$

$$= -\frac{1}{4\pi} \left[\frac{2\pi}{3} E_x(\boldsymbol{r}) \, \hat{\boldsymbol{e}}_x + \frac{2\pi}{3} E_y(\boldsymbol{r}) \, \hat{\boldsymbol{e}}_y + \frac{2\pi}{3} E_z(\boldsymbol{r}) \, \hat{\boldsymbol{e}}_z\right] = -\frac{1}{6} \boldsymbol{E}(\boldsymbol{r})$$

$$\lim_{\epsilon \to 0} \iint\limits_{S_\epsilon} \nabla' g(\boldsymbol{r}, \boldsymbol{r}') \times \big[\hat{\boldsymbol{n}}(\boldsymbol{r}') \times \boldsymbol{E}(\boldsymbol{r}')\big] \, \mathrm{d}S'$$

$$= \lim_{\epsilon \to 0} \iint\limits_{S_\epsilon} -\hat{\boldsymbol{\nu}}(\boldsymbol{r}') \frac{\mathrm{e}^{-\mathrm{j}k\epsilon}}{4\pi\epsilon} \left[\frac{1}{\epsilon} + \mathrm{j}k\right] \times \big[-\hat{\boldsymbol{\nu}}(\boldsymbol{r}') \times \boldsymbol{E}(\boldsymbol{r}')\big] \, \epsilon^2 \sin\theta' \, \mathrm{d}\varphi' \, \mathrm{d}\theta'$$

$$= \frac{1}{4\pi} \iint\limits_{S_\epsilon} \hat{\boldsymbol{\nu}}(\boldsymbol{r}') \times \big[\hat{\boldsymbol{\nu}}(\boldsymbol{r}') \times \boldsymbol{E}(\boldsymbol{r})\big] \sin\theta' \, \mathrm{d}\varphi' \, \mathrm{d}\theta'$$

$$= \frac{1}{4\pi} \int\limits_{\theta'=0}^{\pi/2} \int\limits_{\varphi'=0}^{2\pi} \Big\{ \hat{\boldsymbol{\nu}}(\boldsymbol{r}') \big[\hat{\boldsymbol{\nu}}(\boldsymbol{r}') \cdot \boldsymbol{E}(\boldsymbol{r})\big] - \boldsymbol{E}(\boldsymbol{r}) \big[\hat{\boldsymbol{\nu}}(\boldsymbol{r}') \cdot \hat{\boldsymbol{\nu}}(\boldsymbol{r}')\big] \Big\} \sin\theta' \, \mathrm{d}\varphi' \, \mathrm{d}\theta'$$

$$= \frac{1}{4\pi} \left[\frac{2\pi}{3} \boldsymbol{E}(\boldsymbol{r}) - 2\pi \boldsymbol{E}(\boldsymbol{r})\right] = -\frac{1}{3} \boldsymbol{E}(\boldsymbol{r})$$

The limit values above are plugged into (A.17), *i.e.*,

---

[1]In the second integral, the relative permittivity is temporarily denoted by ϵ_r to avoid mix up with the radius ϵ.
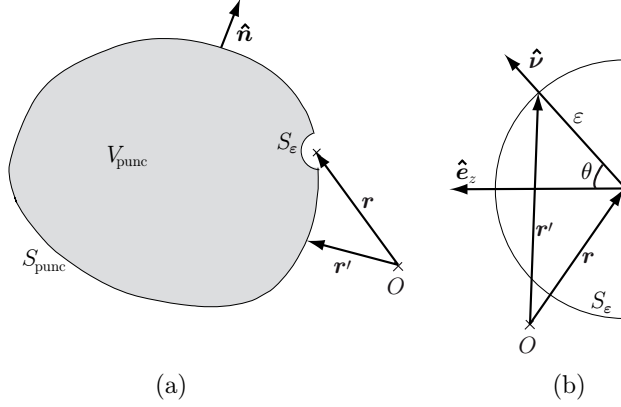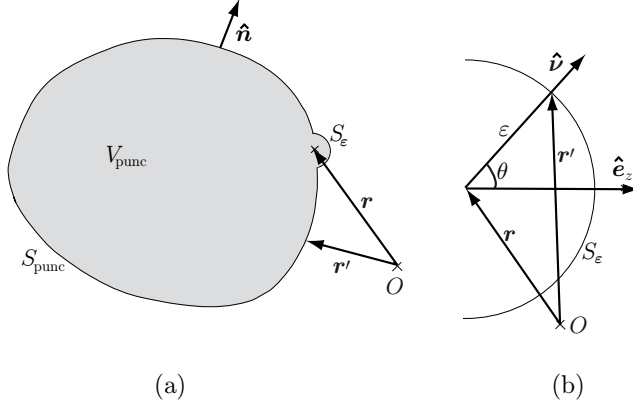
Figure 12: (a) The geometry for the evaluation of the limit process. In the limit the surface $(S' = S_{\text{punc}} \cup S_\epsilon) \to S$ and $V_{\text{punc}} \to V$. (b) The parameterization of the half sphere S_ϵ. Observe that now $\hat{\boldsymbol{n}} = \hat{\boldsymbol{\nu}}$.

$$\oiint_S \left(j\omega\mu_0\mu \; g(\boldsymbol{r},\boldsymbol{r}')\big[\hat{\boldsymbol{n}}(\boldsymbol{r}') \times \boldsymbol{H}(\boldsymbol{r}')\big] - j\frac{1}{\omega\epsilon_0\epsilon} \; \nabla'g(\boldsymbol{r},\boldsymbol{r}')\Big\{\nabla'_S \cdot \big[\hat{\boldsymbol{n}}(\boldsymbol{r}') \times \boldsymbol{H}(\boldsymbol{r}')\big]\Big\} \right.$$

$$\left. + \nabla'g(\boldsymbol{r},\boldsymbol{r}') \times \big[\hat{\boldsymbol{n}}(\boldsymbol{r}') \times \boldsymbol{E}(\boldsymbol{r}')\big] \right) \mathrm{d}S' = \frac{1}{2}\boldsymbol{E}(\boldsymbol{r}) \qquad \boldsymbol{r} \in S \quad \text{(A.18)}$$

which is the limit value of the surface integral representation for the electric field when approaching from the outside.[2]

If the limit is taken from the inside instead, the integral representation, (A.16), *i.e.*,

$$\iint_S \left(j\omega\mu_0\mu \; g(\boldsymbol{r},\boldsymbol{r}')\big[\hat{\boldsymbol{n}}(\boldsymbol{r}') \times \boldsymbol{H}(\boldsymbol{r}')\big] - j\frac{1}{\omega\epsilon_0\epsilon_\mathrm{r}} \; \nabla'g(\boldsymbol{r},\boldsymbol{r}')\Big\{\nabla'_S \cdot \big[\hat{\boldsymbol{n}}(\boldsymbol{r}') \times \boldsymbol{H}(\boldsymbol{r}')\big]\Big\} \right.$$

$$\left. + \nabla'g(\boldsymbol{r},\boldsymbol{r}') \times \big[\hat{\boldsymbol{n}}(\boldsymbol{r}') \times \boldsymbol{E}(\boldsymbol{r}')\big] \right) \mathrm{d}S' = \boldsymbol{E}(\boldsymbol{r}) \qquad \boldsymbol{r} \in V \quad \text{(A.19)}$$

is applied to a volume V_{punc} shown in Figure 12a. The derivation is similar to the analysis above. The difference is that now $\hat{\boldsymbol{n}} = \hat{\boldsymbol{\nu}}$. This changes the sign in the limit processes, which inserted in (A.19) give the same final integral equation, *i.e.*, (A.18).

The representation (A.18) consists of three components, two describing the tangential field and one describing the normal component of the field. Since the normal component can be determined by the knowledge of the tangential parts the normal

---

[2]The first surface integral does not have to be written as Cauchy's principle value since $\oiint_S \ldots \mathrm{d}S = \iint_S \ldots \mathrm{d}S$.
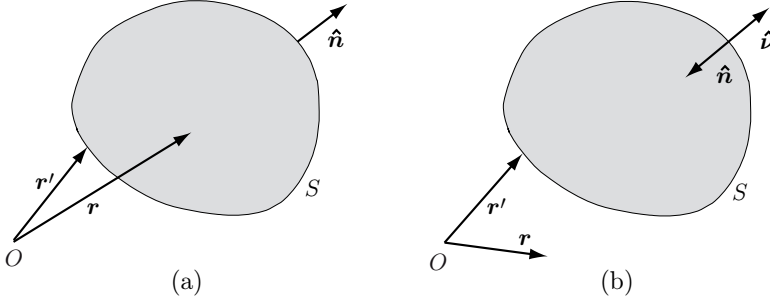
Figure 13: (a) The interior problem. (b) The exterior problem.

component can be eliminated [43], *i.e.*,

$$\hat{\boldsymbol{n}}(\boldsymbol{r}) \times \iint\limits_{S} \left(j\omega\mu_0\mu \; g(\boldsymbol{r},\boldsymbol{r}')\big[\hat{\boldsymbol{n}}(\boldsymbol{r}') \times \boldsymbol{H}(\boldsymbol{r}')\big] - j\frac{1}{\omega\epsilon_0\epsilon} \; \nabla'g(\boldsymbol{r},\boldsymbol{r}')\Big\{\nabla'_S \cdot \big[\hat{\boldsymbol{n}}(\boldsymbol{r}') \times \boldsymbol{H}(\boldsymbol{r}')\big]\Big\} \right.$$

$$\left. + \nabla'g(\boldsymbol{r},\boldsymbol{r}') \times \big[\hat{\boldsymbol{n}}(\boldsymbol{r}') \times \boldsymbol{E}(\boldsymbol{r}')\big] \right) \mathrm{d}S' = \frac{1}{2}\,\hat{\boldsymbol{n}}(\boldsymbol{r}) \times \boldsymbol{E}(\boldsymbol{r}) \qquad \boldsymbol{r} \in S \quad \text{(A.20)}$$

A.4   The equivalent surface currents

The electric and magnetic equivalent surface currents, $\boldsymbol{J}$ and $\boldsymbol{M}$, are defined as [8]

$$\begin{cases} \boldsymbol{J}(\boldsymbol{r}) = \hat{\boldsymbol{n}}(\boldsymbol{r}) \times \boldsymbol{H}(\boldsymbol{r}) \\ \boldsymbol{M}(\boldsymbol{r}) = -\,\hat{\boldsymbol{n}}(\boldsymbol{r}) \times \boldsymbol{E}(\boldsymbol{r}) \end{cases}$$

Introducing the equivalent currents in (A.16) and (A.20) yield *a surface integral representation and a surface integral equation for the electric field*

$$\begin{cases} \displaystyle\iint\limits_{S} \Big\{ j\omega\mu_0\mu \; g(\boldsymbol{r},\boldsymbol{r}')\boldsymbol{J}(\boldsymbol{r}') - j\frac{1}{\omega\epsilon_0\epsilon} \; \nabla'g(\boldsymbol{r},\boldsymbol{r}')\big[\nabla'_S \cdot \boldsymbol{J}(\boldsymbol{r}')\big] \\ \qquad\qquad - \nabla'g(\boldsymbol{r},\boldsymbol{r}') \times \boldsymbol{M}(\boldsymbol{r}')\Big\} \,\mathrm{d}S' = \boldsymbol{E}(\boldsymbol{r}) \qquad \boldsymbol{r} \text{ inside } S \\[2ex] \hat{\boldsymbol{n}}(\boldsymbol{r}) \times \displaystyle\iint\limits_{S} \Big\{ j\omega\mu_0\mu \; g(\boldsymbol{r},\boldsymbol{r}')\boldsymbol{J}(\boldsymbol{r}') - j\frac{1}{\omega\epsilon_0\epsilon} \; \nabla'g(\boldsymbol{r},\boldsymbol{r}')\big[\nabla'_S \cdot \boldsymbol{J}(\boldsymbol{r}')\big] \\ \qquad\qquad - \nabla'g(\boldsymbol{r},\boldsymbol{r}') \times \boldsymbol{M}(\boldsymbol{r}')\Big\} \,\mathrm{d}S' = -\frac{1}{2}\,\boldsymbol{M}(\boldsymbol{r}) \qquad \boldsymbol{r} \in S \end{cases}$$

The regions are depicted in Figure 13a.

In this thesis, the integral representation and equation are applied to the exterior problem, *i.e.*, see Figure 13b. This volume is not bounded. However, employing the

Silver-Müller radiation conditions, the solution of the Maxwell equations satisfies the following integral representation [29, 43, 60, 65]

$$
\begin{cases}
\displaystyle\iint\limits_{S} \left\{ \mathrm{j}\omega\mu_0\mu \; g(\boldsymbol{r},\boldsymbol{r}')\boldsymbol{J}(\boldsymbol{r}') - \mathrm{j}\frac{1}{\omega\epsilon_0\epsilon} \; \nabla'g(\boldsymbol{r},\boldsymbol{r}')\big[\nabla'_S \cdot \boldsymbol{J}(\boldsymbol{r}')\big] \right. \\
\qquad\qquad \left. - \nabla'g(\boldsymbol{r},\boldsymbol{r}') \times \boldsymbol{M}(\boldsymbol{r}') \right\} \mathrm{d}S' = -\boldsymbol{E}(\boldsymbol{r}) \qquad \boldsymbol{r} \text{ outside } S \\[2mm]
\displaystyle\hat{\boldsymbol{\nu}}(\boldsymbol{r}) \times \oiint\limits_{S} \left\{ \mathrm{j}\omega\mu_0\mu \; g(\boldsymbol{r},\boldsymbol{r}')\boldsymbol{J}(\boldsymbol{r}') - \mathrm{j}\frac{1}{\omega\epsilon_0\epsilon} \; \nabla'g(\boldsymbol{r},\boldsymbol{r}')\big[\nabla'_S \cdot \boldsymbol{J}(\boldsymbol{r}')\big] \right. \\
\qquad\qquad \left. - \nabla'g(\boldsymbol{r},\boldsymbol{r}') \times \boldsymbol{M}(\boldsymbol{r}') \right\} \mathrm{d}S' = \frac{1}{2}\boldsymbol{M}(\boldsymbol{r}) \qquad \boldsymbol{r} \in S
\end{cases}
$$

where the change of signs is due to the choice of normal, $i.e.$, $\hat{\boldsymbol{\nu}} = -\hat{\boldsymbol{n}}$.

References

[1] Y. Alvarez and F. Las-Heras. Integral equation algorithms for equivalent currents distribution retrieval over arbitrary three-dimensional surfaces. In *Proc. 2006 IEEE Antennas and Propagation Society International Symp.*, pages 1061–1064, Albuquerque, New Mexico, 2006.

[2] Y. Alvarez, F. Las-Heras, and M. R. Pino. Full-wave method for RF sources location. In *Proc. Second European Conference on Antennas and Propagation*, pages 1–5, Edinburgh, UK, 2007. The Institution of Engineering and Technology.

[3] Y. Alvarez, F. Las-Heras, and M. R. Pino. Reconstruction of equivalent currents distribution over arbitrary three-dimensional surfaces based on integral equation algorithms. *IEEE Trans. Antennas Propagat.*, **55**(12), 3460–3468, 2007.

[4] M. Andersson. Software for analysis of radome performance. In *Proc. International Conference on Electromagnetics in Advanced Applications (ICEAA'05)*, pages 537–539, Torino, Italy, 2005.

[5] B. Audone, A. Delogu, and P. Moriondo. Radome design and measurements. *IEEE Trans. Antennas Propagat.*, **37**(2), 292–295, 1988.

[6] R. G. Ayestarán and F. Las-Heras. Near field to far field transformation using neural networks and source reconstruction. *J. Electromagn. Waves Appl.*, **20**(15), 2201–2213, 2006.

[7] R. G. Ayestarán and F. Las-Heras. Neural network-based array synthesis in presence of obstacles. *International Journal of Numerical Modelling-Electronic Networks Devices and Fields*, **19**, 1–13, 2006.

[8] C. A. Balanis. *Advanced Engineering Electromagnetics*. John Wiley & Sons, New York, 1989.

[9] A. Bondeson, T. Rylander, and P. Ingelström. *Computational Electromagnetics*. Springer-Verlag, Berlin, 2005.

[10] H. G. Booker and P. C. Clemmow. The concept of an angular spectrum of plane waves and its relation to that of polar diagram and aperture distribution. *Proc. Inst. Elec. Eng.*, **97**(1), 11–16, 1950.

[11] A. Boström, G. Kristensson, and S. Ström. Transformation properties of plane, spherical and cylindrical scalar and vector wave functions. In V. V. Varadan, A. Lakhtakia, and V. K. Varadan, editors, *Field Representations and Introduction to Scattering*, Acoustic, Electromagnetic and Elastic Wave Scattering, chapter 4, pages 165–210. Elsevier Science Publishers, Amsterdam, 1991.

[12] O. M. Bucci, M. D. Migliore, G. Panariello, and P. Sgambato. Accurate diagnosis of conformal arrays from near-field data using the matrix method. *IEEE Trans. Antennas Propagat.*, **53**(3), 1114–1120, 2005.

[13] C. Cappellin, O. Breinbjerg, and A. Frandsen. Properties of the transformation from the spherical wave expansion to the plane wave expansion. *Radio Sci.*, **43**(1), 2008.

[14] C. Cappellin, A. Frandsen, and O. Breinbjerg. Application of the SWE-to-PWE antenna diagnostics technique to an offset reflector antenna. *IEEE Antennas and Propagation Magazine*, **50**(5), 204–213, 2008.

[15] D. Colton and R. Kress. *Integral Equation Methods in Scattering Theory*. John Wiley & Sons, New York, 1983.

[16] L. E. Corey and E. B. Joy. On computation of electromagnetic fields on planar surfaces from fields specified on nearby surfaces. *IEEE Trans. Antennas Propagat.*, **29**(2), 402–404, 1981.

[17] A. Delogu and M. Mwanya. Design and testing of a radome for a beam steering radar antenna. In *Proc. International Conference on Electromagnetics in Advanced Applications (ICEAA'05)*, pages 505–508, Torino, Italy, 2005.

[18] A. J. Devaney and E. Wolf. Radiating and nonradiating classical current distributions and the fields they generate. *Phys. Rev. D*, **8**(4), 1044–1047, 1973.

[19] A. J. Devaney and E. Wolf. Multipole expansions and plane wave representations of the electromagnetic field. *J. Math. Phys.*, **15**(2), 234–244, 1974.

[20] T. F. Eibert and C. H. Schmidt. Multilevel fast multipole accelerated inverse equivalent current method employing Rao-Wilton-Glisson discretization of electric and magnetic surface currents. *IEEE Trans. Antennas Propagat.*, **57**(4), 1178–1185, 2009.

[21] J. Fridén, H. Isaksson, B. Hansson, and B. Thors. Robust phase-retrieval for quick whole-body SAR assessment using dual plane amplitude-only data. *Electronics Letters*, **45**(23), 1155–1157, 2009.

[22] M. G. Guler and E. B. Joy. High resolution spherical microwave holography. *IEEE Trans. Antennas Propagat.*, **43**(5), 464–472, 1995.

[23] J. Hanfling, G. Borgiotti, and L. Kaplan. The backward transform of the near field for reconstruction of aperture fields. *IEEE Antennas and Propagation Society International Symposium*, **17**, 764–767, 1979.

[24] J. E. Hansen, editor. *Spherical Near-Field Antenna Measurements*. Number 26 in IEE electromagnetic waves series. Peter Peregrinus Ltd., Stevenage, UK, 1988. ISBN: 0-86341-110-X.

[25] T. B. Hansen and A. D. Yaghjian, editors. *Plane-wave theory of time-domain fields: near-field scanning applications*. IEEE electromagnetic wave theory. IEEE Press, New York, 1999. ISBN: 0-7803-3428-0.

[26] M. M. Hernando, A. Fernandez, M. Arias, M. Rodriguez, Y. Alvarez, and F. Las-Heras. EMI radiated noise measurement system using the source reconstruction technique. *IEEE Trans. Industrial Electronics*, **55**(9), 3258–3265, 2008.

[27] D. S. Jones. *Acoustic and Electromagnetic Waves*. Oxford University Press, New York, 1986.

[28] S. M. Kay. *Fundamentals of Statistical Signal Processing, Estimation Theory*. Prentice-Hall, Inc., NJ, 1993.

[29] R. E. Kleinman and G. F. Roach. Boundary integral equations for the three-dimensional Helmholtz equation. *SIAM Review*, **16**(2), 214–236, 1974.

[30] B. M. Kolundžija and A. R. Djordjević. *Electromagnetic modeling of composite metallic and dielectric structures*. Artech House, Boston, London, 2002.

[31] G. Kristensson. *Spridningsteori med antenntillämpningar*. Studentlitteratur, Lund, 1999. (In Swedish).

[32] F. Las-Heras, B. Galocha, and Y. Alvarez. On the sources reconstruction method application for array and aperture antennas diagnostics. *Microwave Opt. Techn. Lett.*, **51**(7), 1664–1668, 2009.

[33] F. Las-Heras, B. Galocha, and J. L. Besada. Far-field performance of linear antennas determined from near-field data. *IEEE Trans. Antennas Propagat.*, **50**(3), 408–410, 2002.

[34] F. Las-Heras, M. R. Pino, S. Loredo, Y. Alvarez, and T. K. Sarkar. Evaluating near-field radiation patterns of commercial antennas. *IEEE Trans. Antennas Propagat.*, **54**(8), 2198–2207, 2006.

[35] F. Las-Heras and T. K. Sarkar. Radial field retrieval in spherical scanning for current reconstruction and NF–FF transformation. *IEEE Trans. Antennas Propagat.*, **50**(6), 866–874, 2002.

[36] J.-J. Laurin, J.-F. Zürcher, and F. E. Gardiol. Near-field diagnostics of small printed antennas using the equivalent magnetic current approach. *IEEE Trans. Antennas Propagat.*, **49**(5), 814–828, 2001.

[37] J. Lee, E. M. Ferren, D. P. Woollen, and K. M. Lee. Near-field probe used as a diagnostic tool to locate defective elements in an array antenna. *IEEE Trans. Antennas Propagat.*, **36**(6), 884–889, 1988.

[38] I. V. Lindell. *Methods for Electromagnetic Field Analysis.* IEEE Press and Oxford University Press, Oxford, 1995.

[39] C.-C. Lu. A fast algorithm based on volume integral equation for analysis of arbitrary shaped dielectric radomes. *IEEE Trans. Antennas Propagat.*, **51**(3), 606–612, 2003.

[40] E. A. Marengo and A. J. Devaney. The inverse source problem of electromagnetics: Linear inversion formulation and minimum energy solution. *IEEE Trans. Antennas Propagat.*, **47**(2), 410–412, February 1999.

[41] E. A. Marengo, A. J. Devaney, and F. K. Gruber. Inverse source problem with reactive power constraint. *IEEE Trans. Antennas Propagat.*, **52**(6), 1586–1595, June 2004.

[42] E. A. Marengo and R. W. Ziolkowski. Nonradiating and minimum energy sources and their fields: Generalized source inversion theory and applications. *IEEE Trans. Antennas Propagat.*, **48**(10), 1553–1562, October 2000.

[43] C. Müller. *Foundations of the Mathematical Theory of Electromagnetic Waves.* Springer-Verlag, Berlin, 1969.

[44] M. S. Narasimhan and B. P. Kumar. A technique of synthesizing the excitation currents of planar arrays or apertures. *IEEE Trans. Antennas Propagat.*, **38**(9), 1326–1332, 1990.

[45] S. Nordebo, M. Gustafsson, and K. Persson. Sensitivity analysis for antenna near-field imaging. *IEEE Trans. Signal Process.*, **55**(1), 94–101, January 2007.

[46] S. Nordebo and M. Gustafsson. Statistical signal analysis for the inverse source problem of electromagnetics. *IEEE Trans. Signal Process.*, **54**(6), 2357–2361, June 2006.

[47] A. F. Peterson, S. L. Ray, and R. Mittra. *Computational Methods for Electromagnetics.* IEEE Press, New York, 1998.

[48] P. Petre and T. K. Sarkar. Planar near-field to far-field transformation using an equivalent magnetic current approach. *IEEE Trans. Antennas Propagat.*, **40**(11), 1348–1356, 1992.

[49] P. Petre and T. K. Sarkar. Planar near-field to far-field transformation using an array of dipole probes. *IEEE Trans. Antennas Propagat.*, **42**(4), 534–537, 1994.

[50] A. J. Poggio and E. K. Miller. Integral equation solutions of three-dimensional scattering problems. In R. Mittra, editor, *Computer Techniques for Electromagnetics*. Pergamon, New York, 1973.

[51] S. Poulsen. *Stealth radomes*. PhD thesis, Lund University, Department of Electroscience, Lund University, P.O. Box 118, S-221 00 Lund, Sweden, 2006.

[52] D. M. Pozar. *Microwave Engineering*. John Wiley & Sons, New York, 1998.

[53] Y. Rahmat-Samii. Surface diagnosis of large reflector antennas using microwave holographic metrology: an iterative approach. *Radio Sci.*, **19**(5), 1205–1217, 1984.

[54] Y. Rahmat-Samii and J. Lemanczyk. Application of spherical near-field measurements to microwave holographic diagnosis of antennas. *IEEE Trans. Antennas Propagat.*, **36**(6), 869–878, 1988.

[55] D. J. Rochblatt and B. L. Seidel. Microwave antenna holography. *IEEE Trans. Microwave Theory Tech.*, **40**(6), 1294–1300, 1992.

[56] T. K. Sarkar and A. Taaghol. Near-field to near/far-field transformation for arbitrary near-field geometry utilizing an equivalent electric current and MoM. *IEEE Trans. Antennas Propagat.*, **47**(3), 566–573, March 1999.

[57] J. A. Shifflett. CADDRAD: A physical opics radar/radome analysis code for arbitrary 3D geometries. *IEEE Antennas and Propagation Magazine*, **6**(39), 73–79, 1997.

[58] R. A. Shore and A. D. Yaghjian. Dual surface electric field integral equation. Air Force Research Laboratory Report, 2001. No. AFRL-SN-HS-TR-2001-013.

[59] R. A. Shore and A. D. Yaghjian. Dual-surface integral equations in electromagnetic scattering. *IEEE Trans. Antennas Propagat.*, **53**(5), 1706–1709, 2005.

[60] S. Silver. *Microwave Antenna Theory and Design*, volume 12 of *Radiation Laboratory Series*. McGraw-Hill, New York, 1949.

[61] J. C.-E. Sten. Reconstruction of electromagnetic minimum energy sources in a prolate spheroid. *Radio Sci.*, **39**(2), 2004.

[62] J. C.-E. Sten and E. A. Marengo. Inverse source problem in an oblate spheroidal geometry. *IEEE Trans. Antennas Propagat.*, **54**(11), 3418–3428, 2006.

[63] J. C.-E. Sten and E. A. Marengo. Inverse source problem in the spheroidal geometry: Vector formulation. *IEEE Trans. Antennas Propagat.*, **56**(4), 961–969, 2008.

[64] W. R. Stone. A review and examination of results on uniqueness in inverse problems. *Radio Sci.*, **22**(6), 1026–1030, November 1987.

[65] S. Ström. Introduction to integral representations and integral equations for time-harmonic acoustic, electromagnetic and elastodynamic wave fields. In V. V. Varadan, A. Lakhtakia, and V. K. Varadan, editors, *Field Representations and Introduction to Scattering*, volume 1 of *Handbook on Acoustic, Electromagnetic and Elastic Wave Scattering*, chapter 2, pages 37–141. Elsevier Science Publishers, Amsterdam, 1991.

[66] A. Taaghol and T. K. Sarkar. Near-field to near/far-field transformation for arbitrary near-field geometry, utilizing an equivalent magnetic current. *IEEE Trans. Electromagn. Compatibility*, **38**(3), 536–542, 1996.

[67] F. Thérond, J. C. Bolomey, N. Joachmowicz, and F. Lucas. Electromagnetic diagnosis technique using spherical near-field probing. In *Proc. EUROEM'94*, pages 1218–1226, Bordeaux, France, 1994.

[68] A. R. Tobin, A. D. Yaghjian, and M. M. Bell. Surface integral equation for multi-wavelength, arbitrarily shaped, perfectly conducting bodies. In *Digest of the National Radio Science Meeting (URSI)*, page 9, Boulder, Colorado, 1987.

[69] J. G. van Bladel. *Electromagnetic Fields*. IEEE Press, New York, 2007.

[70] V. V. Varadan and V. K. Varadan. Acoustic, electromagnetic and elastodynamics fields. In V. V. Varadan, A. Lakhtakia, and V. K. Varadan, editors, *Field Representations and Introduction to Scattering*, Acoustic, Electromagnetic and Elastic Wave Scattering, chapter 1, pages 1–35. Elsevier Science Publishers, Amsterdam, 1991.

[71] J. J. H. Wang. An examination of the theory and practices of planar near-field measurement. *IEEE Trans. Antennas Propagat.*, **36**(6), 746–753, 1988.

[72] M. B. Woodworth and A. D. Yaghjian. Derivation, application and conjugate gradient solution of dual-surface integral equations for three-dimensional, multi-wavelength perfect conductors. *Progress in Electromagnetics Research*, **5**, 103–129, 1991.

[73] M. B. Woodworth and A. D. Yaghjian. Multiwavelength three-dimensional scattering with dual-surface integral equations. *J. Opt. Soc. Am. A*, **11**(4), 1399–1413, 1994.

[74] R. G. Yaccarino and Y. Rahmat-Samii. Phaseless bi-polar planar near-field measurements and diagnostics of array antennas. *IEEE Trans. Antennas Propagat.*, **47**(3), 574–583, 1999.

[75] W.-J. Zhao, L.-W. Li, and Y.-B. Gan. Efficient analysis of antenna radiation in the presence of airborne dielectric radomes of arbitrary shape. *IEEE Trans. Antennas Propagat.*, **53**(1), 442–449, 2005.

[76] A. Ziyyat, L. Casavola, D. Picard, and J. C. Bolomey. Prediction of BTS antennas safety perimeter from NF to NF transformation: an experimental validation. In *Proc. Antenna Measurement Techniques Association (AMTA)*, pages 22–26, Denver, US, 2001.

Reconstruction of equivalent currents using a near-field data transformation – with radome applications

Paper I

Kristin Persson and Mats Gustafsson

Abstract

Knowledge of the current distribution on a radome can be used to improve radome design, detect manufacturing errors, and to verify numerical simulations. In this paper, the transformation from near-field data to its equivalent current distribution on a surface of arbitrary material, *i.e.*, the radome, is analyzed. The transformation is based on the scalar surface integral representation that relates the equivalent currents to the near-field data. The presence of axial symmetry enables usage of the fast Fourier transform (FFT) to reduce the computational complexity. Furthermore, the problem is regularized using the singular value decomposition (SVD). Both synthetic and measured data are used to verify the method. The quantity of data is vast since the height of the radome corresponds to $29 - 43$ wavelengths in the frequency interval $8.0 - 12.0$ GHz. It is shown that the method gives an accurate description of the field radiated from an antenna, on a surface enclosing it. Moreover, disturbances introduced by copper plates attached to the radome surface, not localized in the measured near field, are focused and detectable in the equivalent currents.

1   Introduction

There are several applications of a near field to equivalent currents transformation. For example, in the radome industry it is important to have accurate models of the field radiated from the antenna inside the radome. This field cannot be measured directly since the radome often is placed very close to the antenna and at these distances, there is a substantial interaction between the antenna and the measuring probe [5, 10, 16]. Another field of application is in the manufacturing of radiating bodies, *i.e.*, radomes, antenna arrays *etc.*, when the radiation pattern from the body does not exhibit the expected form. By determination of the equivalent currents on the radiating body the malfunctioning areas or components can be found.

A common method, transforming near field to equivalent currents and vice versa, is to use modal-expansions of the electric field [5]. This is a very efficient method for radiating bodies with certain geometrical symmetries, *i.e.*, planar, cylindrical, and spherical. Having a planar aperture the plane wave spectrum of the field is utilized in the back transformation [3, 4]. The fact that the expression of the far field originating from a planar surface is equal to the Fourier transform of the radiating field on the aperture has been investigated in [9, 10]. The paper [9] also illustrates that defects, *i.e.*, patches of Eccosorb, can be detected on the aperture. If the radiating body is of cylindrical or spherical geometry the radial solutions contain cylindrical and spherical Bessel functions while the angular solutions are described by trigonometric functions and the associated Legendre functions, respectively [5, 14]. For general geometrical symmetries, where modal-expansions do not exist, the modal-expansion is not applicable.

Later on different combinations of the electric- and magnetic-field integral equations (EFIE and MFIE) derived from the Maxwell equations, *cf.*, the Method of Moments (MoM), have been used to back propagate fields towards their origin, *i.e.*,

a linear inverse source problem is solved. By this method it is possible to handle a wider class of geometries [10]. In [15] the dual-surface magnetic and electric-field integral equations are investigated. The fields are transformed back to a cubic perfect electric conductor by solving the dual-surface magnetic-field integral equation using the conjugate gradient method. Other work using the integral equations is reported in [11], where the near field is measured on a arbitrary surface and later inverted to a planar perfectly conducting surface by using a singular value decomposition (SVD) for regularization.

In this paper, the approach is to investigate a scalar surface integral representation that does not require the aperture to be a perfect electric or magnetic conductor. The representation provides a relation relating the unknown electric and magnetic equivalent currents on a surface to the measured electric field. An additional relation is given by the fact that the equivalent currents are constructed such that the integral is zero inside the volume, on which surface the currents exist, *i.e.*, the extinction theorem [13].

The integral relations are discretized into matrix linear equations. The matrix equations include an azimuthal convolution which is solved with a fast Fourier transform (FFT) in the angular coordinate. The fast Fourier transform brings down the complexity of the problem, *i.e.*, the original surface-to-surface linear map is decomposed into a set of line-to-line linear maps. A singular value decomposition (SVD) is used to invert each of these linear maps. As most inverse problems it is ill-posed, *i.e.*, small errors in the near-field data can produce large errors in the equivalent currents. Thus, the problem needs to be regularized by suppression of small singular values when inverted.

In this paper, the electric field to be inverted is presumed to be scalar, *i.e.*, the scalar surface integral representation is utilized. The assumption is acceptable since the used near-field data, supplied by SAAB Bofors Dynamics and Chelton Applied Composites, Sweden, clearly have one dominating component in the main lobe, see Figure 3. The measured data is given for three different antenna and radome configurations, *viz.*, antenna, antenna together with radome, and antenna together with defect radome. The height of the radome corresponds to $29 - 43$ wavelengths in the frequency interval $8.0 - 12.0$ GHz.

As a start, synthetic data is used to verify the method. Verification is also performed by a comparison between the measured far field and the far field calculated from the equivalent currents on the radome. The calculated far field agrees well with the measured far field. We show that the method can describe the field radiated from an antenna, on a surface enclosing it. When the radome is introduced the field is scattered and flash lobes arise. The equivalent currents on the radome, that produce the electric field measured in the near-field area, are identified and the flash lobes are accurately detected.

Manufacturing errors, not localized in the measured near-field data, can be focused and detected in the equivalent currents on the radome surface. In this paper, it is shown that the field scattered by copper plates attached on the radome, are focused back towards the original position of the copper plates. The length of the side of the square copper plates is 6 cm, *i.e.*, $1.6 - 2.4$ wavelengths corresponding to
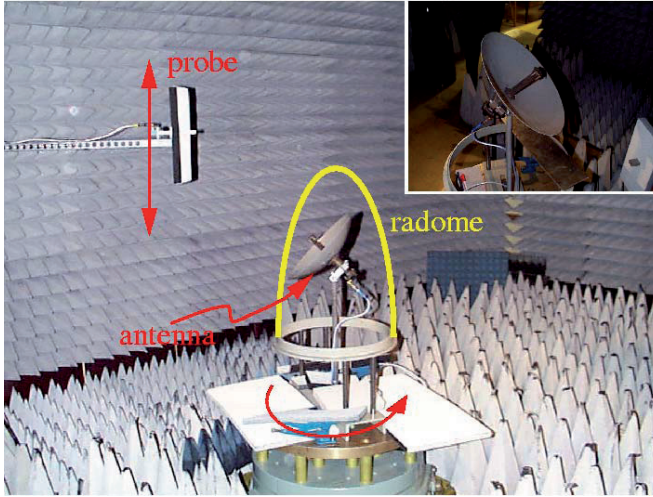
Figure 1:   Photo of the cylindrical near-field range at SAAB Bofors Dynamics, Sweden. The antenna under test is rotated and the probe is moved in the vertical direction. A close up of the reflector antenna is shown in the upper right corner.

the frequency span $8.0 - 12.0$ GHz.

In Section 2 the experimental set-up is described and the measured near-field data is presented. The scalar surface integral representation is introduced and adapted to the specific problem in Section 3. Section 4 discusses the implementation process of the scalar surface integral representation. Results, using synthetic near-field data and the error of the method is elucidated. The results, when using the experimental near-field data, are shown and examined in Section 5. The paper ends with the achieved conclusions in Section 6.

2   Near-field measurements

The near-field data, used in this paper, was supplied by SAAB Bofors Dynamics and Chelton Applied Composites, Sweden. The set-up with relevant dimensions indicated is shown in Figures 1 and 2a. Three different measurements were performed; data measured without the radome, data measured with the radome, and data measured with the defect radome. The defect radome has two copper plates attached to its surface.

A reflector antenna fed by a symmetrically placed wave-guide generates the near-field data, see Figure 1. The diameter of the antenna is 0.32 m and its focal distance is 0.1 m. The main lobe of the antenna is vertically polarized relative to the horizontal plane. The standing wave ratio (SWR) is approximately 1.4 in the frequency range $8.2 - 9.5$ GHz. The antenna is poorly adapted for other frequencies. A 10 dB reflection attenuator is connected to the antenna.
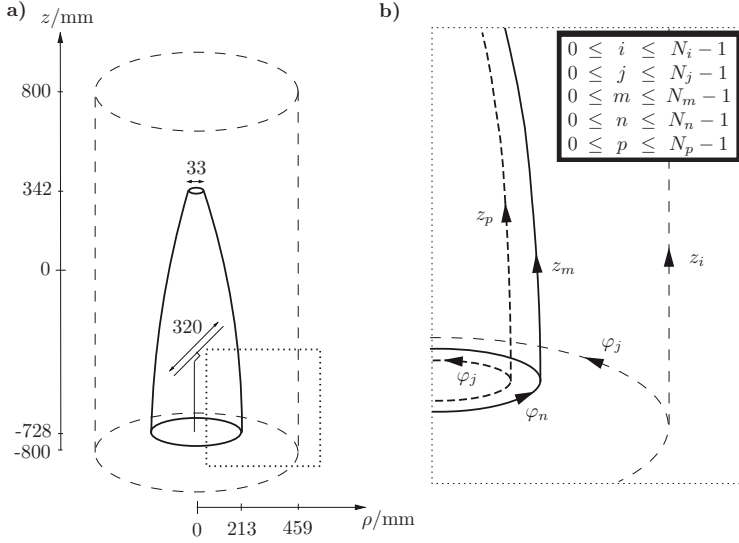
Figure 2: (a) The dimensions of the reflector antenna, the radome, and the cylinder where the electric near field is measured. (b) A close-up showing the discretized geometric variables.

The radome surface is described by

$$\rho(z) = \begin{cases} 0.213\,\text{m} & -0.728\,\text{m} \le z \le -0.663\,\text{m} \\ -(bz' + d) + \sqrt{(bz' + d)^2 - a(z')^2 - 2cz' - e} & -0.663\,\text{m} < z \le 0.342\,\text{m} \end{cases}$$
$$(2.1)$$

where $z' = z + 0.728\,\text{m}$ and the constants are $a = 0.122$, $b = 0.048$, $c = -0.018\,\text{m}$, $d = 0.148\,\text{m}$, and $e = -0.108\,\text{m}^2$. The near-field measurement probe consists of a wave-guide for which no compensation is made in the final data. The cylindrical surface, where the electric field is measured, is placed in both the reactive near-field zone and the radiating near-field zone [2].

The amplitude and phase of the electric field are measured in the frequency interval $8.0 - 12.0\,\text{GHz}$ on a cylindrical surface by moving the probe in the z-direction and rotating the antenna under test, see Figure 1. With this measurement set-up the fields on the top and the bottom of the cylindrical surface could not be collected. It would have been preferable to measure the fields on an infinite cylinder. However, the size of the cylinder is chosen due to the influence of the turntable below the radome and the low field amplitudes above $z = 800\,\text{mm}$, *cf.*, Figures 2a and 3. In angle, 120 points are measured between $-180°$ and $180°$ in steps of $3°$. The z-dimension is divided into 129 points, every two points separated by $12.5\,\text{mm}$. This means that at $8.0\,\text{GHz}$ the electric field is measured 3 times per wavelength, in the z-direction, and 1.5 times per wavelength, in the angular direction, respectively. Together, a total of $120 \times 129 = 15480$ measurement points are used for each radome
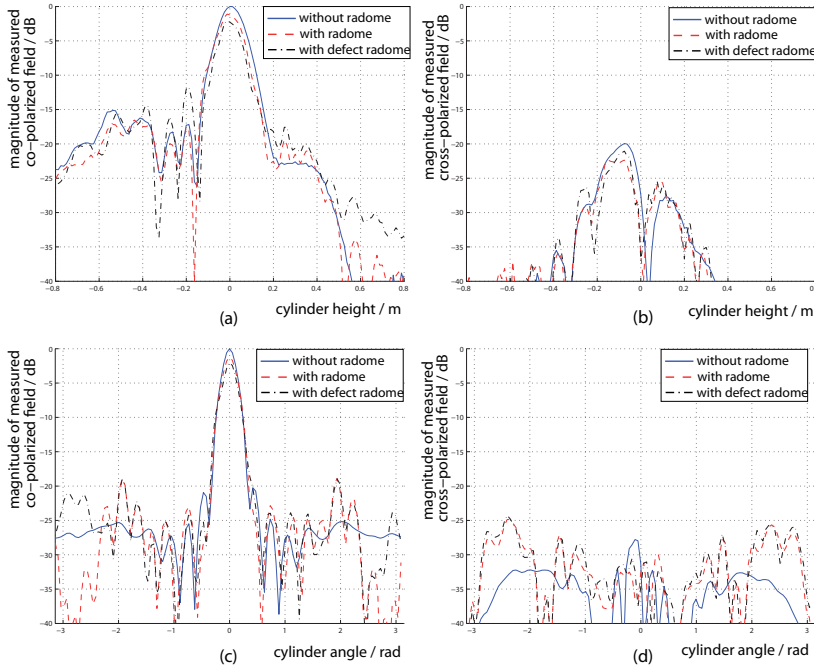
Figure 3: The measured co- and cross-polarized electric field on the measurement cylinder at 8.0 GHz. In (a) and (b) the angle is fixed at $\varphi = 0$, and the fields are normalized to the maximum value when no radome is present in (a). In (c) and (d) the height is fixed at $z = 0$, and the fields are normalized to the maximum value when no radome is present in (c).

configuration and frequency. The co- and cross-polarized measured electric fields are shown in Figure 3. The differences between the three different antenna and radome cases arise from constructive and destructive interference between the radiated field and the scattered field. In Figure 3 it is also observed that the electric field consists of a dominating co-component in the main lobe, *i.e.*, a dominating z-component since the antenna is vertically polarized.

3   The surface integral representation

The surface integral representation expresses the electromagnetic field in a homogeneous and isotropic region in terms of its values on the bounding surface. The representation states that if the electromagnetic field on a surface of a volume is known, the electromagnetic field in the volume can be determined [7, 13]. The representation is derived starting from the time harmonic Maxwell equations with the time convention $e^{i\omega t}$. The Maxwell equations transform into the vector Helmholtz

equation

$$\nabla^2 \boldsymbol{E}(\boldsymbol{r}) + k^2 \boldsymbol{E}(\boldsymbol{r}) = 0 \tag{3.1}$$

since the material (air) is source free, homogeneous, and isotropic.

Assume that the electric field only consists of a component in the z-direction. This is a good approximation dealing with the specific measurements described in Section 2 since our prime interest is to reconstruct the electric field in the main lobe, where the z-component is clearly the dominating one, *cf.*, Figure 3.

Working with a scalar field, the surface integral representation only depends on the scalar electric field, E_z, and its normal derivative, $\partial E_z/\partial n$, *i.e.*, the magnetic field is not taken into account as it must in the full three dimensional expression [7]. The scalar surface integral representation is derived using the free space Green's function $g(\boldsymbol{r}, \boldsymbol{r}') = \mathrm{e}^{-ik|\boldsymbol{r}-\boldsymbol{r}'|}/4\pi|\boldsymbol{r}-\boldsymbol{r}'|$ [13]

$$\iint\limits_{S} \left[\frac{\partial g(\boldsymbol{r}, \boldsymbol{r}')}{\partial n} E_z(\boldsymbol{r}) - g(\boldsymbol{r}, \boldsymbol{r}') \frac{\partial E_z(\boldsymbol{r})}{\partial n} \right] \mathrm{d}S = \begin{cases} -E_z(\boldsymbol{r}') & \boldsymbol{r}' \in V \\ 0 & \boldsymbol{r}' \notin V \end{cases} \tag{3.2}$$

where V is the volume spanning from the outside of the radome to infinity. The closed surface S is the radome surface with an added top and bottom surface. Observe that the electric field does not have to be zero outside the volume, *i.e.*, inside the radome. The surface integral representation (3.2) only states that the left-hand side of the equation is zero if the vector $\boldsymbol{r}'$ points outside the volume V, *i.e.*, the extinction theorem [13].

The equivalent surface currents are introduced as

$$M(\boldsymbol{r}) \equiv E_z(\boldsymbol{r}) \quad \text{and} \quad M'(\boldsymbol{r}) \equiv \frac{\partial E_z(\boldsymbol{r})}{\partial n} \tag{3.3}$$

which are inserted in (3.2) to give

$$\iint\limits_{\text{radome}} \left[\frac{\partial g(\boldsymbol{r}, \boldsymbol{r}')}{\partial n} M(\boldsymbol{r}) - g(\boldsymbol{r}, \boldsymbol{r}') M'(\boldsymbol{r}) \right] \mathrm{d}S = \begin{cases} -E_z^{\text{cyl}}(\boldsymbol{r}') & \boldsymbol{r}' \in \text{cylinder} \\ 0 & \boldsymbol{r}' \in \text{surface inside radome} \end{cases}$$

$$\tag{3.4}$$

where E_z^{cyl} is the z-component of the electric field on the measurement cylinder. The continuous variables are discretized to give linear matrix equations. The discretized cylindrical coordinate system is described by the integer indices displayed in Figure 2b.

3.1 Angular Fourier transformation

The transformation, the Green's function, is axially symmetric due to the measurement set-up, see Section 2. Observe that the symmetry only applies to the transformation, not to the electric field. Thus, the left-hand side in (3.4) represents a convolution and by using a Fourier transformation of the angle coordinate the computational complexity can be brought down one dimension. This reduction of

one dimension, can be understood by writing the left-hand side in (3.4) as a matrix X. This matrix is a circulant matrix, *i.e.*, every row is shifted one step to the right compared to the previous row. The eigenvectors of all circulant matrices are the column vectors of the Fourier matrix F. When a circulant matrix is multiplied with the Fourier matrix. *i.e.*, performing the Fourier transformation, the result is $FX = F\Lambda$ where Λ is a diagonal matrix, which can be seen as a reduction of one dimension [12].

Discretization and Fourier transformation, in the angle coordinate, of (3.4) give

$$\sum_{m=0}^{N_m-1}\left[\widehat{\mathcal{G}}'_{im\hat{\jmath}}\widehat{M}_{m\hat{\jmath}}\ -\widehat{\mathcal{G}}_{im\hat{\jmath}}\widehat{M}'_{m\hat{\jmath}}\right] = -\widehat{E}^{\text{cyl}}_{i\hat{\jmath}}\qquad\text{for all }\ i,\hat{\jmath}\qquad(3.5)$$

and

$$\sum_{m=0}^{N_m-1}\left[\widehat{\mathsf{G}}'_{pm\hat{\jmath}}\widehat{M}_{m\hat{\jmath}}\ -\widehat{\mathsf{G}}_{pm\hat{\jmath}}\widehat{M}'_{m\hat{\jmath}}\right] = 0\qquad\text{for all }\ p,\hat{\jmath}\qquad(3.6)$$

where $\mathcal{G}$ and G are the surface integrals, taken over the radome, of the Green's function multiplied with the basis functions used in the discretization process. $\mathcal{G}$ has the discretized space variable $\boldsymbol{r}'$ belonging to the measurement cylinder and G has the discretized space variable $\boldsymbol{r}'$ belonging to a surface inside the radome, respectively. The prime denotes the normal derivative of the Green's function, $\hat{\jmath}$ is the integer index belonging to the Fourier transformed angle component, and the "hat" denotes the Fourier transformed variables. The summation limits N_m and N_p are described in Figure 2b. To solve the scalar surface integral representation, a limit process of equation (3.6) should be performed by forcing the fictitious surface inside the radome towards the radome surface [2, 8]. However, in our attempt to find a simple and feasible method to allocate the surface current the use of the extinction theorem as an approximate solution to the integral representation in equation (3.6) is sufficient.

Reduction of M' in (3.5) and (3.6) gives

$$\sum_{m=0}^{N_m-1}\left\{\widehat{\mathcal{G}}'_{im\hat{\jmath}} - \sum_{p=0}^{N_p-1}\sum_{q=0}^{N_m-1}\widehat{\mathcal{G}}_{iq\hat{\jmath}}(\widehat{\mathsf{G}}^{-1})_{qp\hat{\jmath}}\widehat{\mathsf{G}}'_{pm\hat{\jmath}}\right\}\widehat{M}_{m\hat{\jmath}}\ = -\widehat{E}^{\text{cyl}}_{i\hat{\jmath}}\quad\text{for all }i,\hat{\jmath}\qquad(3.7)$$

Equation (3.7) can also be written as $\hat{\jmath}$ matrix equations

$$\widehat{\boldsymbol{G}}^{\text{radome}}_{\hat{\jmath}}\ \widehat{\boldsymbol{M}}_{\hat{\jmath}}\ = -\widehat{\boldsymbol{E}}^{\text{cyl}}_{\hat{\jmath}}\qquad\text{for all }\ \hat{\jmath}\qquad(3.8)$$

where the matrices are defined as $\widehat{\boldsymbol{M}}_{\hat{\jmath}} \equiv [\widehat{M}_{m1}]_{\hat{\jmath}}$, $\widehat{\boldsymbol{E}}^{\text{cyl}}_{\hat{\jmath}} \equiv [\widehat{E}^{\text{cyl}}_{i1}]_{\hat{\jmath}}$, and

$$\widehat{\boldsymbol{G}}^{\text{radome}}_{\hat{\jmath}}\ \equiv [\widehat{\mathcal{G}}'_{im}]_{\hat{\jmath}} - [\widehat{\mathcal{G}}_{im}]_{\hat{\jmath}}[\widehat{\mathsf{G}}_{mp}]^{-1}_{\hat{\jmath}}[\widehat{\mathsf{G}}'_{pm}]_{\hat{\jmath}}\qquad(3.9)$$

The notation of matrices used here is that of [1].

3.2   Inversion with singular value decomposition

Since the matrices $\widehat{\boldsymbol{G}}_{\hat{\jmath}}^{\mathrm{radome}}$ and $[\widehat{\mathsf{G}}_{mp}]_{\hat{\jmath}}$ in (3.8) and (3.9) are not quadratic, a regular inversion cannot be performed. A fast and easy way to solve this is to use the singular value decomposition (SVD) [12]. This method is used on both matrices, but the SVD-equations are only given here for $\widehat{\boldsymbol{G}}_{\hat{\jmath}}^{\mathrm{radome}}$. The matrix system (3.8) can then be rewritten as

$$\widehat{\boldsymbol{U}}_{\hat{\jmath}}\widehat{\boldsymbol{S}}_{\hat{\jmath}}\widehat{\boldsymbol{V}}_{\hat{\jmath}}^{\dagger}\widehat{\boldsymbol{M}}_{\hat{\jmath}} = -\widehat{\boldsymbol{E}}_{\hat{\jmath}}^{\mathrm{cyl}} \qquad \text{for all } \hat{\jmath} \tag{3.10}$$

where $\widehat{\boldsymbol{V}}_{\hat{\jmath}}^{\dagger}$ denotes the Hermitian conjugate of $\widehat{\boldsymbol{V}}_{\hat{\jmath}}$. Both $\widehat{\boldsymbol{U}}_{\hat{\jmath}}$ and $\widehat{\boldsymbol{V}}_{\hat{\jmath}}$ are orthogonal matrices. $\widehat{\boldsymbol{S}}_{\hat{\jmath}}$ is a diagonal matrix consisting of the singular values to $\widehat{\boldsymbol{G}}_{\hat{\jmath}}^{\mathrm{radome}}$ in decreasing order. The singular values of both $\widehat{\boldsymbol{G}}_{\hat{\jmath}}^{\mathrm{radome}}$ and $[\widehat{\mathsf{G}}_{mp}]_{\hat{\jmath}}$ exhibit the tendency shown by the curves in Figure 4a.

A cut-off value δ normalized to the operator L$_2$-norm of $\widehat{\boldsymbol{G}}_{1}^{\mathrm{radome}}$ is chosen. The operator L$_2$-norm of $\widehat{\boldsymbol{G}}_{1}^{\mathrm{radome}}$ is equal to the largest singular value (σ_1) of the largest Fourier transformed angle component [8]. All singular values smaller than δ are ignored during the inversion of $\widehat{\boldsymbol{S}}_{\hat{\jmath}}$ and are afterwards set to zero. If this is not done the small singular values create an uncontrolled growth of non-radiation currents when inverted. The mathematical formulation then fails since very small electric field contributions become dominating. Performing the inversion of (3.10) gives

$$\widehat{\boldsymbol{M}}_{\hat{\jmath}} = -\widehat{\boldsymbol{U}}_{\hat{\jmath}}^{\dagger}\widehat{\boldsymbol{S}}_{\hat{\jmath}}^{-1}\widehat{\boldsymbol{V}}_{\hat{\jmath}}\widehat{\boldsymbol{E}}_{\hat{\jmath}}^{\mathrm{cyl}} \qquad \text{for all } \hat{\jmath} \tag{3.11}$$

Before the system of equations is solved it is necessary to convert it back from Fourier space by an inverse Fourier transformation

$$\boldsymbol{M}_{j} = \mathcal{F}^{-1}\left[-\widehat{\boldsymbol{U}}_{\hat{\jmath}}^{\dagger}\widehat{\boldsymbol{S}}_{\hat{\jmath}}^{-1}\widehat{\boldsymbol{V}}_{\hat{\jmath}}\widehat{\boldsymbol{E}}_{\hat{\jmath}}^{\mathrm{cyl}}\right] \qquad \text{for all } j, \hat{\jmath} \tag{3.12}$$

where j, as before, denotes the integer index belonging to the discretized angle component, see Figure 2b.

4   Implementation

Some adjustments of the formulas are made in the implementation process. To facilitate the calculations, the radome surface is reshaped into a closed surface by adding a smooth top and bottom surface. These extra surfaces are useful since the measurements are performed under non-ideal conditions. The table, on which the antenna and radome are placed, see Figure 1, reflects some of the radiation, which is taken care of by the bottom surface. The top surface represents the electric field that is reflected on the inside of the radome and then is passed out through the top hole. If these factors are not considered, unwanted edge effects occur since the
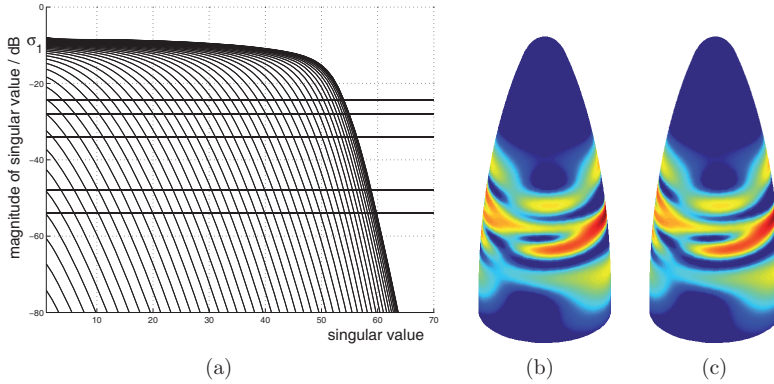
Figure 4: (a) The tendency of singular values of $\widehat{\boldsymbol{G}}_{\hat{\jmath}}^{\text{radome}}$ and $[\widehat{\mathsf{G}}_{mp}]_{\hat{\jmath}}$. Every curve represents the singular values of a Fourier transformed angle component, *i.e.*, different $\hat{\jmath}$. The horizontal lines describe the cut-off values $\delta = \sigma_1[0.15\ 0.1\ 0.05\ 0.01\ 0.005]$. (b) The synthetic equivalent current, originating from three dipoles, in dB-scale $[-15, 0]$, normalized to the highest current value, *i.e.*, the maximum current magnitude in figure c. (c) The reconstructed current in dB-scale $[-15, 0]$, normalized to its highest current value.

electric field originating from the table and the top of the radome is forced to arise from the radome itself.

The measured electric near field is only measured 1.5 times per wavelength, in the angular direction, at the frequency 8.0 GHz, see Section 2. To be sure that the equivalent currents on the radome are recreated in an accurate way it is necessary to have a high sample density on the radome. This is achieved by increasing the number of discrete points, in the angular direction, on the radome surface by including extra angles between the already existing ones. Thus, the axial symmetry of the Green's transformation is kept. The sample density on the measurement cylinder contributes very little to the total error. The scalar surface integral representation creates currents on the radome such that the electric field is correct at the measurement points. However, if the Nyquist theorem is fulfilled, then the electric field is correct at all points on the measurement surface, *i.e.*, not only at the measurement points. As mentioned before, the problem is vast and the matrix $\widehat{\boldsymbol{G}}$, *cf.*, (3.9), has approximately 10^8 elements at the frequency 8.0 GHz when the sample density is 10 points per wavelength both in the angular direction and in the z-direction on the radome.

To verify and find the error of the method, synthetic data is used. A synthetic electric field, originating from three dipoles inside the radome is shown in Figure 4b. The corresponding reconstructed current on a surface shaped as the radome is shown in Figure 4c where the sample density is 10 points per wavelength both in the z-direction and in the angular direction. The inner fictitious surface is located one wavelength from the radome surface.

The error as a function of the Fourier transformed angle component is defined

as

$$\text{Err}(\hat{\jmath}) = 20 \log_{10} \frac{\| \ \widehat{\boldsymbol{M}}_{\hat{\jmath}} - \widehat{\boldsymbol{M}}_{\hat{\jmath}}^{\text{correct}} \ \|_2}{\| \ \widehat{\boldsymbol{M}}_{\hat{\jmath}}^{\text{correct}} \ \|_2} \tag{4.1}$$

$$= 20 \log_{10} \frac{\sqrt{\sum_{m=0}^{N_m-1} \ | \ \widehat{M}_{m\hat{\jmath}} - \widehat{M}_{m\hat{\jmath}}^{\text{correct}} \ |^2 \ \Delta S_m}}{\sqrt{\sum_{m=0}^{N_m-1} \ | \ \widehat{M}_{m\hat{\jmath}}^{\text{correct}} \ |^2 \ \Delta S_m}} \quad \text{for all } \hat{\jmath} \tag{4.2}$$

where the matrix definition in (3.8) is used and ΔS_m denotes the discretized area elements on the radome.

By using synthetic data and choosing appropriate cut-off values δ the error is shown to be below -60 dB for each existing Fourier transformed angle component. To obtain these low error levels, the measurement surface must be closed, *i.e.*, field values at the top and bottom surfaces of the cylindrical measurement surface must be included. The cut-off values depend on the complexity of the specific measurement set-up and must be investigated for each new set-up.

The total error of the scalar surface integral representation using the measured near field described in Section 2 is hard to define since the noise level and the amount of field spread outside the measurement cylinder are unknown parameters. Instead we rely on the fact that the method handles synthetic data well and that the results using measured data is satisfactory, see Section 5.

5   Results using measured near-field data

The measured near-field data, described in Section 2, is investigated. The inner fictitious surface is located one wavelength from the radome surface. The sample density on the radome is 10 points per wavelength both in the angular direction and in the z-direction. The cut-off values are determined in accordance with the discussion in Section 4.

Three different measurement configurations are investigated, *viz.*, antenna, antenna together with radome, and antenna together with defect radome. The studied frequency interval is $8.0 - 12.0$ GHz. The results for the different measurement configurations are shown in Figure 5a at the frequencies 8.0 GHz and 10.0 GHz. In Figure 5b the results for the defect radome case are shown for the frequencies 8.0 GHz, 9.0 GHz, 10.0 GHz, 11.0 GHz, and 12.0 GHz, respectively.

In the case when no radome is placed around the antenna the equivalent current is calculated on a surface shaped as the radome, see Figure 5aa' and 5ad'. The figures show that the near field close to the antenna is complex and hard to predict, *i.e.*, the diffraction pattern must be taken into account. The diffraction is explained as environmental reflections and an off-centered antenna feed.

The case when the radome is present, see Figure 5ab' and 5ae', shows in comparison to the case without radome that the used radome interacts with the antenna and hence disturbs the radiated field. However, the currents in the main lobe are hardly affected by the radome, as seen in Figure 6a. The influence of the radome is

Figure 5: The reconstructed currents in dB-scale $[-30, 0]$, all normalized to the highest current value, *i.e.*, the maximum current magnitude in figure ac'. (a) The different measurement configurations are depicted at two different frequencies. From left to right; antenna without radome, antenna together with radome, and antenna together with defect radome, respectively. The arrows point out the location of the copper plates on the defect radome. (b) The defect radome case, shown at different frequencies.

clearly visible in the reconstructed currents on the back of the radome where flash lobes occur, see Figure 6b.

The defect radome has two copper plates attached to its surface. These are placed in the forward direction of the main lobe of the antenna and centered at the heights 41.5 cm and 65.5 cm above the bottom of the radome. The length of the side of the squared copper plates is 6 cm, which corresponds to 1.6 wavelengths at 8.0 GHz and 2.4 wavelengths at 12.0 GHz, respectively. The locations of the copper plates are detected as shown in Figure 5ac' and 5af', where the lower plate appears clearly. The other plate is harder to discern since it is placed in a region with small current magnitudes. However, a cross section graph through the main lobe detects even this copper plate, see Figure 6a. Observe that the effects of the copper plates cannot be localized directly in the near-field data, compare Figure 6a to Figure 3a. The near-field data only shows that the field is disturbed, not the location of the disturbance. Nevertheless, by using the scalar surface integral representation the effects of the plates are localized and focused. The defect radome also increases the backscattering as seen in Figure 6b. Due to the copper plates the flash lobes are different compared to the case with the non-defect radome.
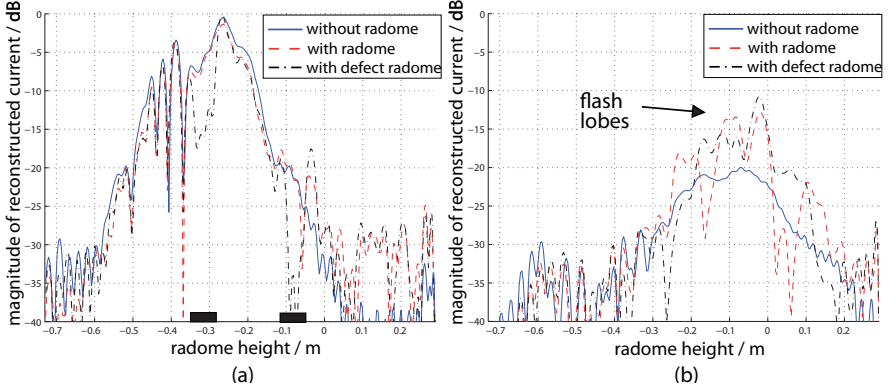
Figure 6: Cross section of the reconstructed current on the radome surface for the different measurement configurations, at 8.0 GHz. The current is shown as functions of the radome height for a fixed angle. All graphs are normalized to the highest current value, *i.e.*, the maximum current for the defect radome. (a) The graph representing the currents in the main lobe, *i.e.*, the front of the radome. The position of the copper plates are marked as thick lines on the horizontal axis. (b) The currents on the back of the radome.

As a final verification, the far-field amplitude on a sphere in the far-field region is studied. The electric field, originating from the equivalent currents on the radome, is calculated on the sphere,

$$\boldsymbol{E}_j^{\text{sph}} = -\mathcal{F}^{-1}\left[\widehat{\boldsymbol{G}}_{\hat{j}}\widehat{\boldsymbol{M}}_{\hat{j}}\right] \qquad \text{for all } j, \hat{j} \tag{5.1}$$

in accordance with (3.8) and (3.12), except that $\widehat{\boldsymbol{G}}_{\hat{j}}$ now describes the transformation from the radome to the inner fictitious surface and the far field sphere, respectively. The denotions j and $\hat{j}$ are, as before, the integer index belonging to the discretized angle component and the Fourier transformed discretized angle component, respectively.

The far-field amplitude F is derived as

$$F(\theta, \phi) = kr\, e^{\text{i}kr} E^{\text{sph}}(r, \theta, \phi) \qquad \text{as } r \to \infty \tag{5.2}$$

where (r, θ, ϕ) describes the spherical coordinate system [6]. The result is compared with far-field data, supplied by Chelton Applied Composites, as shown in Figure 7. The far field is depicted for the angles $\phi = 0$ and $\phi = \pi$, *i.e.*, a cross-section through the far field of the main lobe and the corresponding far field originating from the currents on the back of the radome. There is a lack of agreement between the measured far field and the calculated one in the angles corresponding to the top of the radome,*i.e.*, $\theta \approx 0$. This is due to the fact that fields originating hereof are not all included in the measured near-field data, since the measurement surface is a
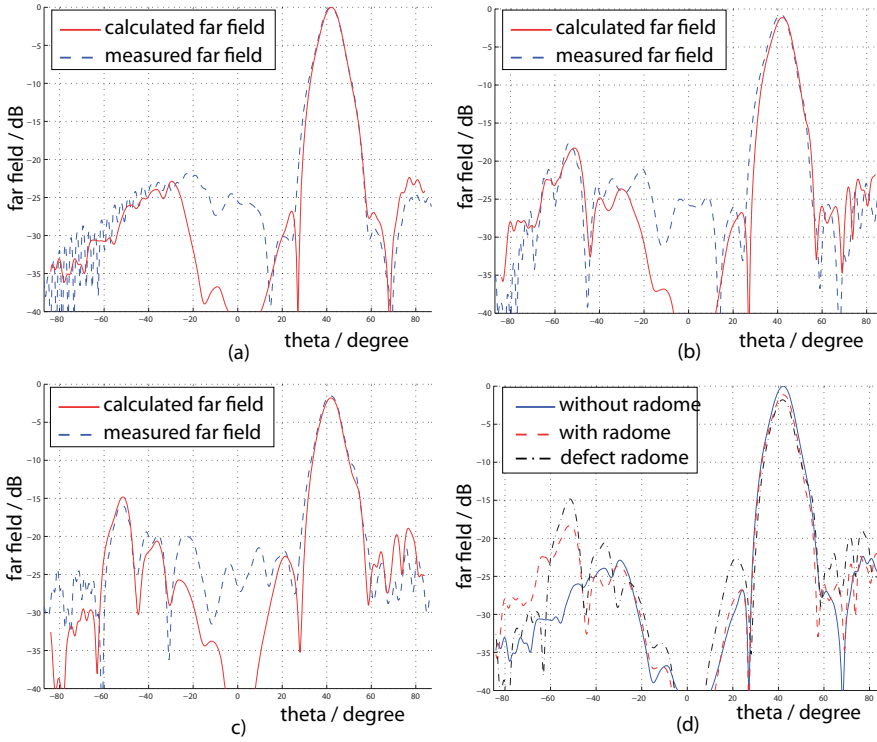
Figure 7:   Comparison between the measured far-field data, supplied by Chelton Applied Composites, and the far field calculated from the equivalent currents on the radome surface. The far fields are normalized to the maximum value of the far field when no radome is present. (a) Antenna without radome. (b) Antenna together with radome. (c) Antenna together with defect radome. (d) The calculated far-field pattern for the three measurement configurations.

cylinder, see Figure 2a. The fact that the radome disturbs and reflects the electric field, as earlier seen in Figure 6b, can also be detected in the far field, see Figure 7d, where flash lobes appear when the radome is present.

6   Discussion and conclusions

The used scalar surface integral representation gives a linear map between the equivalent currents and the near-field data for general structures. It is here shown that this map can be inverted for axially symmetric geometries. The model can theoretically be adapted to geometries lacking symmetry axes. Although it is not a feasible approach for radome applications, demanding large quantities of measured data, with the present computer capacity.

The transformation method is stable and useful in radome design and for evaluation purposes. To investigate the electric field passing through the radome, the current distribution on the antenna or on a surface enclosing the antenna must be known. Using the surface integral representation, the equivalent currents, on a surface enclosing the antenna, can be described.

Another range of application within the radome industry is to study how *e.g.*, lightning conductors and Pitot tubes, often placed on radomes, influence the equivalent currents. We show that such influences and the field effects of the radome itself can be detected. In this paper, copper plates are attached on the radome, in the direction of the antenna main lobe. The length of the side of the square copper plates are $1.6 - 2.4$ wavelengths, corresponding to the frequency span $8.0 - 12.0$ GHz. The effects of the plates cannot be localized directly by using the near-field data, but by using the equivalent currents the effects are focused and detected on the radome surface. Thus, by transforming the near-field data to the radome surface, field defects introduced by the radome and other disturbances are focused back to their origins.

It is concluded that the transformation method based on the surface integral representation works very well and that the field of applications is large. A natural continuation is to elaborate the algorithm by including near field data with cross-polarization, *i.e.*, to implement the full Maxwell equations with a Method of Moments (MoM). Nevertheless, if the measured near-field data consists of one dominating component the use of the full Maxwell equations are not necessary, as shown in this paper.

Additional aspects to be investigated more thoroughly in the future are the resolution possibilities of manufacturing errors and other external field influences. Analysis of the phase information in the equivalent currents is also of interest. Moreover, a study regarding the detection of different materials attached to the radome surface is desirable.

Acknowledgments

References

[1] H. Anton. *Elementary Linear Algebra*. John Wiley & Sons, New York, 7 edition, 1994.

[2] C. A. Balanis. *Antenna Theory.* John Wiley & Sons, New York, second edition, 1997.

[3] L. E. Corey and E. B. Joy. On computation of electromagnetic fields on planar surfaces from fields specified on nearby surfaces. *IEEE Trans. Antennas Propagat.*, **29**(2), 402–404, 1981.

[4] J. Hanfling, G. Borgiotti, and L. Kaplan. The backward transform of the near field for reconstruction of aperture fields. *IEEE Antennas and Propagation Society International Symposium*, **17**, 764–767, 1979.

[5] J. E. Hansen, editor. *Spherical Near-Field Antenna Measurements.* Number 26 in IEE electromagnetic waves series. Peter Peregrinus Ltd., Stevenage, UK, 1988. ISBN: 0-86341-110-X.

[6] J. D. Jackson. *Classical Electrodynamics.* John Wiley & Sons, New York, second edition, 1975.

[7] D. S. Jones. *Acoustic and Electromagnetic Waves.* Oxford University Press, New York, 1986.

[8] R. Kress. *Linear Integral Equations.* Springer-Verlag, Berlin Heidelberg, second edition, 1999.

[9] J. Lee, E. M. Ferren, D. P. Woollen, and K. M. Lee. Near-field probe used as a diagnostic tool to locate defective elements in an array antenna. *IEEE Trans. Antennas Propagat.*, **36**(6), 884–889, 1988.

[10] Y. Rahmat-Samii, L. I. Williams, and R. G. Yaccarino. The UCLA bi-polar planar-near-field antenna-measurement and diagnostics range. *IEEE Antennas and Propagation Magazine*, **37**(6), 16–35, December 1995.

[11] T. K. Sarkar and A. Taaghol. Near-field to near/far-field transformation for arbitrary near-field geometry utilizing an equivalent electric current and MoM. *IEEE Trans. Antennas Propagat.*, **47**(3), 566–573, March 1999.

[12] G. Strang. *Introduction to applied mathematics.* Wellesley-Cambridge Press, Box 157, Wellesley MA 02181, 1986.

[13] S. Ström. Introduction to integral representations and integral equations for time-harmonic acoustic, electromagnetic and elastodynamic wave fields. In V. V. Varadan, A. Lakhtakia, and V. K. Varadan, editors, *Field Representations and Introduction to Scattering*, volume 1 of *Handbook on Acoustic, Electromagnetic and Elastic Wave Scattering*, chapter 2, pages 37–141. Elsevier Science Publishers, Amsterdam, 1991.

[14] V. V. Varadan, Y. Ma, V. K. Varadan, and A. Lakhtakia. Scattering of waves by spheres and cylinders. In V. V. Varadan, A. Lakhtakia, and V. K. Varadan,

editors, *Field Representations and Introduction to Scattering*, volume 1 of *Handbook on Acoustic, Electromagnetic and Elastic Wave Scattering*, chapter 4, pages 211–324. Elsevier Science Publishers, Amsterdam, 1991.

[15] M. B. Woodworth and A. D. Yaghjian. Derivation, application and conjugate gradient solution of dual-surface integral equations for three-dimensional, multi-wavelength perfect conductors. *Progress in Electromagnetics Research*, **5**, 103–129, 1991.

[16] A. D. Yaghjian. An overview of near-field antenna measurements. *IEEE Trans. Antennas Propagat.*, **34**(1), 30–45, January 1986.

Reconstruction of equivalent currents using the scalar surface integral representation

Kristin Persson and Mats Gustafsson

Paper II

Abstract

Knowledge of the current distribution on a radome can be used to improve radome design, detect manufacturing errors, and to verify numerical simulations. In this paper, the transformation from near-field data to its equivalent current distribution on a surface of arbitrary material, *i.e.*, the radome, is analyzed. The transformation is based on the scalar surface integral representation that relates the equivalent currents to the near-field data. The presence of axial symmetry enables usage of the fast Fourier transform (FFT) to reduce the computational complexity. Furthermore, the problem is regularized using the singular value decomposition (SVD). Both synthetic and measured data are used to verify the method. The quantity of data is large since the height of the radome corresponds to $29 - 43$ wavelengths in the frequency interval $8.0 - 12.0$ GHz. It is shown that the method gives an accurate description of the field radiated from an antenna, on a surface enclosing it. Moreover, disturbances introduced by copper plates attached to the radome surface, not localized in the measured near field, are focused and detectable in the equivalent currents. The method also enables us to determine the phase shift of the field due to the passage of the radome, *cf.*, the insertion phase delay.

1   Introduction

This paper provides a wrap-up and a final report of the reconstruction of equivalent currents in the scalar approximation. The theoretical derivation is a summary of the work [11]. The new aspect in this report is mainly the analysis of the measured near-field data, especially the investigation of the phase information. Different ways of visualizing the results are also discussed and presented.

1.1   Ranges of application

There are several applications of a near field to equivalent currents transformation. For example, in the radome industry it is important to have accurate models of the field radiated from the antenna placed inside the radome. It is hard to measure this field directly since the radome often is located very close to the antenna and at these distances, there is a substantial interaction between the antenna and the measuring probe [6, 13, 19]. It is also important to have a powerful tool to determine the insertion phase delay (IPD), also known as the electrical thickness of the radome. The IPD is often one of the specified qualities given to characterize a radome. One way to measure the IPD is to place two horn antennas in such a way that the incident angle on the radome coincide with the Brewster angle, which is the angle where the transmitted field has its highest value [12]. To get the IPD, the phase of the transmitted field is subtracted from the phase of the measured field with no radome between the horn antennas. This process is very time consuming since it has to be repeated several times to cover the whole radome surface. Using the scalar surface integral equation, the phase shift due to the propagation through the radome is determined.

Another field of application is in the manufacturing of radiating bodies, *i.e.*, antenna arrays *etc.*, when the radiation pattern from the body does not exhibit the expected form. By determination of the equivalent currents on the radiating body, the malfunctioning areas or components can be found.

1.2   History

A common method, transforming near field to equivalent currents and vice versa, is to use modal-expansions of the electric field [6]. This is a very efficient method for radiating bodies with certain geometrical symmetries, *i.e.*, planar, cylindrical, and spherical. Having a planar aperture, the plane wave spectrum of the field is utilized in the back transformation [3, 5]. The fact that the expression of the far field originating from a planar surface is equal to the Fourier transform of the radiating field on the aperture has been investigated in [10, 13]. The paper [10] also illustrates that defects, *i.e.*, patches of Eccosorb, can be detected on the aperture. If the radiating body is of cylindrical or spherical geometry, the radial solutions contain cylindrical and spherical Bessel functions, while the angular solutions are described by trigonometric functions and the associated Legendre functions [6, 17]. For general geometrical symmetries, where modal-expansions do not exist, the modal-expansion is less applicable.

Moreover, different combinations of the electric- and magnetic-field integral equations (EFIE and MFIE) derived from the Maxwell equations, have been used to back propagate fields towards their sources, *i.e.*, a linear inverse source problem is solved. By this method it is possible to handle a wider class of geometries [13]. In [18] the dual-surface, magnetic and electric-field integral equations are investigated. The fields are transformed back to a cubic perfect electric conductor by solving the dual-surface magnetic-field integral equation using the conjugate gradient method. Other work using the integral equations is reported in [14], where the near field is measured on a arbitrary surface and later inverted to a planar, perfectly conducting surface by using a singular value decomposition (SVD) for regularization.

1.3   The scalar surface integral representation

In this paper, the approach is to investigate a scalar surface integral representation that does not require the aperture to be a perfect electric or magnetic conductor. The representation provides a relation relating the unknown electric and magnetic equivalent currents on a surface to the measured electric field. An additional relation is given by the fact that the equivalent currents are constructed such that the integral is zero inside the volume, on which surface the currents exist, *i.e.*, the extinction theorem [16].

The integral relations are discretized into matrix linear equations. The matrix equations include an azimuthal convolution which is solved with a fast Fourier transform (FFT) in the angular coordinate. The fast Fourier transform brings down the complexity of the problem, *i.e.*, the original surface-to-surface linear map is decomposed into a set of line-to-line linear maps. A singular value decomposition (SVD)
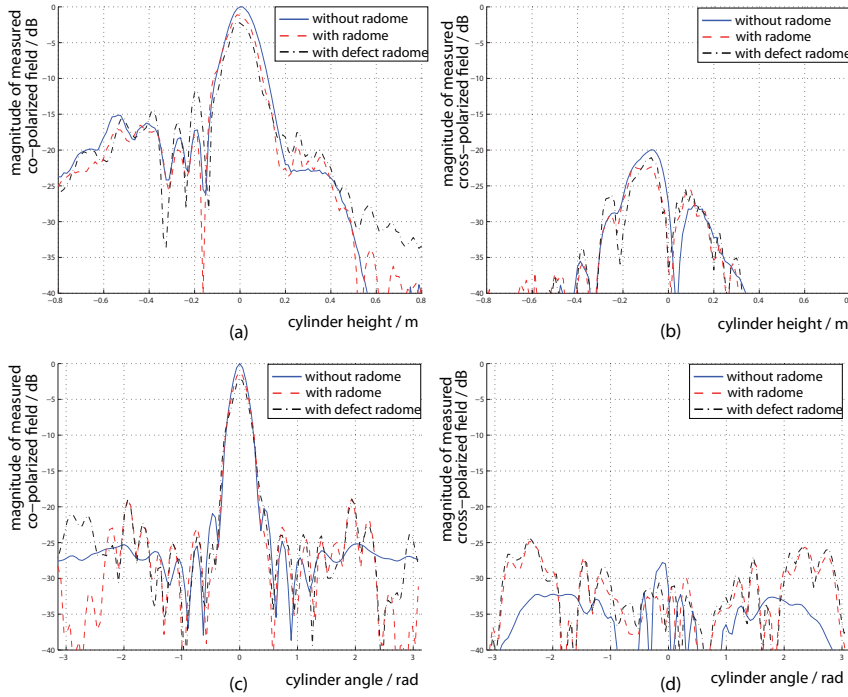
Figure 1: The measured co- and cross-polarized electric field on the measurement cylinder at 8.0 GHz. In (a) and (b) the angle is fixed at $\varphi = 0$, and the fields are normalized by the maximum value when no radome is present in (a). In (c) and (d) the height is fixed at $z = 0$, and the fields are normalized to the maximum value when no radome is present in (c).

is used to invert each of these linear maps. As most inverse problems it is ill-posed, *i.e.*, small errors in the near-field data can produce large errors in the equivalent currents. Thus, the problem needs to be regularized by suppression of small singular values when inverted.

1.4   Results

In this paper, the measured electric field is presumed to be scalar, *i.e.*, the scalar surface integral representation is utilized. The assumption is acceptable since the used near-field data, supplied by SAAB Bofors Dynamics and Applied Composites AB, Sweden, clearly have one dominating component in the main lobe, see Figure 1. The measured data is given for three different antenna and radome configurations, *viz.*, antenna, antenna together with radome, and antenna together with defect radome. The measurement set-up is shown in Figure 2. The height of the radome
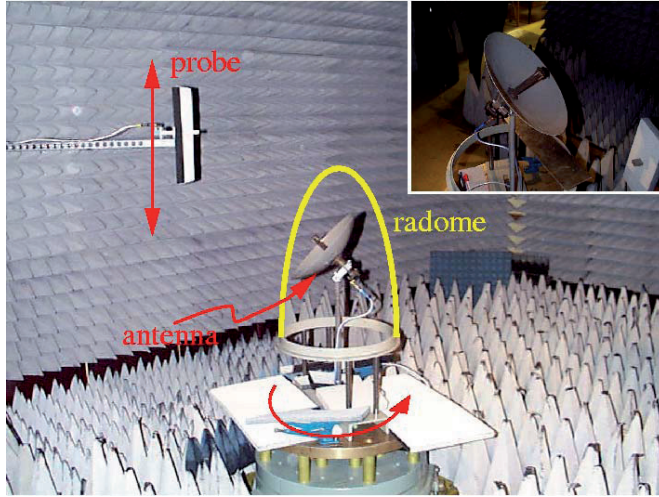
Figure 2:   Photo of the cylindrical near-field range at SAAB Bofors Dynamics, Sweden. The antenna under test is rotated and the probe is moved in the vertical direction. A close up of the reflector antenna is shown in the upper right corner.

corresponds to $29 - 43$ wavelengths in the frequency interval $8.0 - 12.0 \, \text{GHz}$.

   As a start, synthetic data is used to verify the method. Verification is also performed by a comparison between the measured far field and the far field calculated from the equivalent currents on the radome. The calculated far field agrees well with the measured far field. Moreover, when the radome is introduced, the field is scattered and flash lobes arise. The equivalent currents on the radome, due to these effects are identified and the flash lobes are accurately detected.

   Manufacturing errors, not localized in the measured near-field data, can be focused and detected in the equivalent currents on the radome surface. In this paper, it is shown that the field scattered by copper plates attached on the radome, is focused back towards the original position of the copper plates. The length of the side of the square copper plates is $6 \, \text{cm}$, $i.e.$, $1.6 - 2.4$ wavelengths corresponding to the frequency span $8.0 - 12.0 \, \text{GHz}$.

1.5   Outline

In Section 2, the experimental set-up is described and the measured near-field data is presented. The scalar surface integral representation is introduced and adapted to the specific problem in Section 3. Section 4 contains the implementation process of the scalar surface integral representation. Results, using synthetic near-field data, and the error of the method are presented. The results, when using the experimental near-field data, are shown and examined in Section 5. To give the reader a understanding of the information that can be extracted from the resulting data, Section 6 gives examples of ways to visualize the results. The paper ends with the achieved
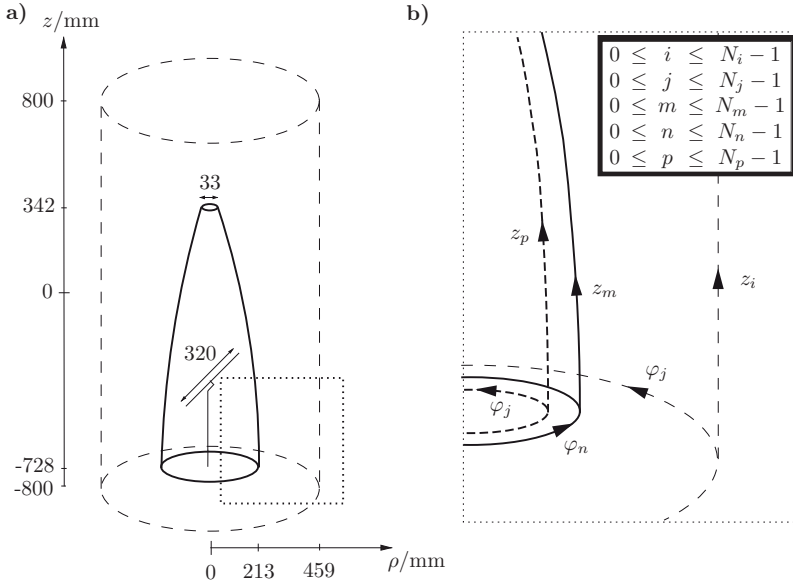
Figure 3:   (a) The dimensions of the reflector antenna, the radome, and the cylinder where the electric near field is measured. (b) A close-up showing the inner fictitious surface and the discretized geometric variables.

conclusions in Section 7.

2   Near-field measurements

The near-field data, used in this paper, was supplied by SAAB Bofors Dynamics and Applied Composites AB, Sweden. The set-up with relevant dimensions indicated is shown in Figures 2 and 3a. Three different measurements were performed; data measured without the radome, data measured with the radome, and data measured with the defect radome. The defect radome has two copper plates attached to its surface.

A reflector antenna, fed by a symmetrically located wave-guide, generates the near-field, see Figure 2. The diameter of the antenna is $0.32\,\mathrm{m}$ and its focal distance is $0.1\,\mathrm{m}$. The main lobe of the antenna is vertically polarized relative to the horizontal plane. The standing wave ratio (SWR) is approximately 1.4 in the frequency range $8.2 - 9.5\,\mathrm{GHz}$. The antenna is poorly adapted for other frequencies. A $10\,\mathrm{dB}$ reflection attenuator is connected to the antenna.

The height of the radome surface is modeled by

$$\rho(z) = \begin{cases} 0.213\,\text{m} & -0.728\,\text{m} \le z \le -0.663\,\text{m} \\ -(bz' + d) + \sqrt{(bz' + d)^2 - a(z')^2 - 2cz' - e} & -0.663\,\text{m} < z \le 0.342\,\text{m} \end{cases}$$
$$(2.1)$$

where $z' = z + 0.728\,\text{m}$ and the constants are $a = 0.122$, $b = 0.048$, $c = -0.018\,\text{m}$, $d = 0.148\,\text{m}$, and $e = -0.108\,\text{m}^2$, respectively. The material of the radome has a relative permittivity of 4.32 and its loss tangent is 0.0144. The thickness of the wall of the radome varies between $7.6 - 8.2\,\text{mm}$. The near-field measurement probe consists of a wave-guide for which no compensation is made in the final data. The cylindrical surface, where the electric field is measured, is located in the near-field zone [2].

The amplitude and phase of the electric field are measured in the frequency interval $8.0 - 12.0\,\text{GHz}$ on a cylindrical surface by moving the probe in the z-direction and rotating the antenna under test, see Figure 2. With this measurement set-up, the fields on the top and the bottom of the cylindrical surface could not be collected. It would have been preferable to measure the fields on an infinite cylinder. However, the size of the cylinder is chosen such that the turntable below the radome does not have a major influence of the measurements and such that the fields above $z = 800\,\text{mm}$ are negligible, $cf.$, Figures 1 and 3a. In the azimuth angle, 120 points are measured between $-180°$ and $180°$ in steps of $3°$. The z-dimension is divided into 129 points, separated by $12.5\,\text{mm}$. This means that at $8.0\,\text{GHz}$ the electric field is measured 3 times per wavelength, in the z-direction, and 1.5 times per wavelength, in the azimuth direction, respectively. Together, a total of $120 \times 129 = 15480$ measurement points are used for each radome configuration and frequency. The co- and cross-polarized measured electric fields are shown in Figure 1. The differences between the three different antenna and radome cases arise from constructive and destructive interference between the radiated field and the scattered field. In Figure 1 it is also observed that the electric field consists of a dominating co-component in the main lobe, $i.e.$, a dominating z-component since the antenna is vertically polarized.

3 The surface integral representation

The surface integral representation expresses the electromagnetic field in a homogeneous, isotropic region in terms of its values on the bounding surface. The representation states that if the electromagnetic field on a surface of a volume is known, the electromagnetic field in the volume can be determined [8, 16]. The representation is derived starting from the time harmonic Maxwell equations with the time convention $e^{i\omega t}$. The Maxwell equations transform into the vector Helmholtz equation

$$\nabla^2 \boldsymbol{E}(\boldsymbol{r}) + k^2 \boldsymbol{E}(\boldsymbol{r}) = 0 \tag{3.1}$$

since the material (air) is source free, homogeneous, and isotropic.

Assume that the electric field only consists of a component in the z-direction. This is a good approximation dealing with the specific measurements described in Section 2 since our prime interest is to reconstruct the electric field in the main lobe, where the z-component is clearly the dominating one, *cf.*, Figure 1.

Working with a scalar field, the surface integral representation only depends on the scalar electric field, E_z, and its normal derivative, $\partial E_z/\partial n$, *i.e.*, not all components of the electric and magnetic fields need to be included. Observe that in the vector integral representation all tangential components of the electric and magnetic fields must be taken into account [8]. The scalar surface integral representation is derived using the free space Green function $g(\boldsymbol{r}, \boldsymbol{r}') = \mathrm{e}^{-\mathrm{i}k|\boldsymbol{r}-\boldsymbol{r}'|}/4\pi|\boldsymbol{r}-\boldsymbol{r}'|$ giving [16]

$$\iint\limits_{S} \left[\frac{\partial g(\boldsymbol{r}, \boldsymbol{r}')}{\partial n} E_z(\boldsymbol{r}) - g(\boldsymbol{r}, \boldsymbol{r}') \frac{\partial E_z(\boldsymbol{r})}{\partial n} \right] \mathrm{d}S = \begin{cases} -E_z(\boldsymbol{r}') & \boldsymbol{r}' \in V \\ 0 & \boldsymbol{r}' \notin V \end{cases} \tag{3.2}$$

where V is the volume exterior to the closed surface S which consists of the radome surface with an added top and bottom surface. Observe that the electric field does not have to be zero outside the volume, *i.e.*, inside the radome. The surface integral representation (3.2) only states that the left-hand side of the equation, evaluated at a point $\boldsymbol{r}'$ outside the volume V, is zero, *i.e.*, the extinction theorem [16].

The equivalent surface currents are introduced as

$$M(\boldsymbol{r}) \equiv E_z(\boldsymbol{r}) \quad \text{and} \quad M'(\boldsymbol{r}) \equiv \frac{\partial E_z(\boldsymbol{r})}{\partial n} \tag{3.3}$$

which inserted in (3.2) give

$$\iint\limits_{\text{radome}} \left[\frac{\partial g(\boldsymbol{r}, \boldsymbol{r}')}{\partial n} M(\boldsymbol{r}) - g(\boldsymbol{r}, \boldsymbol{r}') M'(\boldsymbol{r}) \right] \mathrm{d}S = \begin{cases} -E_z^{\text{cyl}}(\boldsymbol{r}') & \boldsymbol{r}' \in \text{cylinder} \\ 0 & \boldsymbol{r}' \in \text{inside radome} \end{cases} \tag{3.4}$$

where E_z^{cyl} is the z-component of the electric field on the measurement cylinder. The fictitious surface, inside the radome, is shaped as the radome and located close to the radome wall.

3.1   Angular Fourier transformation

Due to the measurement set-up, the transformation, the Green's function, is axially symmetric, see Section 2. The symmetry only applies to the transformation, not to the electric field. Thus, the left-hand side in (3.4) represents a convolution and by using a Fourier transformation of the azimuth coordinate, the computational complexity can be brought down one dimension. This reduction of one dimension, can be understood by writing the left-hand side in (3.4) as a matrix, X. This matrix is a circulant matrix, *i.e.*, every row is shifted one step to the right compared to the previous row. The eigenvectors of all circulant matrices are the column vectors of the Fourier matrix, F. Multiplying a circulant matrix with the Fourier matrix, *i.e.*, performing the Fourier transformation, gives $FX = F\Lambda$ where Λ is a diagonal matrix, which can be seen as a reduction of one dimension [15].

The continuous variables in (3.4) are discretized to give linear matrix equations. The discretized cylindrical coordinate system is described by the integer indices depicted in Figure 3b. Discretization and Fourier transformation, in the azimuth coordinate, of (3.4) give

$$\sum_{m=0}^{N_m-1} \left[\widehat{\mathcal{G}}'_{im\hat{j}} \widehat{M}_{m\hat{j}} - \widehat{\mathcal{G}}_{im\hat{j}} \widehat{M}'_{m\hat{j}} \right] = -\widehat{E}^{\text{cyl}}_{i\hat{j}} \qquad \text{for all } i, \hat{j} \qquad (3.5)$$

and

$$\sum_{m=0}^{N_m-1} \left[\widehat{\mathsf{G}}'_{pm\hat{j}} \widehat{M}_{m\hat{j}} - \widehat{\mathsf{G}}_{pm\hat{j}} \widehat{M}'_{m\hat{j}} \right] = 0 \qquad \text{for all } p, \hat{j} \qquad (3.6)$$

where $\mathcal{G}$ and G are the surface integrals, taken over the radome, of the Green's function multiplied with the basis functions used in the discretization process. $\mathcal{G}$ has the discretized space variable $\boldsymbol{r}'$ belonging to the measurement cylinder and G has the discretized space variable $\boldsymbol{r}'$ belonging to the fictitious surface inside the radome, respectively. The prime denotes the normal derivative of the Green's function, $\hat{j}$ is the integer index belonging to the Fourier transformed azimuth component, and the "hat" denotes the Fourier transformed variables. The summation limits N_m and N_p are given in Figure 3b.

To solve the scalar surface integral representation, a limit process of (3.6) should be performed, letting the fictitious surface inside the radome approach the radome surface [2, 9]. To avoid singularities, we let the fictitious surface be located at a finite distance from the radome surface. This provides us with a simple and feasible method to allocate the surface currents, *i.e.*, the extinction theorem is used as an approximate solution to the integral representation in (3.6).

Reduction of M' in (3.5) and (3.6) gives

$$\sum_{m=0}^{N_m-1} \left\{ \widehat{\mathcal{G}}'_{im\hat{j}} - \sum_{p=0}^{N_p-1} \sum_{q=0}^{N_m-1} \widehat{\mathcal{G}}_{iq\hat{j}} \left(\widehat{\mathsf{G}}^{-1} \right)_{qp\hat{j}} \widehat{\mathsf{G}}'_{pm\hat{j}} \right\} \widehat{M}_{m\hat{j}} = -\widehat{E}^{\text{cyl}}_{i\hat{j}} \quad \text{for all } i, \hat{j} \qquad (3.7)$$

Equation (3.7) can also be written as $\hat{j}$ matrix equations

$$\widehat{\boldsymbol{G}}^{\text{radome}}_{\hat{j}} \widehat{\boldsymbol{M}}_{\hat{j}} = -\widehat{\boldsymbol{E}}^{\text{cyl}}_{\hat{j}} \qquad \text{for all } \hat{j} \qquad (3.8)$$

where the matrices are defined as $\widehat{\boldsymbol{M}}_{\hat{j}} \equiv [\widehat{M}_{m1}]_{\hat{j}}$, $\widehat{\boldsymbol{E}}^{\text{cyl}}_{\hat{j}} \equiv [\widehat{E}^{\text{cyl}}_{i1}]_{\hat{j}}$, and

$$\widehat{\boldsymbol{G}}^{\text{radome}}_{\hat{j}} \equiv [\widehat{\mathcal{G}}'_{im}]_{\hat{j}} - [\widehat{\mathcal{G}}_{im}]_{\hat{j}} [\widehat{\mathsf{G}}_{mp}]^{-1}_{\hat{j}} [\widehat{\mathsf{G}}'_{pm}]_{\hat{j}} \qquad \text{for all } \hat{j} \qquad (3.9)$$

The used notation of matrices is that of [1].

3.2   Inversion with singular value decomposition

Since the matrices $\widehat{\boldsymbol{G}}^{\text{radome}}_{\hat{j}}$ and $[\widehat{\mathsf{G}}_{mp}]_{\hat{j}}$ in (3.8) and (3.9) are not quadratic, a regular inversion cannot be performed. A fast and easy way to solve this is to use the

singular value decomposition (SVD) [15]. This method is used on both matrices, but the SVD-equations are only given here for $\widehat{\boldsymbol{G}}_{\hat{\jmath}}^{\text{radome}}$. The matrix system (3.8) can then be rewritten as

$$\widehat{\boldsymbol{U}}_{\hat{\jmath}}\widehat{\boldsymbol{S}}_{\hat{\jmath}}\widehat{\boldsymbol{V}}_{\hat{\jmath}}^{\dagger}\widehat{\boldsymbol{M}}_{\hat{\jmath}} = -\widehat{\boldsymbol{E}}_{\hat{\jmath}}^{\text{cyl}} \qquad \text{for all } \hat{\jmath} \tag{3.10}$$

where $\widehat{\boldsymbol{V}}_{\hat{\jmath}}^{\dagger}$ denotes the Hermitian conjugate of $\widehat{\boldsymbol{V}}_{\hat{\jmath}}$. Both $\widehat{\boldsymbol{U}}_{\hat{\jmath}}$ and $\widehat{\boldsymbol{V}}_{\hat{\jmath}}$ are orthogonal matrices. $\widehat{\boldsymbol{S}}_{\hat{\jmath}}$ is a diagonal matrix consisting of the singular values to $\widehat{\boldsymbol{G}}_{\hat{\jmath}}^{\text{radome}}$ in decreasing order. The singular values of both $\widehat{\boldsymbol{G}}_{\hat{\jmath}}^{\text{radome}}$ and $[\widehat{\mathsf{G}}_{mp}]_{\hat{\jmath}}$ exhibit the tendency shown by the curves in Figure 4a.

A cut-off value, δ, normalized to the operator L_2-norm of $\widehat{\boldsymbol{G}}_{1}^{\text{radome}}$ is chosen. The operator L_2-norm of $\widehat{\boldsymbol{G}}_{1}^{\text{radome}}$ is equal to the largest singular value (σ_1) of the largest Fourier transformed azimuth component [9]. All singular values smaller than δ are ignored during the inversion of $\widehat{\boldsymbol{S}}_{\hat{\jmath}}$ and are afterwards set to zero. If this is not done the small singular values create an uncontrolled growth of non-radiation currents when inverted. The mathematical formulation then fails since very small electric field contributions become dominating. Performing the inversion of (3.10) gives

$$\widehat{\boldsymbol{M}}_{\hat{\jmath}} = -\widehat{\boldsymbol{V}}_{\hat{\jmath}}\widehat{\boldsymbol{S}}_{\hat{\jmath}}^{-1}\widehat{\boldsymbol{U}}_{\hat{\jmath}}^{\dagger}\widehat{\boldsymbol{E}}_{\hat{\jmath}}^{\text{cyl}} \qquad \text{for all } \hat{\jmath} \tag{3.11}$$

Before the system of equations is solved, it is necessary to convert it back from Fourier space by an inverse Fourier transformation

$$\boldsymbol{M}_{j} = \mathcal{F}^{-1}\left[-\widehat{\boldsymbol{V}}_{\hat{\jmath}}\widehat{\boldsymbol{S}}_{\hat{\jmath}}^{-1}\widehat{\boldsymbol{U}}_{\hat{\jmath}}^{\dagger}\widehat{\boldsymbol{E}}_{\hat{\jmath}}^{\text{cyl}}\right] \qquad \text{for all } j, \hat{\jmath} \tag{3.12}$$

where j, as above, denotes the integer index belonging to the discretized azimuth component, see Figure 3b.

4 Implementation

Some adjustments of the formulas are made in the implementation process. To facilitate the calculations, the radome surface is reshaped into a closed surface by adding a smooth top and bottom surface. These extra surfaces are useful since the measurements are performed under non-ideal conditions. The turntable, on which the antenna and radome are located, see Figure 2, reflects some of the radiation, which is taken care of by the added bottom surface. The top surface takes care of the electric field that is reflected on the inside of the radome and then radiated through the top hole. If these factors are not considered, unwanted edge effects occur since the electric field originating from the turntable and the top of the radome is forced to arise from the radome itself.

The measured electric near field is only measured 1.5 times per wavelength, in the azimuth direction, at the frequency 8.0 GHz, see Section 2. To be sure that the
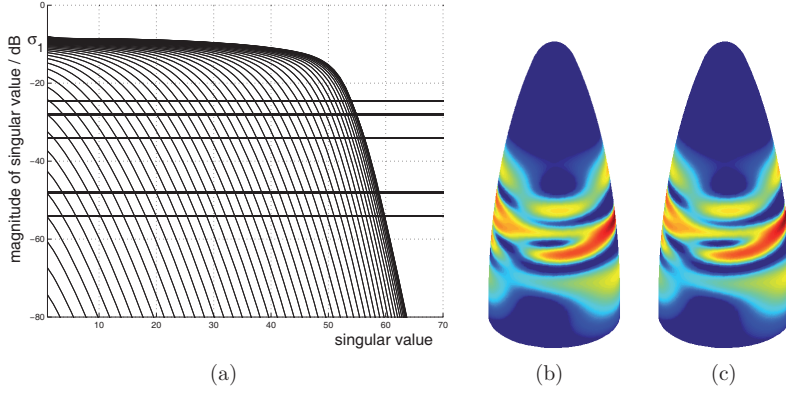
Figure 4: (a) The typical behavior of singular values of $\widehat{\boldsymbol{G}}_{\hat{\jmath}}^{\text{radome}}$ and $[\widehat{\mathsf{G}}_{mp}]_{\hat{\jmath}}$. Every curve represents the singular values of a Fourier transformed azimuth component, *i.e.*, different $\hat{\jmath}$. The horizontal lines describe the cut-off values, $\delta = \sigma_1[0.15\ 0.1\ 0.05\ 0.01\ 0.005]$. (b) The synthetic equivalent currents, originating from three dipoles, in a dB-scale $[-15, 0]$, normalized to the highest current value, *i.e.*, the maximum current magnitude in subfigure c. (c) The reconstructed currents in dB-scale $[-15, 0]$, normalized to its highest current value.

equivalent currents on the radome are recreated in an accurate way, it is necessary to have a high sample density on the radome. This is achieved by increasing the number of discrete points, in the azimuth direction, on the radome surface by including extra angles between the already existing ones. Thus, the axial symmetry of the Green's transformation is preserved.

The sample density on the measurement cylinder contributes very little to the total error. The scalar surface integral representation creates currents on the radome such that the electric field is correct at the measurement points. However, if the Nyquist theorem is fulfilled, then the electric field is correct at all points on the measurement surface, *i.e.*, not only at the measurement points [15]. As mentioned above, the amount of data is large and the matrix $\widehat{\boldsymbol{G}}^{\text{radome}}$, *cf.*, (3.9), has approximately 10^8 elements at the frequency $8.0\,\text{GHz}$ when the sample density is 10 points per wavelength both in the azimuth direction and in the z-direction on the radome.

To verify and find the error of the method, synthetic data is used. A synthetic electric field, originating from three dipoles inside the radome is shown in Figure 4b. The corresponding reconstructed currents on a surface shaped as the radome are shown in Figure 4c where the sample density is 10 points per wavelength both in the z-direction and in the azimuth direction. The inner fictitious surface is located one wavelength from the radome surface.

The error as a function of the Fourier transformed azimuth angle component is
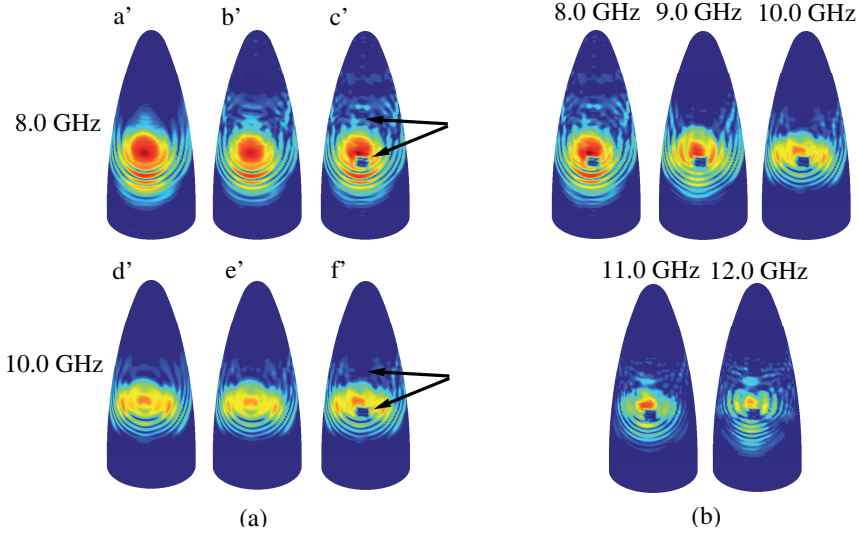
Figure 5: The reconstructed currents in dB-scale $[-30, 0]$, all normalized to the highest current value, *i.e.*, the maximum current magnitude in figure ac'. (a) The different measurement configurations are depicted at two different frequencies. From left to right; antenna without radome, antenna together with radome, and antenna together with defect radome, respectively. The arrows point out the location of the copper plates on the defect radome. (b) The defect radome case, shown at different frequencies.

defined as

$$
\begin{aligned}
\mathrm{Err}(\hat{j}) &= 20 \log_{10} \frac{\| \ \widehat{\boldsymbol{M}}_{\hat{j}} - \widehat{\boldsymbol{M}}_{\hat{j}}^{\mathrm{correct}} \ \|_2}{\| \ \widehat{\boldsymbol{M}}_{\hat{j}}^{\mathrm{correct}} \ \|_2} \\
&= 20 \log_{10} \frac{\sqrt{\sum_{m=0}^{N_m-1} \ | \ \widehat{M}_{m\hat{j}} - \widehat{M}_{m\hat{j}}^{\mathrm{correct}} \ |^2 \ \Delta S_m}}{\sqrt{\sum_{m=0}^{N_m-1} \ | \ \widehat{M}_{m\hat{j}}^{\mathrm{correct}} \ |^2 \ \Delta S_m}} \quad \text{for all } \hat{j}
\end{aligned}
\tag{4.1}
$$

where ΔS_m denotes the discretized area elements on the radome.

By using synthetic data and choosing appropriate cut-off values, δ, the error is shown to be below -60 dB for each existing Fourier transformed azimuth angle component. To obtain these low error levels, the measurement surface must be closed, *i.e.*, field values at the top and bottom surfaces of the cylindrical measurement surface must be included. The cut-off values depend on the complexity of the specific measurement set-up and must be investigated for each new set-up.

The total error of the scalar surface integral representation using the measured near field described in Section 2 is hard to define since the noise level and the amount

Figure 6:   Cross section of the reconstructed currents, on the radome surface, for the different measurement configurations at 8.0 GHz. The currents are shown as functions of the radome height for a fixed angle. All graphs are normalized to the highest current value, *i.e.*, the maximum current for the defect radome case. (a) The graph representing the currents in the main lobe, *i.e.*, the front of the radome. The positions of the copper plates are marked by thick lines on the horizontal axis. (b) The currents on the back of the radome.

of field spread outside the measurement cylinder are unknown parameters. Instead, we rely on the fact that the method handles synthetic data well and that the results using measured data is satisfactory, see Section 5.

5   Results using measured near-field data

The measured near-field data, described in Section 2, is investigated. The inner fictitious surface is located one wavelength from the radome surface. The sample density on the radome is 10 points per wavelength both in the azimuth direction and in the *z*-direction. The cut-off values are determined in accordance with the discussion in Section 4.

Three different measurement configurations are investigated, *viz.*, antenna, antenna together with radome, and antenna together with defect radome. The studied frequency interval is $8.0 - 12.0$ GHz. The results for the different measurement configurations are shown in Figure 5a at the frequencies 8.0 GHz and 10.0 GHz. In Figure 5b the results for the defect radome case are shown for the frequencies 8.0 GHz, 9.0 GHz, 10.0 GHz, 11.0 GHz, and 12.0 GHz, respectively.

In the case when no radome is located around the antenna, the equivalent currents are calculated on a surface shaped as the radome, see Figure 5aa' and 5ad'. The figures show that the near field close to the antenna is complex and hard to predict, *i.e.*, the diffraction pattern must be taken into account. The diffraction is explained as environmental reflections and an off-centered antenna feed.

The case when the radome is present, see Figure 5ab' and 5ae', shows in com-

Figure 7:   The reconstructed phase of the currents on the front of the radome. (a) The different measurement configurations are depicted at two different frequencies. From left to right; antenna without radome, antenna together with radome, and antenna together with defect radome, respectively. (b) The defect radome case, shown at different frequencies.

parison to the case without radome that the radome interacts with the antenna and hence disturbs the radiated field. However, the currents in the main lobe are hardly affected by the radome, as seen in Figure 6a. The influence of the radome is clearly visible in the reconstructed currents on the back of the radome where flash lobes occur, see Figure 6b.

The defect radome has two copper plates attached to its surface. These are located in the forward direction of the main lobe of the antenna and centered at the heights 41.5 cm and 65.5 cm above the bottom of the radome. The length of the side of the squared copper plates is 6 cm, which corresponds to 1.6 wavelengths at 8.0 GHz and 2.4 wavelengths at 12.0 GHz, respectively. The locations of the copper plates are detected as shown in Figure 5ac' and 5af', where the lower plate appears clearly. The other plate is harder to discern since it is located in a region with low amplitudes. However, a cross section graph through the main lobe detects even this copper plate, see Figure 6a. Observe that the effects of the copper plates cannot be localized directly in the near-field data, compare Figure 6a to Figure 1a. The near-field data only shows that the field is disturbed, not the location of the disturbance. Nevertheless, by using the scalar surface integral representation, the effects of the plates are localized and focused. The defect radome also increases the backscattering as seen in Figure 6b. Due to the copper plates, the flash lobes are different compared to the case with the non-defect radome.

Until now only the amplitude of the reconstructed currents has been investigated. The phase of the currents is depicted in Figure 7. The vertical lines above the main lobe in Figure 7a' and 7d' are due to phase jumps and are caused by the low
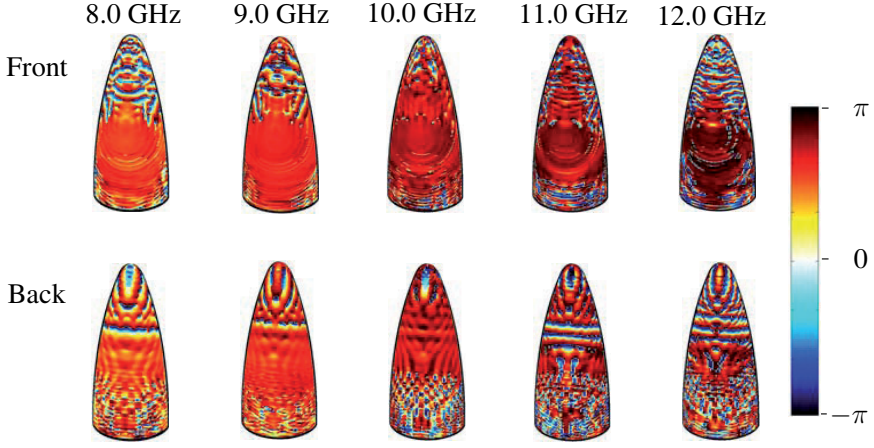
Figure 8:   The phase difference (antenna - antenna with radome) for several frequencies.

amplitude of the currents in these areas. The phase difference (antenna - antenna with radome) reveals how the the phase is changed due to the influence of the radome, see Figure 8. The phase shift, denoted Δ_φ, is only known modulus 2π. The phase shift in the main lobe is almost constant, especially for the low frequencies, which is more clearly seen by looking at the cross section of the front side of the radome, see Figure 9. What is noticeable in this image is the region between $z = -0.4\,\mathrm{m}$ and $z = 0\,\mathrm{m}$, *i.e.*, the main lobe where the phase shift is nearly constant. In areas where the amplitude of the field is small, *cf.*, Figure 6a, the phase of the field is not well defined, *i.e.*, it is dominated by noise. This almost constant phase shift, for the low frequencies, confirms that the radome is quite well adapted to the frequencies $8.0 - 9.0\,\mathrm{GHz}$, which is also the frequency interval where the antenna is well matched, see Section 2.

Sometimes, when dealing with phase information, the figures can be clarified by using phase unwrapping [4]. It means that the jump in the scale between 0 and 2π is removed. In our case phase unwrapping gives us no new information since the area of interest is the main lobe and the phase shift there is almost constant.

To validate the calculation of the phase shift, the propagation distance of the field through the radome, *i.e.*, the actual propagation path of the field in the radome material, is estimated and compared to the actual thickness of the radome given in Section 2. The propagation distance of the field through the radome is longer than the wall thickness since the field has an incident angle larger than zero. The phase difference between two fields propagating the distance d in air and in the radome material, respectively, can be written as [12]

$$\Delta_\varphi = \mathrm{Re}\left[2\pi f \sqrt{\epsilon_0 \epsilon_r \mu_0 (1 - \mathrm{i}\tan\delta)}\right] d - 2\pi f \sqrt{\epsilon_0 \mu_0}\, d \qquad (5.1)$$

where f is the frequency, d the propagation distance of the field, ϵ_0 the permittivity of
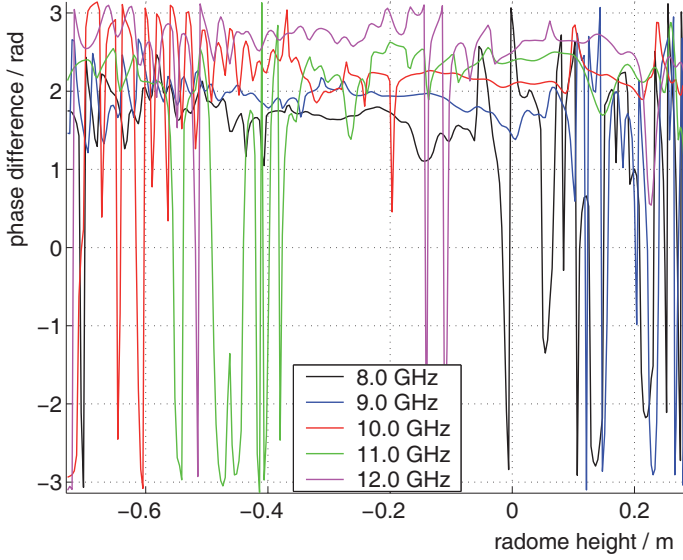
Figure 9:   Cross section of the phase difference (antenna - antenna with radome) on the front of the radome. Observe that in areas where the amplitude of the currents are small, *cf.*, Figure 6a, the phase of the field is not well defined, *i.e.*, it is dominated by noise.
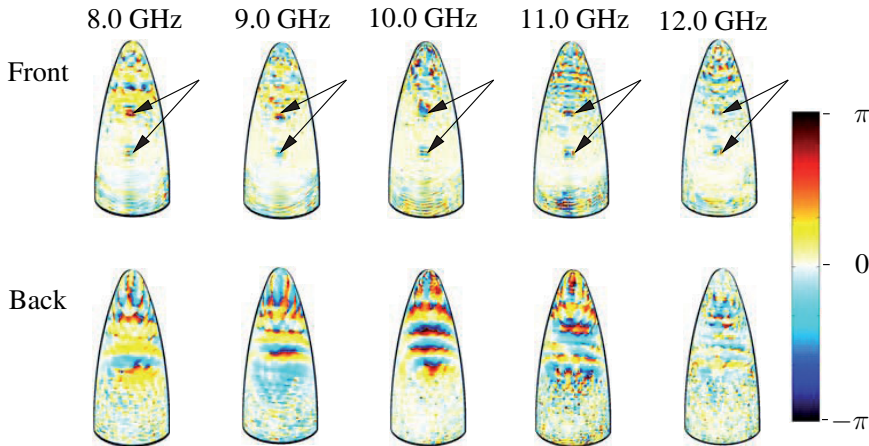
Figure 10:   The phase difference (antenna with radome - antenna with defect radome) for several frequencies. The arrows point out the location of the copper plates.

vacuum, and μ_0 the permeability of vacuum, respectively. The parameters belonging to the radome, described in Section 2, are the relative permittivity, ϵ_r, and the loss tangent, $\tan \delta$. Since only an estimation of the propagation distance is performed, we assume that this distance is the same in both air and the radome material. We assume perpendicular incidence and neglect all reflections. According to Section 2, the thickness of the radome is between $7.6 - 8.2 \, \text{mm}$. The almost constant phase shifts in the main lobe are approximated from Figure 9 for all frequencies. Solving for d in (5.1) results in a propagation distance of $9.3 - 9.7 \, \text{mm}$ for all frequencies, which is considered constant due to the crude approximations of the phase shifts. The phase shift, Δ_φ, is comparable to the insertion phase delay (IPD) often used in the radome industry.

The phase images in Figure 7b are not appropriate for finding the location of the copper plates. Instead, the phase difference (antenna with radome - antenna with defect radome) is useful, see Figure 10. These images reveal the change of the phase due to the attached copper plates on the defect radome.

As a final verification of the method, the amplitude on a sphere in the far-field region is studied. The electric field, originating from the equivalent currents on the radome, is calculated on the sphere, *i.e.*,

$$\boldsymbol{E}_j^{\text{sph}} = -\mathcal{F}^{-1}\left[\widehat{\boldsymbol{G}}_{\hat{j}}\widehat{\boldsymbol{M}}_{\hat{j}}\right] \qquad \text{for all } j, \hat{j} \tag{5.2}$$

in accordance with (3.8) and (3.12), except that $\widehat{\boldsymbol{G}}_{\hat{j}}$ now describes the transformation from the radome to the inner fictitious surface and to the far-field sphere. The denotions j and $\hat{j}$ are, as above, the integer index belonging to the discretized azimuth component and the Fourier transformed discretized azimuth component, respectively.

The far-field amplitude F is derived as

$$F(\theta, \phi) = kr\, \text{e}^{\text{i}kr} E^{\text{sph}}(r, \theta, \phi) \qquad \text{as } r \to \infty \tag{5.3}$$

where (r, θ, ϕ) denotes the spherical coordinate system [7]. The result is compared with far-field data, supplied by Applied Composites AB, as shown in Figure 11. The far field is depicted for the angles $\phi = 0$ and $\phi = \pi$, *i.e.*, a cross-section through the far field of the main lobe and the corresponding far field originating from the currents on the back of the radome. There is a lack of agreement between the measured far field and the calculated one at the angles corresponding to the top of the radome, *i.e.*, $\theta \approx 0$. This is due to the fact that fields originating hereof are not all included in the measured near-field data, since the measurement surface is a cylinder, see Figure 3a. The fact that the radome disturbs and reflects the electric field, as earlier seen in Figure 6b, can also be detected in the far field, see Figure 11d, where flash lobes appear when the radome is present.
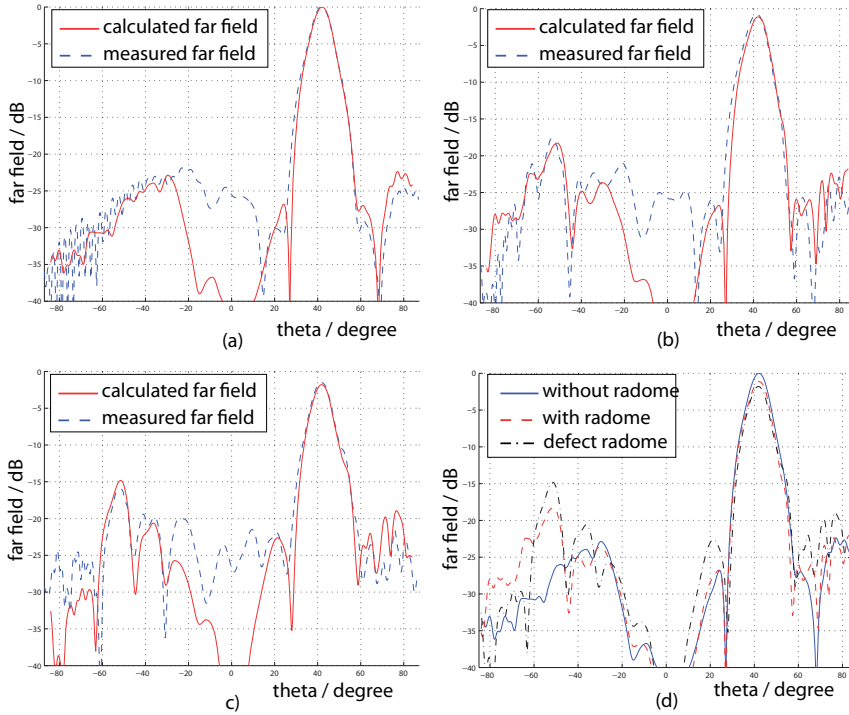
Figure 11: Comparison between the measured far-field data, supplied by Applied Composites AB, and the far field calculated from the equivalent currents on the radome surface. The far fields are normalized to the maximum value of the far field when no radome is present. (a) Antenna without radome. (b) Antenna together with radome. (c) Antenna together with defect radome. (d) The calculated far-field pattern for the three measurement configurations.

6   Alternative ways to visualize the electromagnetic currents

6.1   Amplitude of the reconstructed currents

In the previous section, the amplitude and the phase of the reconstructed currents have been visualized by showing the amplitude in dB-scale over the front side of the radome in Figure 5, and over a cross section of the front and the back in Figure 6. These ways of presenting the results are in this section supplemented in an attempt to see what possibilities other visualization approaches offer. First, the back side of the radome is shown in a dB-scale in Figure 12. The absolute value of the currents is also displayed in a linear scale on the front and the back of the radome in Figures 13
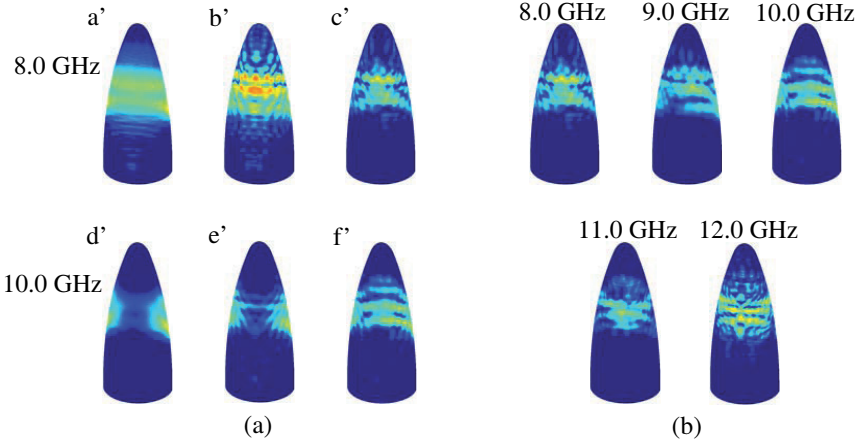
Figure 12: The reconstructed currents on the back of the radome in a dB-scale $[-30, 0]$, all normalized to the highest current value, *i.e.*, the maximum current magnitude in Figure 5ac'. (a) The different measurement configurations are depicted at two different frequencies. From left to right; antenna without radome, antenna together with radome, and antenna together with defect radome, respectively. (b) The defect radome case, shown at different frequencies.
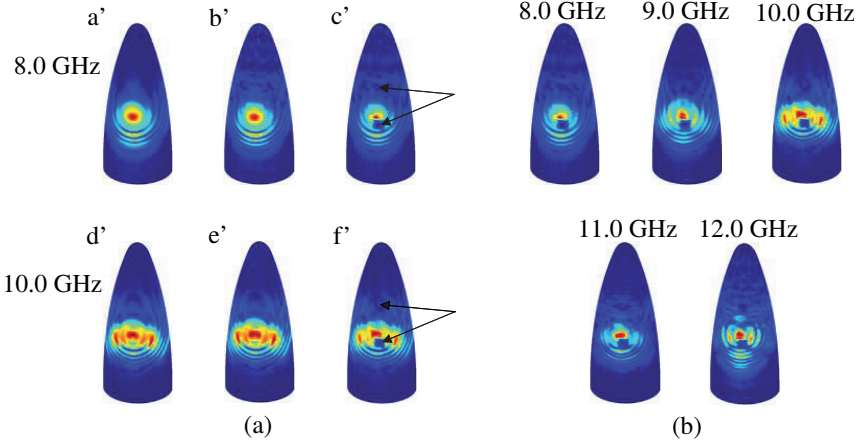
Figure 13: The reconstructed currents on the front of the radome in a linear scale, all normalized to the highest current value, *i.e.*, the maximum current magnitude in figure ac'. (a) The different measurement configurations are depicted at two different frequencies. From left to right; antenna without radome, antenna together with radome, and antenna together with defect radome, respectively. The arrows point out the location of the copper plates on the defect radome. (b) The defect radome case, shown at different frequencies.
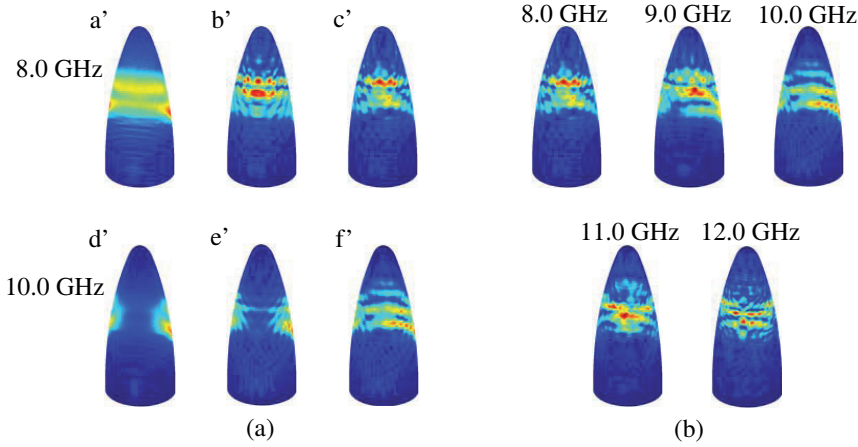
Figure 14:   The reconstructed currents on the back of the radome in a linear scale, all normalized to the highest current value, *i.e.*, the maximum current magnitude in Figure 13ac'. (a) The different measurement configurations are depicted at two different frequencies. From left to right; antenna without radome, antenna together with radome, and antenna together with defect radome, respectively. (b) The defect radome case, shown at different frequencies.

and 14, respectively. The flash lobes clearly appear in both dB- and linear scale, see Figures 12 and 14. Notice that the top copper plate is not resolved very well in the linear scale compared to the dB-scale in Figure 5.

6.2   Differences between the measurement configurations

To further demonstrate the distinctions between the three radome configurations their differences are calculated. The difference (|antenna| - |antenna with radome|) is shown in Figure 15 in a dB-scale, and in Figure 16 in a linear scale. The images show the influence of the radome and the appearance of flash lobes at the back of the radome. The dB-scale, Figure 15, has the advantage that also small current values are made visible. The advantage with the linear scale is that the sign of the difference is visible. In Figure 16, on the front of the radome, the field originating from the antenna is the strongest, *i.e.*, the difference is positive, while on the back of the radome, the field passing trough the radome as flash lobes is the strongest, *i.e.*, the difference is negative. This conclusion can not be drawn by looking at the dB-scale in Figure 15, where only the amplitude of the difference is displayed.

To emphasize the contribution of the defect radome, the difference (|antenna with radome| - |antenna with defect radome|) is studied in a dB-scale, see Figure 17 and in a linear scale, see Figure 18. The effect of the lower copper plate is clearly detectable in both figures, while the top plate is hard to discern in both scales, *i.e.*, these figures are useful to get an overview, but when it comes to details, other
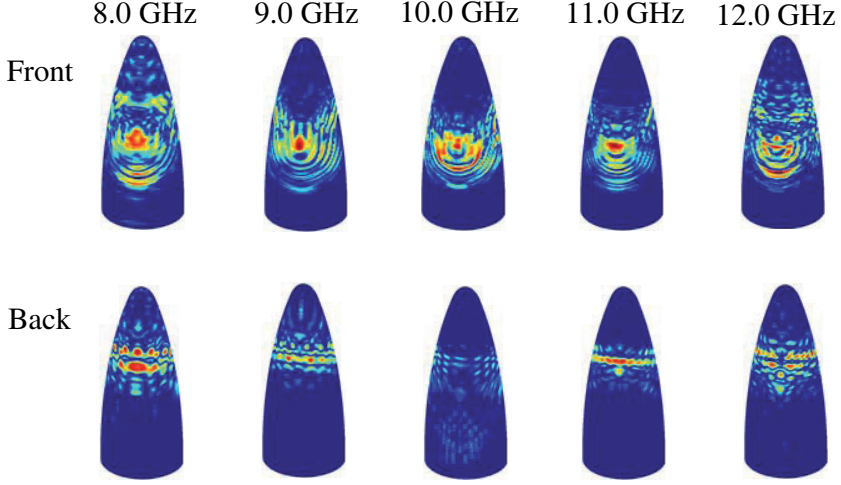
Figure 15: The amplitude difference abs(|antenna| - |antenna with radome|) for several frequencies. The amplitude differences are normalized to the highest value at each frequency and are all depicted in a dB-scale $[-20, 0]$.

visualizations approaches are needed. The tricky part with the dB-scale is to choose its lower limit. If a too low value is used, too much noise appears and blurs the image. However, if instead a too high value is picked, the field effects caused by the copper plates are hidden. To reveal the exact positions of the copper plates, cross section graphs through the front of the radome are presented in a linear and in a dB-scale in Figure 19 for the frequency 8.0 GHz. The effects of the copper plates are clearly seen in both scales, but their positions are somewhat off-centered. This is probably due to the fact that the copper plates cause diffractions and reflections, which do not occur when only the radome is present. There is also an uncertainty in the measurement set-up.

6.3 Propagation of the reconstructed fields

To see how the waves propagate on the radome-shaped surface, the field values, *i.e.*, $\mathrm{Re}\left(\boldsymbol{M}\,\mathrm{e}^{\mathrm{i}\omega t}\right)$ for $0 \leqslant \omega t \leqslant 2\pi$, are presented as a movie on `http://www.eit.lth.se/staff/kristin.persson` under the link `Research`. The distinctions between the different frequencies and radome configurations are revealed on both the front and the back side of the radome surface.
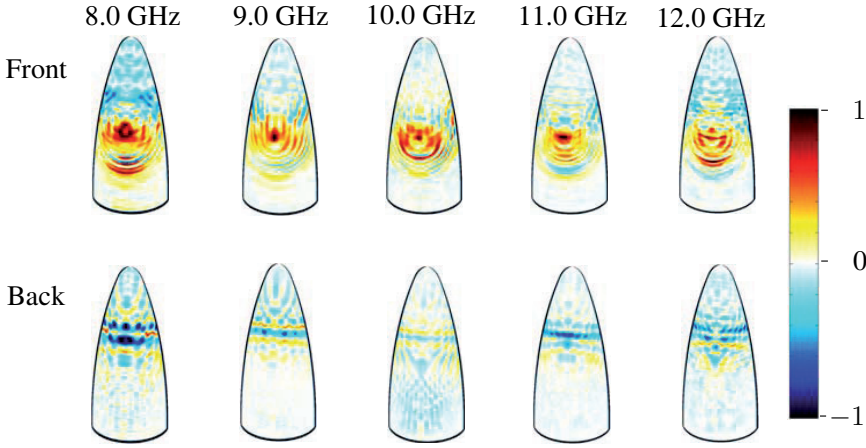
Figure 16: The amplitude difference (|antenna| - |antenna with radome|) for several frequencies. The amplitude differences are normalized to the highest value at each frequency and are all depicted in a linear scale.

7   Discussion and conclusions

The scalar surface integral representation gives a linear map between the equivalent currents and the near-field data for general geometries. It is shown that this map can be inverted for axially symmetric geometries. The model can theoretically be adapted to geometries lacking symmetry axes. Although it is not a feasible approach for radome applications, demanding large quantities of measured data, with the present computer capacity.

The transformation method is stable and useful in radome design and for evaluation purposes. To investigate the electric field passing through the radome, the current distribution on the antenna or on a surface enclosing the antenna must be known. Using the surface integral representation, the equivalent currents, on a surface enclosing the antenna, can be described. The insertion phase delay is estimated by investigating the phase of the reconstructed currents.

In this paper, copper plates are attached on the radome, in the direction of the antenna main lobe. The length of the side of the square copper plates is $1.6 - 2.4$ wavelengths, corresponding to the frequency span $8.0 - 12.0$ GHz. The effects of the plates cannot be localized directly by using the near-field data, but by using the equivalent currents, the effects are focused and detected on the radome surface. Thus, by transforming the near-field data to the radome surface, field defects introduced by the radome and other disturbances are focused back to their origins. Another range of application within the radome industry is to study how *e.g.*, lightning conductors and Pitot tubes, often placed on radomes, influence the equivalent currents. We predict that such influences and the field effects of the
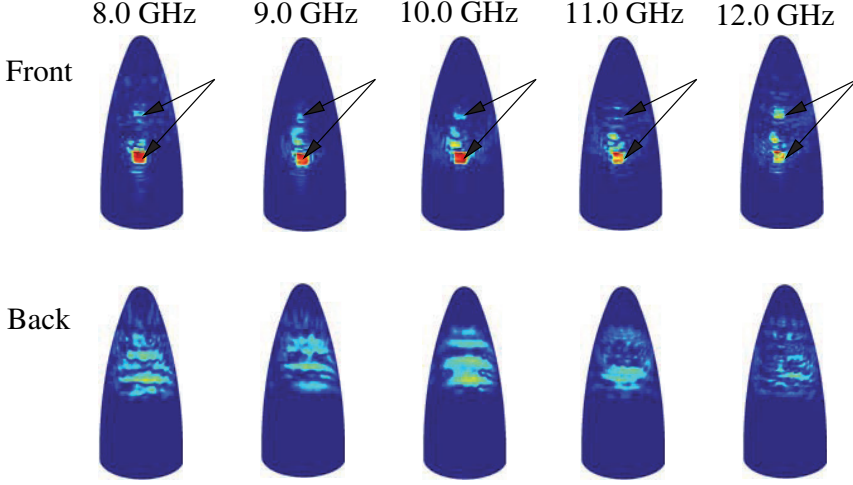
Figure 17: The amplitude difference abs(|antenna with radome| - |antenna with defect radome|) for several frequencies. The amplitude differences are normalized to the highest value at each frequency and are all depicted in a dB-scale $[-30, 0]$. The arrows point out the location of the copper plates.

radome itself can be detected.

It is concluded that the transformation method based on the scalar surface integral representation works very well and that the field of applications is large. A natural continuation is to elaborate the algorithm by including near-field data with cross-polarization, *i.e.*, to implement the full Maxwell equations with a Method of Moments (MoM). Nevertheless, if the measured near-field data consists of one dominating component, the use of the full Maxwell equations are not necessary, as shown in this paper.

Additional aspects to be investigated more thoroughly in the future are the resolution possibilities of manufacturing errors and other external field influences. Moreover, a study regarding the detection of different materials attached to the radome surface is desirable.

Acknowledgments
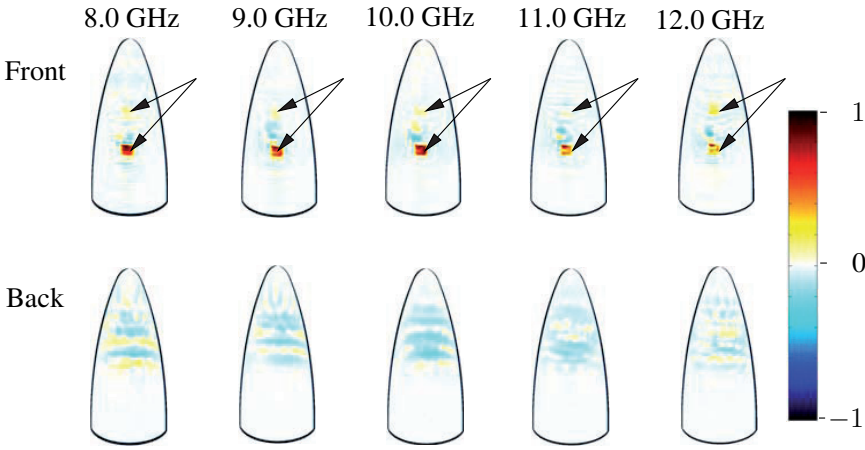
Figure 18: The amplitude difference (|antenna with radome| - |antenna with defect radome|) for several frequencies. The amplitude differences are normalized to the highest value at each frequency and are all depicted in a linear scale. The arrows point out the location of the copper plates.

References

[1] H. Anton. *Elementary Linear Algebra*. John Wiley & Sons, New York, 7 edition, 1994.

[2] C. A. Balanis. *Antenna Theory*. John Wiley & Sons, New York, second edition, 1997.

[3] L. E. Corey and E. B. Joy. On computation of electromagnetic fields on planar surfaces from fields specified on nearby surfaces. *IEEE Trans. Antennas Propagat.*, **29**(2), 402–404, 1981.

[4] D. C. Ghiglia and M. d. Pritt. *Two-Dimensional Phase Unwrapping: theory, algorithms, and software*. John Wiley & Sons, New York, 1998.

[5] J. Hanfling, G. Borgiotti, and L. Kaplan. The backward transform of the near field for reconstruction of aperture fields. *IEEE Antennas and Propagation Society International Symposium*, **17**, 764–767, 1979.

[6] J. E. Hansen, editor. *Spherical Near-Field Antenna Measurements*. Number 26 in IEE electromagnetic waves series. Peter Peregrinus Ltd., Stevenage, UK, 1988. ISBN: 0-86341-110-X.

[7] J. D. Jackson. *Classical Electrodynamics*. John Wiley & Sons, New York, second edition, 1975.
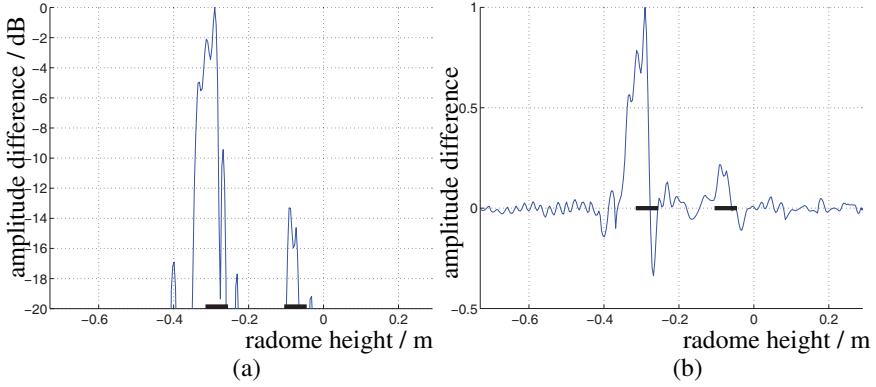
Figure 19:   Cross section of the amplitude difference (|antenna with radome| - |antenna with defect radome|) at 8.0 GHz. The graphs show the difference on the front of the radome as a function of the radome height for a fixed angle. They are both normalized to their highest values. The positions of the copper plates are marked by thick lines on the horizontal axis. (a) The difference abs(|antenna with radome| - |antenna with defect radome|) in dB-scale. (b) The difference (|antenna with radome| - |antenna with defect radome|) in a linear scale.

[8] D. S. Jones. *Acoustic and Electromagnetic Waves*. Oxford University Press, New York, 1986.

[9] R. Kress. *Linear Integral Equations*. Springer-Verlag, Berlin Heidelberg, second edition, 1999.

[10] J. Lee, E. M. Ferren, D. P. Woollen, and K. M. Lee. Near-field probe used as a diagnostic tool to locate defective elements in an array antenna. *IEEE Trans. Antennas Propagat.*, **36**(6), 884–889, 1988.

[11] K. Persson and M. Gustafsson. Reconstruction of equivalent currents using a near-field data transformation – with radome applications. *Progress in Electromagnetics Research*, **54**, 179–198, 2005.

[12] D. M. Pozar. *Microwave Engineering*. John Wiley & Sons, New York, 1998.

[13] Y. Rahmat-Samii, L. I. Williams, and R. G. Yaccarino. The UCLA bi-polar planar-near-field antenna-measurement and diagnostics range. *IEEE Antennas and Propagation Magazine*, **37**(6), 16–35, December 1995.

[14] T. K. Sarkar and A. Taaghol. Near-field to near/far-field transformation for arbitrary near-field geometry utilizing an equivalent electric current and MoM. *IEEE Trans. Antennas Propagat.*, **47**(3), 566–573, March 1999.

[15] G. Strang. *Introduction to applied mathematics*. Wellesley-Cambridge Press, Box 157, Wellesley MA 02181, 1986.

[16] S. Ström. Introduction to integral representations and integral equations for time-harmonic acoustic, electromagnetic and elastodynamic wave fields. In V. V. Varadan, A. Lakhtakia, and V. K. Varadan, editors, *Field Representations and Introduction to Scattering*, volume 1 of *Handbook on Acoustic, Electromagnetic and Elastic Wave Scattering*, chapter 2, pages 37–141. Elsevier Science Publishers, Amsterdam, 1991.

[17] V. V. Varadan, Y. Ma, V. K. Varadan, and A. Lakhtakia. Scattering of waves by spheres and cylinders. In V. V. Varadan, A. Lakhtakia, and V. K. Varadan, editors, *Field Representations and Introduction to Scattering*, volume 1 of *Handbook on Acoustic, Electromagnetic and Elastic Wave Scattering*, chapter 4, pages 211–324. Elsevier Science Publishers, Amsterdam, 1991.

[18] M. B. Woodworth and A. D. Yaghjian. Derivation, application and conjugate gradient solution of dual-surface integral equations for three-dimensional, multi-wavelength perfect conductors. *Progress in Electromagnetics Research*, **5**, 103–129, 1991.

[19] A. D. Yaghjian. An overview of near-field antenna measurements. *IEEE Trans. Antennas Propagat.*, **34**(1), 30–45, January 1986.

Reconstruction and visualization of equivalent currents on a radome surface using an integral representation formulation

Kristin Persson, Mats Gustafsson, and Gerhard Kristensson

Paper III

Abstract

In this paper an inverse source problem is investigated. The measurement set-up is a reflector antenna covered by a radome. Equivalent currents are reconstructed on a surface shaped as the radome in order to diagnose the radome's interaction with the radiated field. To tackle this inverse source problem an analysis of a full-wave integral representation, with the equivalent currents as unknowns, is used. The extinction theorem and its associated integral equation ensure that the reconstructed currents represent sources within the radome. The axially symmetric experimental set-up reduces the computational complexity of the problem. The resulting linear system is inverted by using a singular value decomposition. We visualize how the presence of the radome alters the components of the equivalent currents. The method enables us to determine the phase shift of the field due to the transmission of the radome, *i.e.*, the IPD (insertion phase delay). Also, disturbances due to defects, not observable in the measured near field, are localized in the equivalent currents. The results are also compared with earlier results where a scalar integral representation was employed.

1   Introduction

The aim of this paper is to calculate and visualize the sources of a measured electric field on a radome-shaped surface. The electric field is originating from an antenna inside the radome and is measured in the near-field zone outside the radome. The electrical size of the radome is 29 wavelengths at the frequency 8.0 GHz.

This kind of calculations are important in diagnosing antennas, designing radomes, *etc.*, since the field close to the body of interest is difficult to measure directly. By doing so, the interaction between the source and the measurement probe can give incorrect results [14, 36, 49]. In the process of designing a radome, the electric field close to the antenna is requested as an input to software calculating the field propagation through the radome wall [2, 39]. To get reliable results, it is crucial that the representation of the field radiated from the antenna, *i.e.*, the input data, is well known. To determine the performance of the radome it is eligible to quantify *e.g.*, beam deflection, transmission efficiency, pattern distortion, and the electrical thickness of the radome wall, *i.e.*, the insertion phase delay (IPD). It is also of interest to see how the mounting device and *e.g.*, lightning conductors and Pitot tubes, often placed on radomes, interact with the electric field.

One of the first techniques developed to solve the inverse source problems of this kind employs the plane wave expansion [10, 25, 37]. The method works very well when the equivalent currents are reconstructed on a planar surface. One recent area of application is the determination of the specific absorption rate of mobile phones [12]. A modal expansion of the field can be utilized if the reconstruction surface is cylindrical or spherical [14, 26, 31]. This method has been used to calculate the insertion phase delay (IPD) and to detect defects on a spherical radome [13]. More general geometries, *e.g.*, needle shaped objects and flat disks, can be handled by expanding the field in spheroidal wave functions [44]. A combination of the plane

wave spectrum and the modal expansion has been utilized in [7, 8] and [50] where flat antenna structures are diagnosed and safety perimeter of base stations' antennas is investigated, respectively.

To be able to handle a wider class of geometries, diagnostic techniques based on integral representations, which are solved by a method of moment approach, are applied. The drawback is the computational complexity. If the object on which the currents are to be reconstructed is metallic, *i.e.*, a perfect electric conductor (PEC), either the electric or magnetic field integral equation (EFIE or MFIE) can be employed [47] or combinations thereof [34, 40]. The equivalence principle is conveniently used when analyzing flat antenna structures [23, 24, 38]. An integral representation together with *a priori* information of the object and iterative solvers is used by [22] and [11] to find the electric current on the walls of a PEC for diagnose of a pyramidal horn antenna and a monopole placed on the chassis of a car.

In this paper we propose a technique using the integral representations to relate the unknown equivalent currents to a known measured near field. In addition to the integral representation, we also use an integral equation, originating from the extinction theorem [9]. By using the extinction theorem together with the integral representation we secure that the sources of the reconstructed currents only exist inside the enclosing volume [46]. The equivalent currents can be reconstructed on a surface arbitrarily close to the antenna. No *a priori* information of the material of the object just inside the surface is utilized.

2 Prerequisites

In this section, we review the basic equations employed in this paper. We start with a general geometry, and specialize to a body of revolution in Section 2.2.

2.1 General case

The surface integral representation expresses the electromagnetic field in a homogeneous, isotropic region in terms of its values on the closed bounding surface. We engage the integral representations to a domain outside a closed, bounded surface S_{rad}. Carefully employing the Silver-Müller radiation conditions, the solution of the Maxwell equations satisfy the following integral representation [17, 29, 42, 46]

$$
\iint_{S_{\mathrm{rad}}} \left(-\mathrm{j}\omega\mu_0\mu \; g(\boldsymbol{r}_1, \boldsymbol{r}_2)\big[\hat{\boldsymbol{n}}(\boldsymbol{r}_1) \times \boldsymbol{H}(\boldsymbol{r}_1)\big] + \frac{\mathrm{j}}{\omega\epsilon_0\epsilon} \; \nabla_1 g(\boldsymbol{r}_1, \boldsymbol{r}_2)\big\{\nabla_{1S} \cdot \big[\hat{\boldsymbol{n}}(\boldsymbol{r}_1) \times \boldsymbol{H}(\boldsymbol{r}_1)\big]\big\} \right.
$$

$$
\left. - \nabla_1 g(\boldsymbol{r}_1, \boldsymbol{r}_2) \times \big[\hat{\boldsymbol{n}}(\boldsymbol{r}_1) \times \boldsymbol{E}(\boldsymbol{r}_1)\big] \right) \mathrm{d}S_1 = \begin{cases} \boldsymbol{E}(\boldsymbol{r}_2) & \boldsymbol{r}_2 \text{ outside } S_{\mathrm{rad}} \\ \boldsymbol{0} & \boldsymbol{r}_2 \text{ inside } S_{\mathrm{rad}} \end{cases}
$$

$$(2.1)$$

where the time convention used is $\mathrm{e}^{\mathrm{j}\omega t}$, and the surface divergence is denoted $\nabla_S \cdot$ [9]. The variable of integration is denoted $\boldsymbol{r}_1$ and the observation point $\boldsymbol{r}_2$, see Figure 1. The relative permittivity ϵ and the relative permeability μ may depend on the
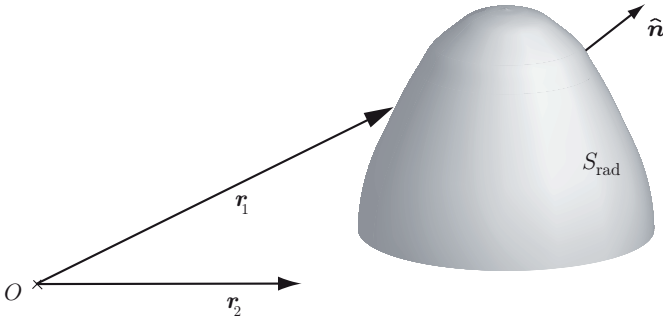
Figure 1: The surface S_{rad} of integration. The unit normal to the surface is $\hat{\boldsymbol{n}}$. The variable of integration is denoted $\boldsymbol{r}_1$ and the observation point $\boldsymbol{r}_2$.

angular frequency ω, *i.e.*, the material can be dispersive, but they are constants as a functions of space (homogeneous material). The scalar free space Green function is

$$g(\boldsymbol{r}_1, \boldsymbol{r}_2) = \frac{\mathrm{e}^{-\mathrm{j}k|\boldsymbol{r}_2 - \boldsymbol{r}_1|}}{4\pi|\boldsymbol{r}_2 - \boldsymbol{r}_1|} \tag{2.2}$$

where the wave number of the material is $k = \omega\sqrt{\epsilon_0\mu_0\epsilon\mu}$. The representation (2.1) states that if the electromagnetic field on S_{rad} is known, the electromagnetic field outside S_{rad} can be determined [15, 30, 46]. If these integrals are evaluated at a point $\boldsymbol{r}_2$ lying in the volume enclosed by S_{rad} these integrals cancel each other (extinction). It is important to notice that this does not necessarily mean that the field $\boldsymbol{E}$ is identically zero inside S_{rad}, it only states that the values of the integrals cancel.

The electric and magnetic equivalent surface current densities, $\boldsymbol{J}$ and $\boldsymbol{M}$, are introduced to simplify the notation and they are defined as [5]

$$\begin{cases} \boldsymbol{J}(\boldsymbol{r}) = \hat{\boldsymbol{n}}(\boldsymbol{r}) \times \boldsymbol{H}(\boldsymbol{r}) \\ \boldsymbol{M}(\boldsymbol{r}) = -\,\hat{\boldsymbol{n}}(\boldsymbol{r}) \times \boldsymbol{E}(\boldsymbol{r}) \end{cases} \tag{2.3}$$

The lower (or upper) representation in (2.1) is transformed into an integral equation letting $\boldsymbol{r}_2$ approach S_{rad}, *cf.*, Figure 1. However, care must be taken since the integrands become singular when $\boldsymbol{r}_2$ approaches the surface [9, 17, 28, 46]. The equation consists of three components, two describing the tangential field and one describing the normal component of the field. Since the normal component can be determined by the knowledge of the tangential parts, this representation has redundancies, *i.e.*, the normal component is eliminated [29].

To this end, (2.1) splits into a surface integral representation of the electric field

$$\iint\limits_{S_{\mathrm{rad}}} \left\{ -\mathrm{j}\omega\mu_0\mu \; g(\boldsymbol{r}_1,\boldsymbol{r}_2)\boldsymbol{J}(\boldsymbol{r}_1) + \mathrm{j}\frac{1}{\omega\epsilon_0\epsilon} \; \nabla_1 g(\boldsymbol{r}_1,\boldsymbol{r}_2)\big[\nabla_{1S} \cdot \boldsymbol{J}(\boldsymbol{r}_1)\big] \right. \tag{2.4}$$

$$\left. + \nabla_1 g(\boldsymbol{r}_1,\boldsymbol{r}_2) \times \boldsymbol{M}(\boldsymbol{r}_1) \right\} \mathrm{d}S_1 = \boldsymbol{E}(\boldsymbol{r}_2) \qquad \boldsymbol{r}_2 \text{ outside } S_{\mathrm{rad}}$$

and a surface integral equation in $\boldsymbol{J}$ and $\boldsymbol{M}$

$$\hat{\boldsymbol{n}}(\boldsymbol{r}_2) \times \iint\limits_{S_{\mathrm{rad}}} \left\{ \mathrm{j}\omega\mu_0\mu \; g(\boldsymbol{r}_1,\boldsymbol{r}_2)\boldsymbol{J}(\boldsymbol{r}_1) - \mathrm{j}\frac{1}{\omega\epsilon_0\epsilon} \; \nabla_1 g(\boldsymbol{r}_1,\boldsymbol{r}_2)\big[\nabla_{1S} \cdot \boldsymbol{J}(\boldsymbol{r}_1)\big] \right. \tag{2.5}$$

$$\left. - \nabla_1 g(\boldsymbol{r}_1,\boldsymbol{r}_2) \times \boldsymbol{M}(\boldsymbol{r}_1) \right\} \mathrm{d}S_1 = \frac{1}{2} \boldsymbol{M}(\boldsymbol{r}_2) \qquad \boldsymbol{r}_2 \in S_{\mathrm{rad}}$$

When necessary, the integrals in the surface integral equation are interpreted as Cauchy's principal value [9, 35].

The integral equation is written in a weak form, *i.e.*, it is multiplied by a test function and integrated over its domain [6, 20, 28, 34]. The representation (2.4) does not need this treatment since $\boldsymbol{r}_2$ consists of a discrete number of points outside S_{rad}, *i.e.*, $\boldsymbol{r}_1$ and $\boldsymbol{r}_2$ do not coincide. The weak formulation of (2.5) is derived in Appendix A, where the test function is denoted by $\boldsymbol{\Psi}$, giving

$$\mathrm{j}\omega\mu_0\mu \iint\limits_{S_{\mathrm{rad}}} \iint\limits_{S_{\mathrm{rad}}} \boldsymbol{\Psi}(\boldsymbol{r}_2) \cdot g(\boldsymbol{r}_1,\boldsymbol{r}_2)\boldsymbol{J}(\boldsymbol{r}_1) \; \mathrm{d}S_1 \; \mathrm{d}S_2$$

$$- \mathrm{j}\frac{1}{\omega\epsilon_0\epsilon} \iint\limits_{S_{\mathrm{rad}}} \iint\limits_{S_{\mathrm{rad}}} \big[\nabla_{2S} \cdot \boldsymbol{\Psi}(\boldsymbol{r}_2)\big] g(\boldsymbol{r}_1,\boldsymbol{r}_2)\big[\nabla_{1S} \cdot \boldsymbol{J}(\boldsymbol{r}_1)\big] \; \mathrm{d}S_1 \; \mathrm{d}S_2$$

$$- \iint\limits_{S_{\mathrm{rad}}} \iint\limits_{S_{\mathrm{rad}}} \boldsymbol{\Psi}(\boldsymbol{r}_2) \cdot \big[\nabla_1 g(\boldsymbol{r}_1,\boldsymbol{r}_2) \times \boldsymbol{M}(\boldsymbol{r}_1)\big] \; \mathrm{d}S_1 \; \mathrm{d}S_2$$

$$- \frac{1}{2} \iint\limits_{S_{\mathrm{rad}}} \big[\hat{\boldsymbol{n}}(\boldsymbol{r}_2) \times \boldsymbol{\Psi}(\boldsymbol{r}_2)\big] \cdot \boldsymbol{M}(\boldsymbol{r}_2) \; \mathrm{d}S_2 = 0 \quad (2.6)$$

2.2   Body of revolution

From now on the equations are adapted to a body of revolution (BOR) in vacuum, *i.e.*, $\epsilon = 1$ and $\mu = 1$. The surface is parameterized by the azimuth angle φ and the height coordinate along the surface v, *i.e.*, the position vector $\boldsymbol{r}$ can be expressed as $\boldsymbol{r}(\varphi,v) = \rho(v)\cos\varphi \, \hat{\boldsymbol{e}}_{\mathrm{x}} + \rho(v)\sin\varphi \, \hat{\boldsymbol{e}}_{\mathrm{y}} + z(v)\, \hat{\boldsymbol{e}}_{\mathrm{z}}$. The normalized basis vectors are then

$$\hat{\boldsymbol{\varphi}}(\varphi) = \frac{\partial \boldsymbol{r}}{\partial \varphi} \Big/ \left|\frac{\partial \boldsymbol{r}}{\partial \varphi}\right| = -\sin\varphi \, \hat{\boldsymbol{e}}_{\mathrm{x}} + \cos\varphi \, \hat{\boldsymbol{e}}_{\mathrm{y}} \qquad \text{and} \qquad \hat{\boldsymbol{v}}(\varphi,v) = \frac{\partial \boldsymbol{r}}{\partial v} \Big/ \left|\frac{\partial \boldsymbol{r}}{\partial v}\right|$$

and $\{\hat{\boldsymbol{n}}, \hat{\boldsymbol{\varphi}}, \hat{\boldsymbol{v}}\}$ forms a right-handed triple of unit vectors. The curvilinear components of the magnetic equivalent surface current and electric field are denoted as
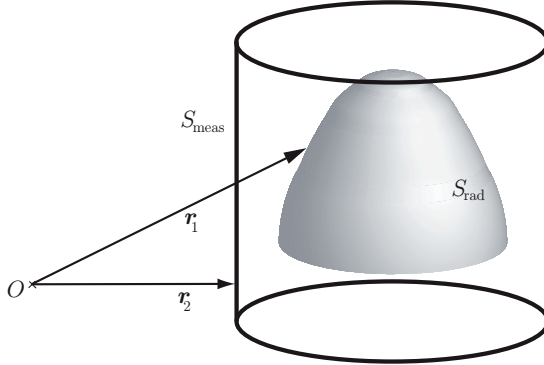
Figure 2: The regions of integration in (2.9).

$E^\varphi = -M^{\mathrm{v}}$ and $E^{\mathrm{v}} = M^\varphi$, cf., (2.3), where $M^\varphi = \boldsymbol{M} \cdot \hat{\boldsymbol{\varphi}}$, and $M^{\mathrm{v}} = \boldsymbol{M} \cdot \hat{\boldsymbol{v}}$. The magnetic field and the electric equivalent current are related in a similar way. The explicit expressions of the normalized basis vectors, surface divergence, the gradient of the Green function, and other useful formulas are derived in Appendix B.

Two functions, $\boldsymbol{a}^\varphi_{mj}$ and $\boldsymbol{a}^{\mathrm{v}}_{mj}$, are used as basis functions. They are defined as

$$\boldsymbol{a}^\varphi_{mj} = f^\varphi_j(v)\,\mathrm{e}^{\mathrm{j}m\varphi}\hat{\boldsymbol{\varphi}}$$
$$\boldsymbol{a}^{\mathrm{v}}_{mj} = f^{\mathrm{v}}_j(v)\,\mathrm{e}^{\mathrm{j}m\varphi}\hat{\boldsymbol{v}} \tag{2.7}$$

The height of the radome, v_1, is discretized into points, v_j, where $j = 1, \ldots, N_{\mathrm{z}}$. The functions $f^{\varphi/\mathrm{v}}_j(v)$ can be chosen as a constant, linear, cubic, spline functions etc., with support in a neighborhood of v_j [6, 34]. For the results in this paper, both $f^{\varphi/\mathrm{v}}_j(v)$ are chosen as piecewise linear functions, i.e., one-dimensional rooftops. Observe that φ/v in $f^{\varphi/\mathrm{v}}$ denotes a superscript and not an exponential. In the azimuthal direction, a global function, $\mathrm{e}^{\mathrm{j}m\varphi}$, i.e., a Fourier basis, is used due to the symmetry of the body, and m is an integer index. The current is expanded as

$$\boldsymbol{J} = \sum_{m,j} \left\{ J^\varphi_{mj}\,\boldsymbol{a}^\varphi_{mj} + J^{\mathrm{v}}_{mj}\,\boldsymbol{a}^{\mathrm{v}}_{mj} \right\} \tag{2.8}$$

The magnetic current $\boldsymbol{M}$ is expanded in a similar way, but with expansion coefficients $M^{\varphi/\mathrm{v}}_{mj}$.

Galerkin's method is used [6]. That is, the test functions are according to (2.7) $\boldsymbol{\Psi}^\varphi_{ni} = (\boldsymbol{a}^\varphi_{ni})^*$ and $\boldsymbol{\Psi}^{\mathrm{v}}_{ni} = (\boldsymbol{a}^{\mathrm{v}}_{ni})^*$ where complex conjugation is denoted by a star and the indicies run through the same integers as m and j. The surface divergence, the tangential components of the test function and the current are explicitly derived and listed in Appendix C.

The surface integral representation (2.4) is applied to the measurement set-up described in Section 3, i.e., $\boldsymbol{r}_2$ belongs to a cylindrical surface S_{meas}, see Figure 2. This surface has axial symmetry with constant radius and is parameterized by φ_2

and v_2, in the same manner as the surface S_{rad} is. The height is discretized into points, v_q, where $q = 1, \ldots, N_{\mathrm{z}}^{\mathrm{meas}}$. None of the integrals contains singularities since $\boldsymbol{r}_1$ and $\boldsymbol{r}_2$ will not coincide. From equation (2.4) we get

$$
\begin{bmatrix} \hat{\boldsymbol{v}} \\ \hat{\boldsymbol{\varphi}} \end{bmatrix} \cdot \left\{ -\mathrm{j}\omega\mu_0 \iint\limits_{S_{\mathrm{rad}}} g(\boldsymbol{r}_1, \boldsymbol{r}_2) \boldsymbol{J}(\boldsymbol{r}_1) \ \mathrm{d}S_1 + \mathrm{j}\frac{1}{\omega\epsilon_0} \iint\limits_{S_{\mathrm{rad}}} \nabla_1 g(\boldsymbol{r}_1, \boldsymbol{r}_2) \big[\nabla_{1S} \cdot \boldsymbol{J}(\boldsymbol{r}_1) \big] \ \mathrm{d}S_1 \right.
$$
$$
\left. + \iint\limits_{S_{\mathrm{rad}}} \nabla_1 g(\boldsymbol{r}_1, \boldsymbol{r}_2) \times \boldsymbol{M}(\boldsymbol{r}_1) \ \mathrm{d}S_1 \right\} = \begin{bmatrix} \hat{\boldsymbol{v}} \cdot \boldsymbol{E}(\boldsymbol{r}_2) \\ \hat{\boldsymbol{\varphi}} \cdot \boldsymbol{E}(\boldsymbol{r}_2) \end{bmatrix} = \begin{bmatrix} E^{\mathrm{v}}(\varphi_2, v_2) \\ E^{\varphi}(\varphi_2, v_2) \end{bmatrix} \qquad \boldsymbol{r}_2 \in S_{\mathrm{meas}}
$$
$$(2.9)$$

where the tangential components are projected using scalar multiplication.

Since the currents are expanded in the Fourier series, the right hand side of (2.9) is expanded in the same way, *i.e.*, the Fourier expansion of $E^{\varphi/\mathrm{v}}$ is

$$
E^{\varphi/\mathrm{v}}(\varphi_2, v_2) = \sum_{n=-\infty}^{\infty} E_n^{\varphi/\mathrm{v}}(v_2) \mathrm{e}^{\mathrm{j}n\varphi_2}
$$

where

$$
E_n^{\varphi/\mathrm{v}}(v_2) = \frac{1}{2\pi} \int_0^{2\pi} E^{\varphi/\mathrm{v}}(\varphi_2, v_2) \mathrm{e}^{-\mathrm{j}n\varphi_2} \ \mathrm{d}\varphi_2 \tag{2.10}
$$

and n is an integer index. Observe that φ/v in $E^{\varphi/\mathrm{v}}$ denotes a superscript and not an exponential. The Fourier series reduce the dimensions of the problem by one degree [27, 34, 45].

Equation (2.9) consists of nine different angular integrals. These integrals are non-singular and are derived and listed in Appendix D. Equation (2.9) is organized as a system of matrices, *i.e.*,

$$
\begin{bmatrix} [Z^{11}] & [Z^{12}] \\ [Z^{21}] & [Z^{22}] \end{bmatrix} \begin{bmatrix} [J^{\mathrm{v}}] \\ [J^{\varphi}] \end{bmatrix} + \begin{bmatrix} [X^{11}] & [X^{12}] \\ [X^{21}] & [X^{22}] \end{bmatrix} \begin{bmatrix} [M^{\mathrm{v}}] \\ [M^{\varphi}] \end{bmatrix} = \begin{bmatrix} [E^{\mathrm{v}}] \\ [E^{\varphi}] \end{bmatrix} \tag{2.11}
$$

where the right hand side consists of the Fourier coefficients of the electric field. The details of the derivation and the explicit expressions of the matrix elements $\big[Z^{kl} \big]$ and $\big[X^{kl} \big]$ are given in Appendix F.

The integral equation in (2.6) also contains nine different integrals in the angular direction. These are the same as in the integral representation, *i.e.*, (2.9), but they now contain singularities. The integrals are derived and listed in Appendix D. Equation (2.6) is also organized as a system of matrices, *i.e.*,

$$
\begin{bmatrix} [\mathcal{Z}^{11}] & [\mathcal{Z}^{12}] \\ [\mathcal{Z}^{21}] & [\mathcal{Z}^{22}] \end{bmatrix} \begin{bmatrix} [J^{\mathrm{v}}] \\ [J^{\varphi}] \end{bmatrix} + \begin{bmatrix} [\mathcal{X}^{11}] & [\mathcal{X}^{12}] \\ [\mathcal{X}^{21}] & [\mathcal{X}^{22}] \end{bmatrix} \begin{bmatrix} [M^{\mathrm{v}}] \\ [M^{\varphi}] \end{bmatrix} = \begin{bmatrix} [0] \\ [0] \end{bmatrix} \tag{2.12}
$$

The details of the derivation and the explicit expressions of the matrix elements $\big[\mathcal{Z}^{kl} \big]$ and $\big[\mathcal{X}^{kl} \big]$ are given in Appendix G.

Combining the matrix systems for the integral representation (2.11) and (2.12) gives, in short-hand notation,

$$
\begin{bmatrix} [Z] & [X] \\ [\mathcal{Z}] & [\mathcal{X}] \end{bmatrix} \begin{bmatrix} [J] \\ [M] \end{bmatrix} = \begin{bmatrix} [E] \\ [0] \end{bmatrix}
$$
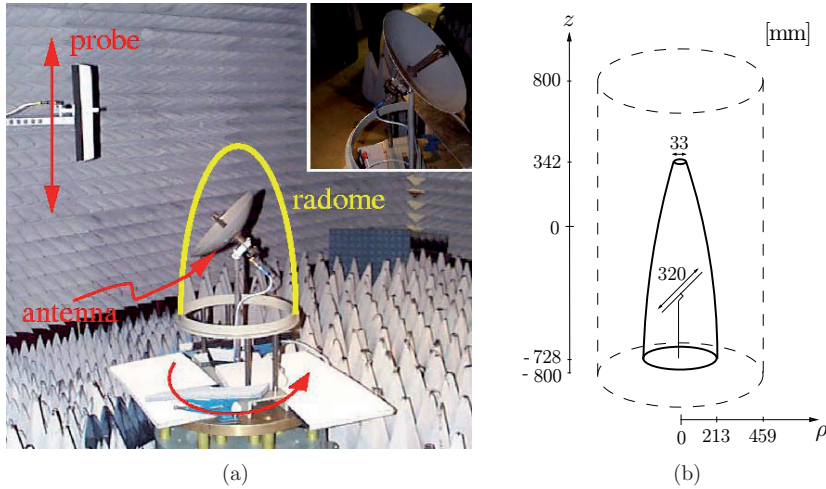
Figure 3: (a) Photo of the cylindrical near-field range at SAAB Bofors Dynamics, Sweden. The antenna under test is rotated and the probe is moved in the vertical direction. A close up of the reflector antenna is shown in the upper right corner. (b) The dimensions of the reflector antenna, the radome, and the cylinder where the electric near field is measured.

The magnitude of the entries of the matrices may differ by several orders of magnitude. To avoid numerical errors, the system is solved for one current at a time,

$$[J] = -[\mathcal{Z}]^{-1}[\mathcal{X}][M] \qquad\qquad \Longrightarrow$$
$$\left\{-[Z][\mathcal{Z}]^{-1}[\mathcal{X}] + [X]\right\}[M] = [E] \tag{2.13}$$

when $\boldsymbol{J}$ is eliminated. In the first line, $\boldsymbol{J}$ is expressed as a function of $\boldsymbol{M}$ utilizing the integral equation. The matrix $[\mathcal{Z}]$ is quadratic and inverted numerically in MATLAB. The second equation is ill-posed. The matrix is no longer quadratic and to solve for $\boldsymbol{M}$, the linear system is inverted and regularized by the singular value decomposition (SVD) in MATLAB [45]. Besides numerical errors also noise and measurement errors show up. Here, the SVD helps in suppressing the amplification of noise in the inversion [3]. In our initial investigation we have not encountered any problems with spurious modes [41] or by using the numerical inversion of MATLAB or the SVD. However, a more detailed investigation of the ill-posed equations is needed. Specifically, a discussion of how to chose the cut-off value, *i.e.*, the magnitude of the largest singular value that is excluded, needs to be addressed further.

3   Near-field measurements

The experimental set-up and the measured electric field is described in [32]. However, for convenience, the necessary information is summarized. The measurement

set-up is shown in Figure 3. A reflector antenna, fed by a symmetrically mounted wave-guide, generates the electromagnetic field. The diameter of the antenna is $0.32\,\text{m}$, and the main lobe of the antenna is vertically polarized relative to the horizontal plane. The radome surface is axially symmetric and its radius, in terms of the height coordinate, is modeled by

$$\rho(z) = \begin{cases} 0.213\,\text{m} & -0.728\,\text{m} \le z \le -0.663\,\text{m} \\ -(bz' + d) + \sqrt{(bz' + d)^2 - a(z')^2 - 2cz' - e} & -0.663\,\text{m} < z \le 0.342\,\text{m} \end{cases}$$

where $z' = z + 0.728\,\text{m}$ and the constants are $a = 0.122$, $b = 0.048$, $c = -0.018\,\text{m}$, $d = 0.148\,\text{m}$, and $e = -0.108\,\text{m}^2$, respectively. The height of the radome corresponds to 29 wavelengths for the frequency $8.0\,\text{GHz}$. The material of the radome has a relative permittivity of about 4.32 and its loss tangent is about 0.0144. The thickness of the wall of the radome varies over the surface in the interval $7.6 - 8.2\,\text{mm}$.

The surface S_{rad} in (2.6) and (2.9) is defined by the radome surface, closed with smooth top and bottom surfaces. These added surfaces are needed since the integral representation applies to a closed surface and the measurements are performed under non-ideal conditions. The turntable, on which the antenna and radome are located, see Figure 3a, reflects some of the radiation, which is taken care of by the added bottom surface. The top surface takes care of the electric field that is reflected on the inside of the radome and then radiated through the top hole. If these factors are neglected, unwanted edge effects occur, since the electric fields originating from the turntable and the top of the radome are forced to originate from the radome itself. The radome surface is divided into 8 cells per wavelength in the height direction, and in each cell 4 points are chosen where the integrations are evaluated.

The electric field is measured on a cylindrical surface by moving the probe in the z-direction and rotating the radome and the antenna under test, see Figure 3. This surface is located in the near-field zone [4]. The near-field measurement probe consists of a waveguide for which no compensation is made in the final data. With this measurement set-up, the data on the top and the bottom of the cylindrical surface cannot be collected. It would have been preferable to measure the fields on an infinite cylinder. However, the size of the cylinder is chosen such that the turntable below the radome does not have a major influence on the measurements and such that the fields above $z = 800\,\text{mm}$ are negligible. In the azimuth angle, 120 points are measured in steps of $3°$. The z-dimension is divided into 129 points, every two points, v_q and v_{q+1}, are separated by $12.5\,\text{mm}$.

Three different measurement configurations are considered; antenna without radome, antenna together with radome, and antenna together with defect radome. The defect radome has two copper plates attached to its surface. These are located in the forward direction where the main lobe hits the radome and centered at the heights $41.5\,\text{cm}$ and $65.5\,\text{cm}$ above the bottom of the radome. The side of the squared copper plates is $6\,\text{cm}$, corresponding to 1.6 wavelengths at $8.0\,\text{GHz}$.

The absolute values of the measured co- and cross-polarized electric fields, E^{v} and E^{φ}, respectively, are shown in Figures 4–5, where $|E^{\text{v}}|_{\text{dB}} = 20 \log\left(|E^{\text{v}}|/|E^{\text{v}}|_{\text{max}}\right)$ and $|E^{\varphi}|_{\text{dB}} = 20 \log\left(|E^{\varphi}|/|E^{\text{v}}|_{\text{max}}\right)$, respectively. That is, all fields are normalized with
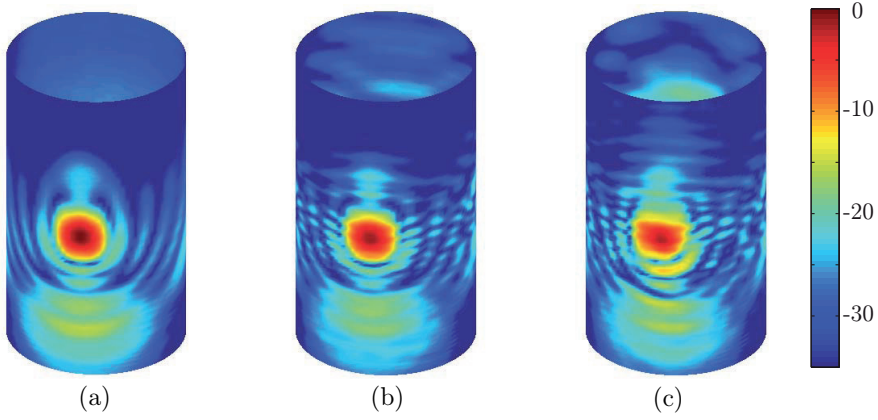
Figure 4: The co-component, $|E^{\mathrm{v}}|_{\mathrm{dB}}$, of the experimentally measured near-field data at 8.0 GHz, normalized with the largest value of $|E^{\mathrm{v}}|$ when no radome is present. (a) No radome present. (b) Radome present. (c) Defect radome present.
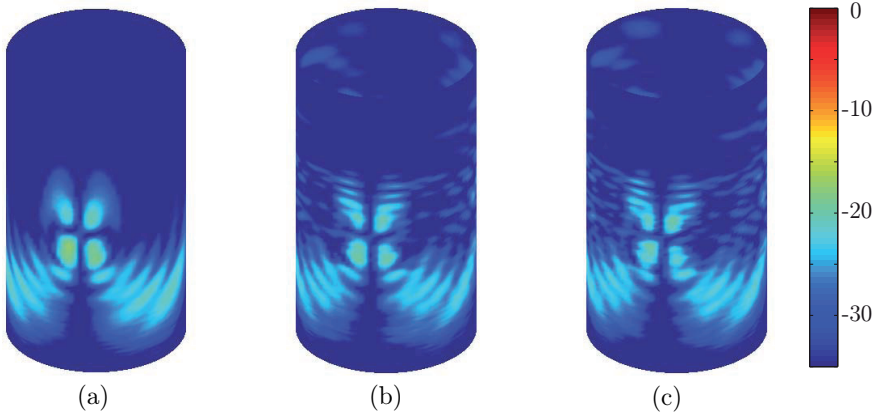
Figure 5: The cross-component, $|E^{\varphi}|_{\mathrm{dB}}$, of the experimentally measured near-field data at 8.0 GHz, normalized with the largest value of $|E^{\mathrm{v}}|$ when no radome is present. (a) No radome present. (b) Radome present. (c) Defect radome present.
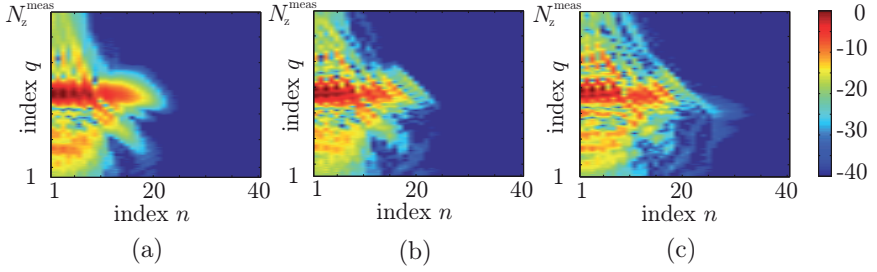
Figure 6: The Fourier transformed measured field, $|E^{\mathrm{v}}|_{\mathrm{dB}}$, at $8.0\,\mathrm{GHz}$. All values are normalized with the largest value of $|E^{\mathrm{v}}|$ when no radome is present. a) No radome present. (b) Radome present. (c) Defect radome present.
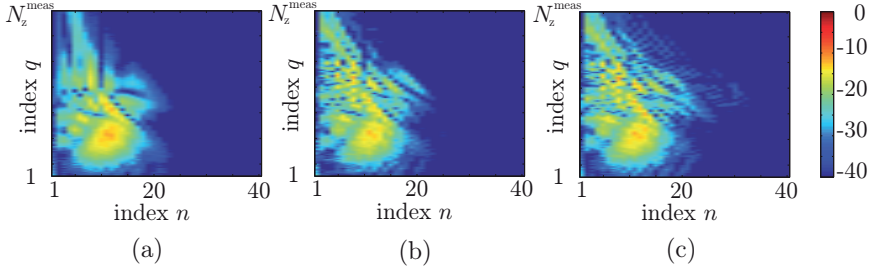
Figure 7: The Fourier transformed measured field, $|E^{\varphi}|_{\mathrm{dB}}$, at $8.0\,\mathrm{GHz}$. All values are normalized with the largest value of $|E^{\mathrm{v}}|$ when no radome is present. (a) No radome present. (b) Radome present. (c) Defect radome present.

the largest value of $|E^{\mathrm{v}}|$ when no radome is present. In particular, E^{φ} has a quite complicated pattern. The diffraction is explained as environmental reflections and an off-centered antenna feed. Observe that the amplitude of the azimuth component is smaller than the amplitude of the height component, $i.e.$, measurement errors are more likely to show up here. The differences between the three different antenna and radome cases arise from constructive and destructive interference between the radiated field and the scattered field. The absolute value of the Fourier transformed measured fields are shown in dB-scale in Figures 6–7. According to these figures, the spectrum is truncated at $n = 30$, above which the energy contents is too low.

4   Results

The measured field on the cylindrical surface at $8.0\,\mathrm{GHz}$, $cf.$, Figures 4 and 5, is transformed back onto a surface corresponding to the radome surface. Figures 8 and 9 show the recreated electric fields, $|E^{\mathrm{v}}|_{\mathrm{dB}}$ and $|E^{\varphi}|_{\mathrm{dB}}$, respectively, in the main
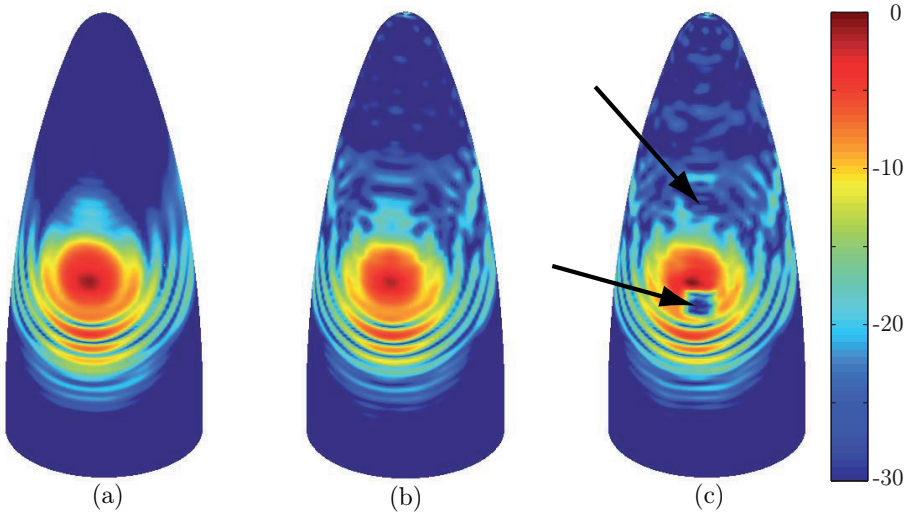
Figure 8: The recreated $|E^{\mathrm{v}}|_{\mathrm{dB}}$-component on the front side of the radome. All values are normalized with the largest value of $|E^{\mathrm{v}}|$ when the defect radome is present. (a) No radome present. (b) Radome present. (c) Defect radome present. The arrows point out the locations of the copper plates.

lobe for the different configurations. Observe that all values are normalized with the largest value of $|E^{\mathrm{v}}|$ when the defect radome is present. The figures show that the near field close to the antenna is complex and hard to predict. In the case, when no radome is located around the antenna, the electric fields are calculated on a surface shaped as the radome, see Figures 8a and 9a. The case when the radome is present, see Figures 8b and 9b, shows that the radome interacts with the antenna and hence disturbs the radiated field. How this interaction affects the amplitude is depicted in Figures 10a and b, where $(|E^{\mathrm{v}}_{\mathrm{no\ radome}}| - |E^{\mathrm{v}}_{\mathrm{radome}}|)$ and $(|E^{\varphi}_{\mathrm{no\ radome}}| - |E^{\varphi}_{\mathrm{radome}}|)$ are shown in a linear scale and normalized with the maximum difference for each component. Both components of the electric field are reduced in amplitude in the main lobe whereas the field strength outside the main lobe is increased when the radome is introduced. This is most likely due to transmission loss in the radome wall and scattering against the inside wall.

The effect of the attached copper plates are detected as shown in Figures 8c and 9c, where the lower plate appears clearly. Observe that the copper plates cannot be localized directly in the near-field data, compare Figures 4c and 5c to Figures 8c and 9c. The near-field data only shows that the field is disturbed, not the locations of the disturbances. The upper plate is hard to discern in Figures 8c and 9c since it is located in a region with small field magnitudes. However, the influence of the upper copper plate can be detected in the cross section graphs, see Figures 11a and b. To determine the exact position of the defects several cross section graphs
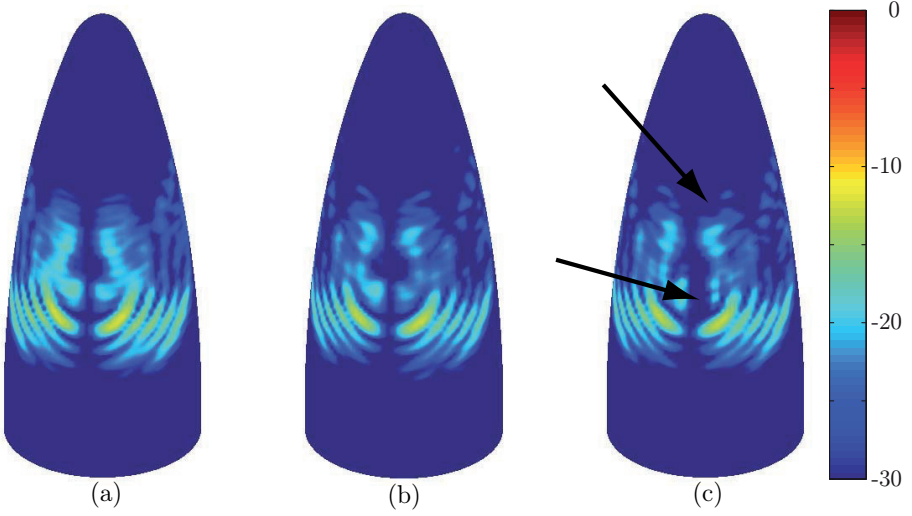
Figure 9: The recreated $|E^\varphi|_{\mathrm{dB}}$-component on the front side of the radome. All values are normalized with the largest value of $|E^{\mathrm{v}}|$ when the defect radome is present. (a) No radome present. (b) Radome present. (c) Defect radome present. The arrows point out the locations of the copper plates.

have to be examined. It is interesting to see that even though the magnitude of the cross-polarization is small, the locations of the copper plates can be found.

The presence of the radome also creates some backscattering (flash lobes) as seen in Figures 11 c–d, 12, and 13. In Figures 11 c–d, a cross section at an angle 180° from the center of the main lobe, $i.e.$, in the middle of the back side, is viewed. Figures 12 and 13 depict both components on the back side of the radome for all three configurations in a dB-scale. In these figures it is also observed that the flash lobes are altered when the copper plates are present.

The copper plates can also be detected by subtracting the field of the defect radome and the field of the non-defect radome. This result is shown in dB-scale in Figure 14 for both the components of the electric field, $i.e.$, $|E^{\mathrm{v}}_{\mathrm{radome}} - E^{\mathrm{v}}_{\mathrm{def\,radome}}|_{\mathrm{dB}}$ and $|E^{\varphi}_{\mathrm{radome}} - E^{\varphi}_{\mathrm{def\,radome}}|_{\mathrm{dB}}$, each component normalized with the maximum difference for each component. The reconstruction of the E^φ-component, $cf.$, Figure 14b, only shows the effects of some parts of the copper plates. The reason is that parts of the copper plates are located in an area where the amplitude of the E^φ-component is small, $cf.$, Figure 5 and 9a.

Figure 14a indicates that there is an amplitude difference between the configurations slightly above the location of the lower copper plate. To visualize what is happening, the difference $(|E^{\mathrm{v}}_{\mathrm{radome}}| - |E^{\mathrm{v}}_{\mathrm{def\,radome}}|)$, normalized with its maximum value, in a linear scale, is depicted in Figure 15. The scale is truncated in order to see the small field difference above the copper plate. Here it becomes clear that the
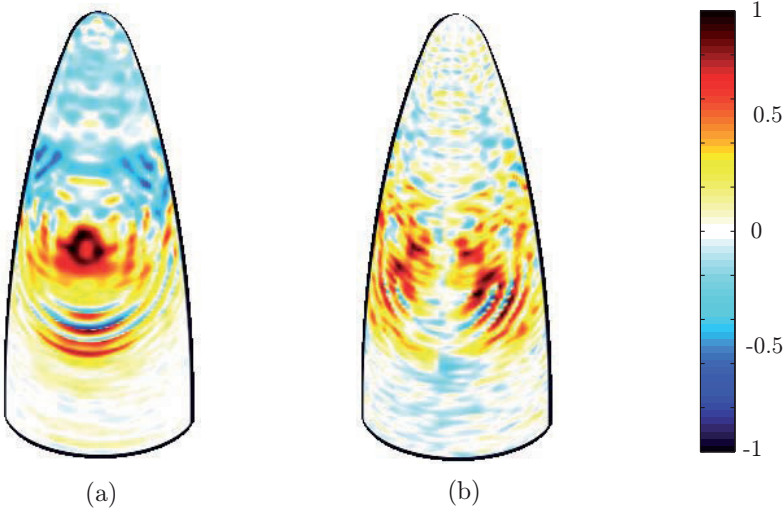
Figure 10: The subtraction between the fields with and without radome present. In (a) $(|E^{\mathrm{v}}_{\mathrm{no\ radome}}| - |E^{\mathrm{v}}_{\mathrm{radome}}|)/\max||E^{\mathrm{v}}_{\mathrm{no\ radome}}| - |E^{\mathrm{v}}_{\mathrm{radome}}||$ is shown and in (b) $(|E^{\varphi}_{\mathrm{no\ radome}}| - |E^{\varphi}_{\mathrm{radome}}|)/\max||E^{\varphi}_{\mathrm{no\ radome}}| - |E^{\varphi}_{\mathrm{radome}}||$. The front side of the radome, *i.e.*, the side with the main lobe, is viewed. The scale is linear.

area, where the copper plate is attached, has a reduced electric field, when the defect radome is present. The area above the copper plate has instead an increased electric field, when the defect radome is present. This is most likely due to scattering of the copper plate.

So far only the amplitudes of the reconstructed fields has been investigated. However, even the phase can give useful information. The phase of the E^{v}-component, *i.e.*, $\angle E^{\mathrm{v}}$, where $\angle$ denotes the argument, is depicted in Figure 16 for all configurations. The vertical lines above the main lobe in Figure 16a are due to phase jumps, and are caused by the low amplitude of the fields in these areas.

Just showing the phase as in Figure 16 does not give very much information. What is interesting is to study the phase difference (antenna - antenna with radome) for the two recreated components, see Figure 17. It reveals how the phase is changed due to the influence of the radome. It is observed that the phase shift in the main lobe is almost constant, for both components. This confirms that the radome is well adapted to the frequency $8.0\,\mathrm{GHz}$. Since the amplitude of E^{φ} is low, *cf.*, Figures 5 and 9, its phase contains much noise, and it is therefore somewhat more unreliable than $\angle E^{\mathrm{v}}$.

In Figure 18, a cross section in the middle of the main lobe of the phase difference in Figure 17 is depicted. The cross section of $\angle E^{\varphi}$ is shown for a slightly acentric angle, since the amplitude in the center of the main lobe is very low, see Figure 9. In areas where the field is strong, the phase shift does not fluctuate as much. Outside
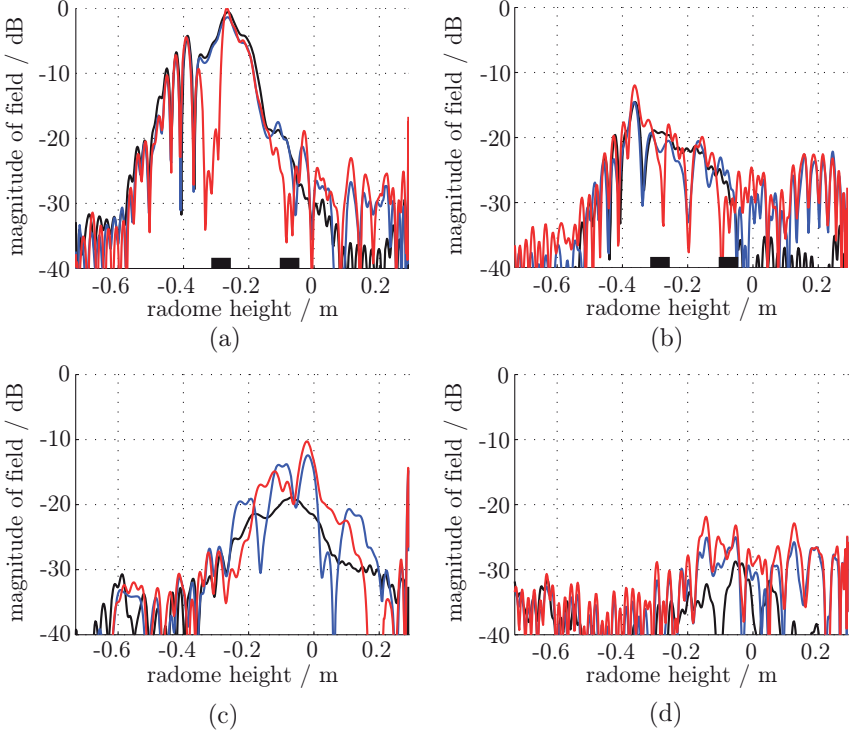
Figure 11: Cross sections of the reconstructed field components. (a) $|E^{\mathrm{v}}|_{\mathrm{dB}}$ in the main lobe. (b) $|E^{\varphi}|_{\mathrm{dB}}$ in the main lobe. (c) $|E^{\mathrm{v}}|_{\mathrm{dB}}$ on the back of the radome. (d) $|E^{\varphi}|_{\mathrm{dB}}$ on the back of the radome. All values are normalized with the maximum value of $|E^{\mathrm{v}}|$ when the defect radome is present. The black line corresponds to no radome, the blue line has the radome present and the red line represents the defect radome. The positions of the copper plates on the defect radome are marked by thick lines on the horizontal axis.
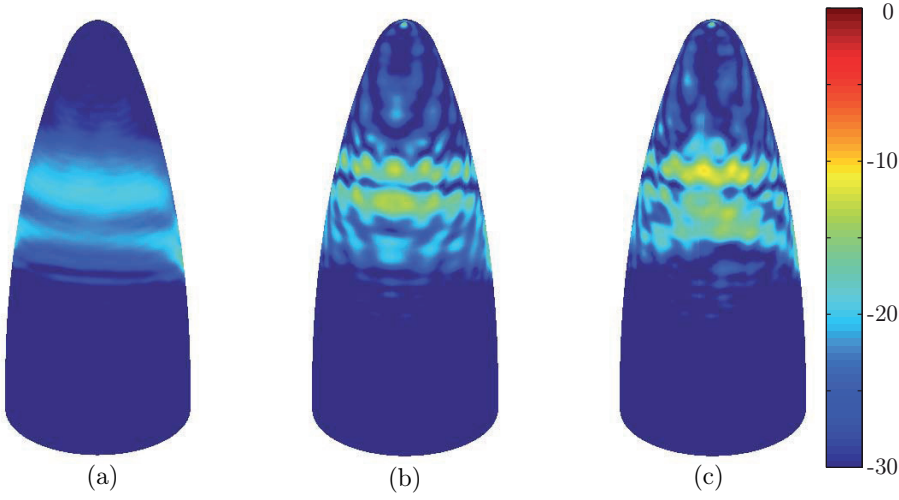
Figure 12: The recreated $|E^{\mathrm{v}}|_{\mathrm{dB}}$-component on the back side of the radome. All values are normalized with the maximum value of $|E^{\mathrm{v}}|$, on the front side, when the defect radome is present. (a) No radome present. (b) Radome present. (c) Defect radome present.
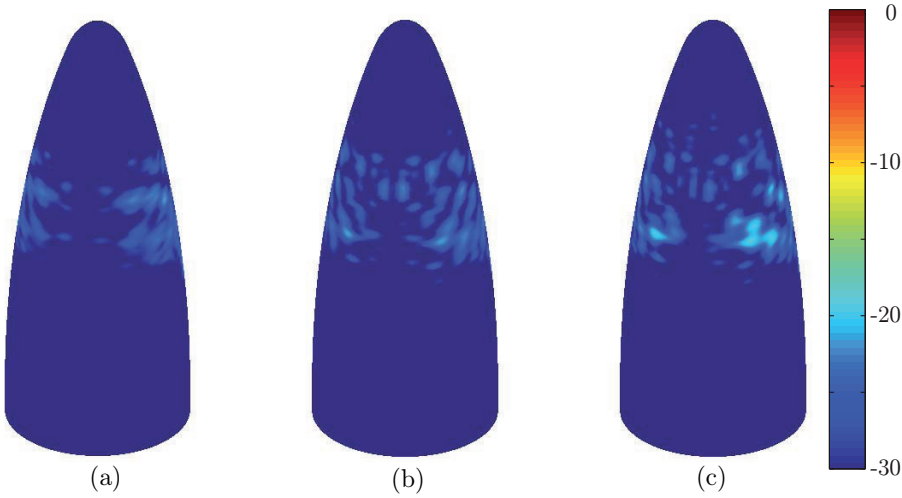
Figure 13: The recreated $|E^{\varphi}|_{\mathrm{dB}}$-component on the back side of the radome. All values are normalized with the maximum value of $|E^{\mathrm{v}}|$, on the front side, when the defect radome is present. (a) No radome present. (b) Radome present. (c) Defect radome present.
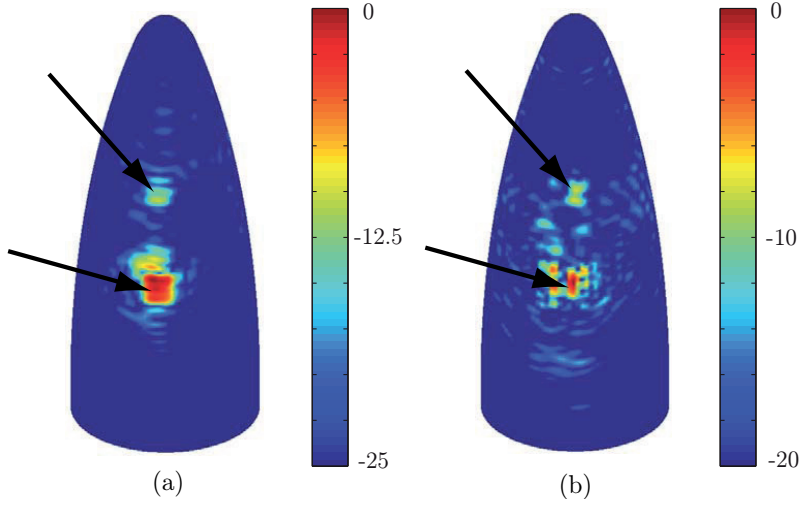
Figure 14: The logarithmic differences revealing the copper plates, (a) $20 \log\{|E^{\mathrm{v}}_{\mathrm{radome}} - E^{\mathrm{v}}_{\mathrm{def\ radome}}| / \max|E^{\mathrm{v}}_{\mathrm{radome}} - E^{\mathrm{v}}_{\mathrm{def\ radome}}|\}$, and (b) $20 \log\{|E^{\varphi}_{\mathrm{radome}} - E^{\varphi}_{\mathrm{def\ radome}}| / \max|E^{\varphi}_{\mathrm{radome}} - E^{\varphi}_{\mathrm{def\ radome}}|\}$ on the front side of the radome. The arrows point out the locations of the copper plates.
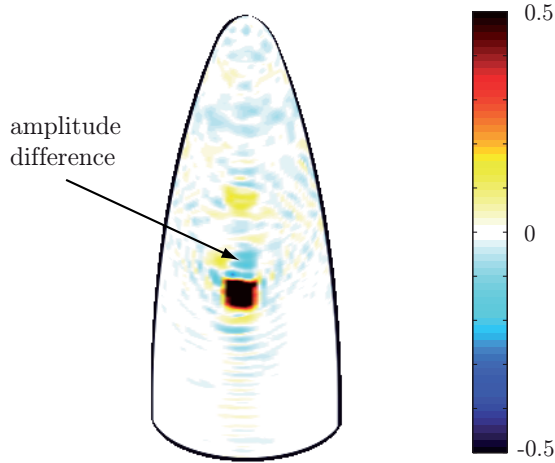
Figure 15: The difference $(|E^{\mathrm{v}}_{\mathrm{radome}}| - |E^{\mathrm{v}}_{\mathrm{def\ radome}}|) / \max||E^{\mathrm{v}}_{\mathrm{radome}}| - |E^{\mathrm{v}}_{\mathrm{def\ radome}}||$ in a linear scale on the front side of the radome. The scale is truncated in order to see the small field amplitude above the copper plate, marked with an arrow.
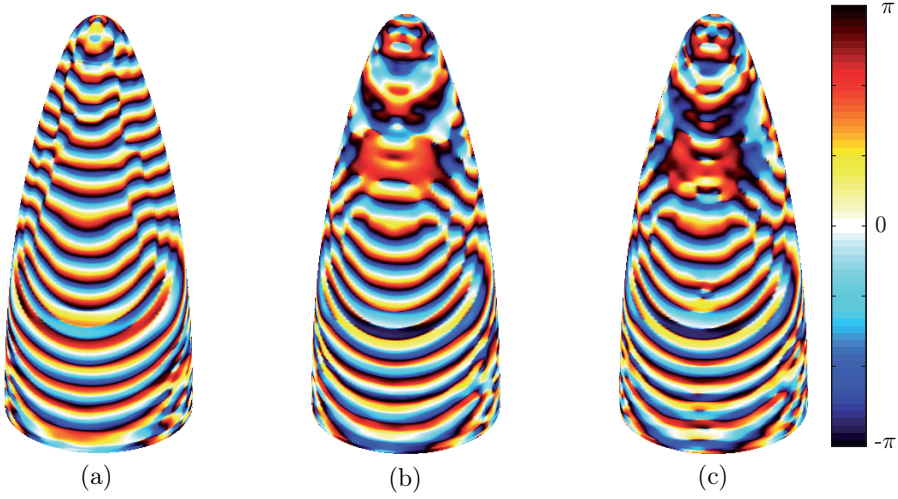
Figure 16: The recreated phase of the E^{v}-component on the front side of the radome in a linear scale. a) No radome present. b) Radome present. c) Defect radome present.
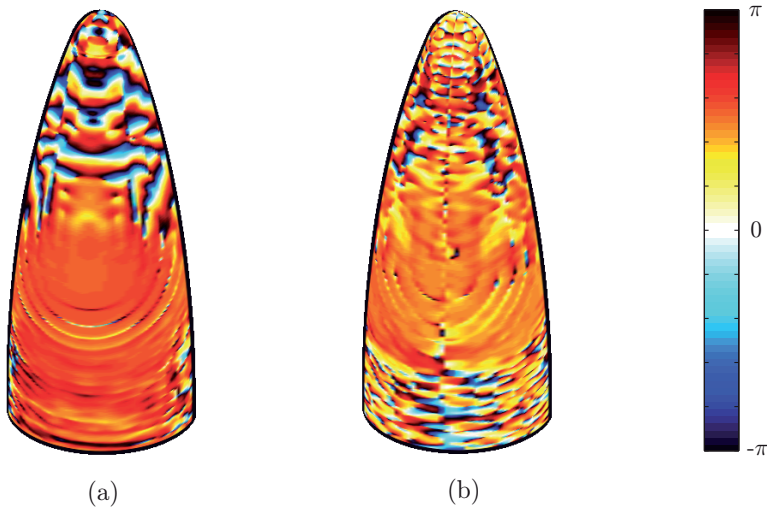
Figure 17: The IPD, $i.e.$, the phase difference between the field when no radome is present and the field when the radome is present, on the front side of the radome. a) $(\angle E^{\mathrm{v}}_{\text{no radome}} - \angle E^{\mathrm{v}}_{\text{radome}})$. b) $(\angle E^{\varphi}_{\text{no radome}} - \angle E^{\varphi}_{\text{radome}})$.
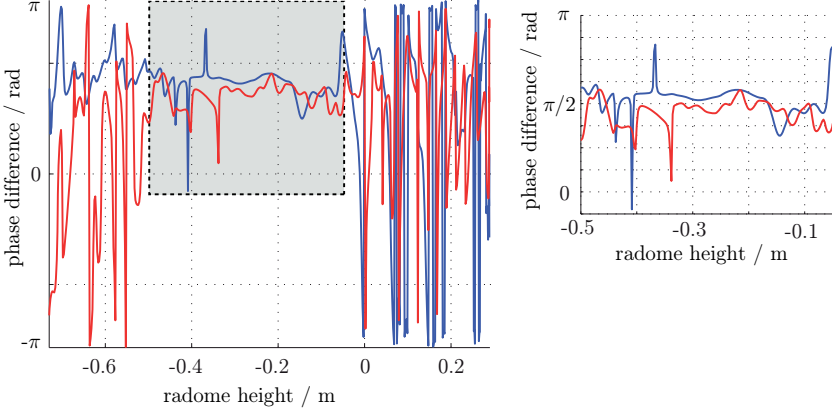
Figure 18: Cross section in the middle of the main lobe of the IPD depicted in Figure 17. The blue line corresponds to $(\angle E^{\mathrm{v}}_{\mathrm{no\ radome}} - \angle E^{\mathrm{v}}_{\mathrm{radome}})$ and the red to $(\angle E^{\varphi}_{\mathrm{no\ radome}} - \angle E^{\varphi}_{\mathrm{radome}})$, respectively. The insert shows the area with reliable data.

(a)   (b)
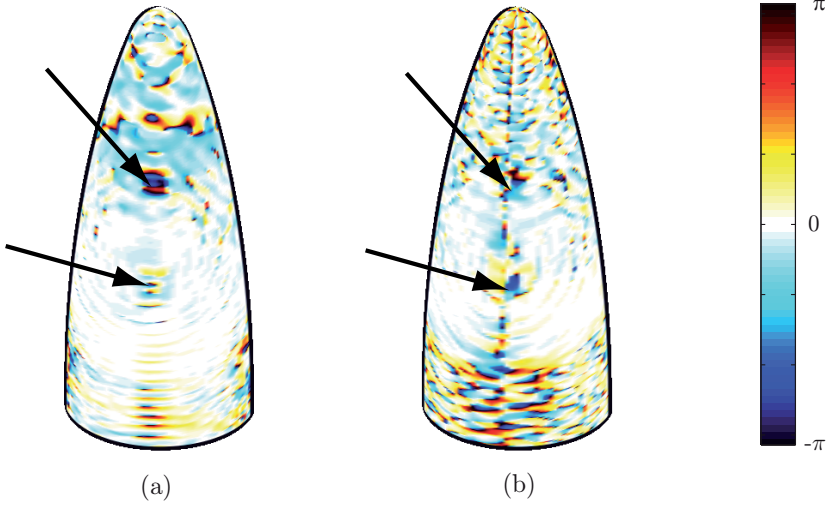
Figure 19: The phase difference between the field when the radome is present and the field when the defect radome is present, on the front side of the radome. The arrows point out the copper plates. a) $(\angle E^{\mathrm{v}}_{\mathrm{radome}} - \angle E^{\mathrm{v}}_{\mathrm{def\ radome}})$. b) $(\angle E^{\varphi}_{\mathrm{radome}} - \angle E^{\varphi}_{\mathrm{def\ radome}})$.
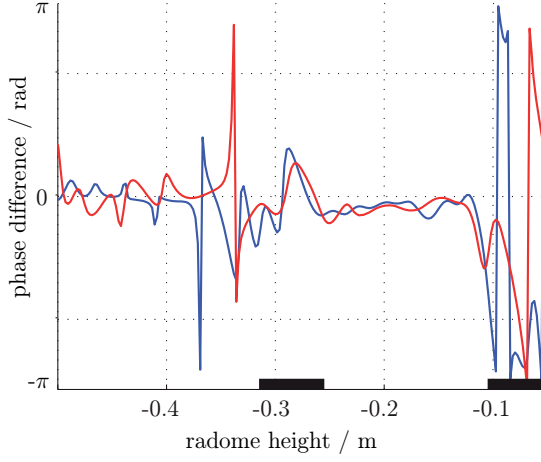
Figure 20: Cross section in the middle of the main lobe of the phase differences depicted in Figure 19. The axis describing the radome height is truncated and shows only the region where the phase information is reliable, *cf.*, Figure 18. The blue line corresponds to $(\angle E^{\mathrm{v}}_{\mathrm{radome}} - \angle E^{\mathrm{v}}_{\mathrm{def\ radome}})$ and the red to $(\angle E^{\varphi}_{\mathrm{radome}} - \angle E^{\varphi}_{\mathrm{no\ radome}})$, respectively.

this areas the amplitude is low and the phase is not well defined, *i.e.*, dominated by noise, and it will not give valid information. This means that when looking at the main lobe, the only area that contains reliable values is $z \in [-0.5, -0.05]$.

The phase shift arising when the radome is introduced, *i.e.*, the phase shift viewed in Figures 17 and 18, is called the IPD (Insertion Phase Delay). It is one of the parameters that quantifies the performance of the radome, and depending on the polarization, two different IPD are defined [19]

$$T = |T|\angle \mathrm{IPD} \tag{4.1}$$

where $T = E_{\mathrm{t}}/E_{\mathrm{i}}$ is the complex transmission coefficient. The incoming field is denoted E_{i}, and the transmitted E_{t}. The phase shift is only known modulus 2π. To validate the calculation of the IPD, an estimation of the thickness of the radome wall is carried out. Under the assumption of negligible reflections the IPD can be expressed as [18, 21]

$$\mathrm{IPD} = \frac{\omega}{\mathrm{c}} \left\{ \mathrm{Re} \sqrt{\epsilon_{\mathrm{r}}(1 - \mathrm{j} \tan \delta)} \cos \theta_{\mathrm{t}} - \cos \theta_{\mathrm{i}} \right\} d \tag{4.2}$$

for both polarizations, where ω is the angular frequency, c is the speed of light in vacuum, θ_{i} is the incident angle, and θ_{t} is the transmission angle of the field on the inside of the radome wall. Approximate values of the relative permittivity, $\epsilon_{\mathrm{r}} \approx 4.32$, and the loss tangent, $\tan \delta \approx 0.0144$, are used. The thickness of the radome wall is
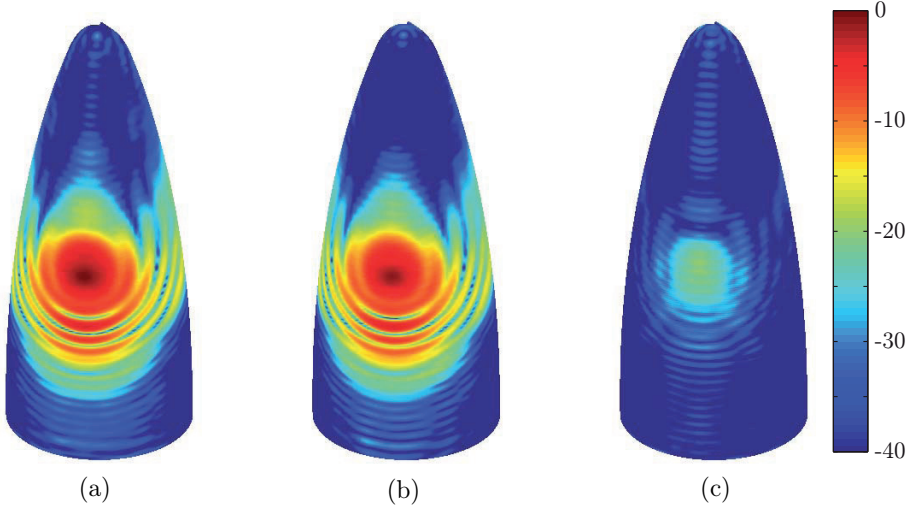
Figure 21: A comparison between the code based on the scalar and full vector integral representation when no radome is present. All values are shown i dB-scale and normalized with the maximum value of $|E^\mathrm{v}|$. (a) Vector code, $|E^\mathrm{v}|_\mathrm{dB}$. (b) Scalar code, $|E^\mathrm{z}/\cos\theta|_\mathrm{dB}$. (c) Difference, $|E^\mathrm{v} - E^\mathrm{z}/\cos\theta|_\mathrm{dB}$.

denoted d. The incident angle is approximated to 40º, $cf.$, Figure 3b. The measured radome thickness, d, varies over the surface in the interval $7.6 - 8.2$ mm. The phase shift in the main lobe is crudely approximated from Figure 18 to be 1.7 rad for both components/polarizations. Solving for d in (4.2) results in a radome thickness of 8.4 mm. The agreement is quite well considering the approximations made.

An investigation of the phase difference (radome - defect radome), see Figures 19 and 20, reveals that its harder to localize the actual positions of the copper plates by using the phase instead of only the amplitude, $cf.$, Figures 8 and 9. Nevertheless, the upper copper plate is visible in the 3-D visualization in Figure 19a, and by looking at a cross section over the main lobe of the phase difference, the position of the upper copper plate is located for both components, see Figure 20. We only show the interval, where the phase is not too contaminated by noise, $cf.$, Figure 18. The upper copper plate is located on the boundary to where noise dominates. Thus, if the positions of the copper plate were not known in advance, the phase shift might be interpreted as noise. The lower copper plate also introduces a phase shift, but these effects are hard to interpret and not confined to the exact position of the plate.

4.1   Verification

To verify the code, the new results for the E^v-component is compared with the results given by the scalar integral representation, see [32, 33]. The comparison is

shown in Figure 21 for the case when no radome is present. In the scalar case, the E^z-component is calculated whereas in the vector code it is the component tangential to the surface, *i.e.*, E^v. To compensate for this the E^z-component is divided by $\cos\theta$, where θ is the angle between the z-axis and the radome surface. In Figure 21 all fields are normalized with the maximum value of $|E^v|$ and shown in dB-scale. We notice that the field pattern given by both codes are very similar. The amplitudes are higher in the vector case, and the largest difference, about $-19\,$dB, occurs in the main lobe where both field-components are strong. This is evident since the interaction between both field components, E^v and E^φ, is taken into account in the vector calculations. Whereas, in the scalar case, E^φ was assumed to be zero. Verification of the scalar code has been made in [32]. Specifically, the reconstructed fields on the radome surface was transformed to the far field. Comparison with measured far field shows good agreement.

5   Conclusions

The aim of this paper is to reconstruct equivalent currents on a surface bounding the sources of an electromagnetic field. A vector-valued surface integral representation is utilized together with the extinction theorem. The surface integral representation gives a linear map between the equivalent surface currents and the near-field data for general geometries. It is shown that this map can be inverted for axially symmetric geometries with the measured near field. The theory can be adapted to geometries lacking symmetry axes. However, it is not a feasible approach for radome applications today due to the computational demand to solve the integral equations. An alternative approach would be to address this problem using fast multipoles methods [43].

In previous papers only the dominating vertical co-component of the measured field has been used in the reconstruction by using a scalar integral representation, where comparison with measured far field shows good agreement [32, 33]. In this paper it is shown that both components of the equivalent currents can be reconstructed by using a full-wave surface integral representation. The results for the cross-component show that also this component provides useful insight of the complex field close to the antenna and the field altered by the radome. It is illustrated how the radome interacts with the electric field. In particular, transmission losses in the radome wall and reflections on the inside decrease the field in the main lobe, and new side and flash lobes appear. Both components of the experimentally measured field can also be used to locate the effect of defects, *i.e.*, copper plates, not directly visible in the measured near-field data. Furthermore, the copper plates introduce scattering and alter the flash lobes.

Also, the phase of the reconstructed fields is investigated. The IPD, *i.e.*, the phase difference, arising when the radome is located between the antenna and the measurement probe, is visualized. The results give a good estimate of the thickness of the radome wall. The effects of the copper plates are visible in the phase shift. However, the exact location of the defects is hard to determine solely from the phase

images.

By comparison with the results given by the scalar integral representation, it is concluded that the patterns of the electric field, obtained by the different codes, are similar. The amplitude does however differ somewhat between the codes. This result is expected since in the scalar case assumes zero azimuthal component of the measured electric field. However, in this paper, the interaction between both components is taken into consideration.

This paper shows the potentials of the approach in radome diagnostics. Next step is to analyze if the electric equivalent current, *i.e.*, the magnetic field, on the radome surface gives some more information. Moreover, investigations with different frequencies are expected. To localize the exact positions of the defects, a deeper analyze of 3D-pictures, *cf.*, Figures 8c and 9c, and cross-section graphs, *cf.*, Figure 11, combined with the phase shift data, is planned. To use this method in verifying radomes, *i.e.*, calculating the IPD, more analysis of the phase and its noise levels is needed.

Acknowledgements

Appendix A   Investigation of the weak formulation

In this appendix, the weak formulation of (2.5) is evaluated. The aim is to show that all singularities are removable, and the final result is presented in (2.6).

The weak formulation is attained by multiplying with a test function and integrating over the domain. We chose to multiply with the test function

$$\boldsymbol{\Psi}^{\mathrm{ort}} = -\hat{\boldsymbol{n}} \times \boldsymbol{\Psi}$$

The reason for this choice will become clear as we proceed.

Term 1:

$$\iint\limits_{S_{\mathrm{rad}}} \boldsymbol{\Psi}^{\mathrm{ort}}(\boldsymbol{r}_2) \cdot \left(\hat{\boldsymbol{n}}(\boldsymbol{r}_2) \times \iint\limits_{S_{\mathrm{rad}}} g(\boldsymbol{r}_1, \boldsymbol{r}_2) \boldsymbol{J}(\boldsymbol{r}_1) \, \mathrm{d}S_1 \right) \mathrm{d}S_2$$

$$= -\iint\limits_{S_{\mathrm{rad}}} \left(\iint\limits_{S_{\mathrm{rad}}} g(\boldsymbol{r}_1, \boldsymbol{r}_2) \boldsymbol{J}(\boldsymbol{r}_1) \, \mathrm{d}S_1 \right) \cdot \left\{ \hat{\boldsymbol{n}}(\boldsymbol{r}_2) \times \boldsymbol{\Psi}^{\mathrm{ort}}(\boldsymbol{r}_2) \right\} \mathrm{d}S_2$$

$$= -\iint\limits_{S_{\mathrm{rad}}} \iint\limits_{S_{\mathrm{rad}}} \boldsymbol{\Psi}(\boldsymbol{r}_2) \cdot g(\boldsymbol{r}_1, \boldsymbol{r}_2) \boldsymbol{J}(\boldsymbol{r}_1) \, \mathrm{d}S_1 \, \mathrm{d}S_2$$

The integral causes no numerical problems since the singularity in $g(\boldsymbol{r}_1, \boldsymbol{r}_2)$ is integrable.

Term 2:

$$\iint\limits_{S_{\mathrm{rad}}} \boldsymbol{\Psi}^{\mathrm{ort}}(\boldsymbol{r}_2) \cdot \left(\hat{\boldsymbol{n}}(\boldsymbol{r}_2) \times \iint\limits_{S_{\mathrm{rad}}} \nabla_1 g(\boldsymbol{r}_1, \boldsymbol{r}_2) \left[\nabla_{1S} \cdot \boldsymbol{J}(\boldsymbol{r}_1) \right] \mathrm{d}S_1 \right) \mathrm{d}S_2$$

$$= -\iint\limits_{S_{\mathrm{rad}}} \boldsymbol{\Psi}^{\mathrm{ort}}(\boldsymbol{r}_2) \cdot \left(\hat{\boldsymbol{n}}(\boldsymbol{r}_2) \times \nabla_2 \underbrace{\iint\limits_{S_{\mathrm{rad}}} g(\boldsymbol{r}_1, \boldsymbol{r}_2) \left[\nabla_{1S} \cdot \boldsymbol{J}(\boldsymbol{r}_1) \right] \mathrm{d}S_1}_{K(\boldsymbol{r}_2)} \right) \mathrm{d}S_2$$

$$\overset{(1)}{=} -\iint\limits_{S_{\mathrm{rad}}} \boldsymbol{\Psi}^{\mathrm{ort}}(\boldsymbol{r}_2) \cdot \left(\hat{\boldsymbol{n}}(\boldsymbol{r}_2) \times \left\{ \nabla_{2S} + \hat{\boldsymbol{n}}(\boldsymbol{r}_2) \left[\hat{\boldsymbol{n}}(\boldsymbol{r}_2) \cdot \nabla_2 \right] \right\} K(\boldsymbol{r}_2) \right) \mathrm{d}S_2$$

$$= -\iint\limits_{S_{\mathrm{rad}}} \boldsymbol{\Psi}^{\mathrm{ort}}(\boldsymbol{r}_2) \cdot \left[\hat{\boldsymbol{n}}(\boldsymbol{r}_2) \times \nabla_{2S} K(\boldsymbol{r}_2) \right] \mathrm{d}S_2 = \iint\limits_{S_{\mathrm{rad}}} \boldsymbol{\Psi}(\boldsymbol{r}_2) \cdot \nabla_{2S} K(\boldsymbol{r}_2) \, \mathrm{d}S_2$$

$$\overset{(2)}{=} \iint\limits_{S_{\mathrm{rad}}} \nabla_{2S} \cdot \left[\boldsymbol{\Psi}(\boldsymbol{r}_2) K(\boldsymbol{r}_2) \right] \mathrm{d}S_2 - \iint\limits_{S_{\mathrm{rad}}} \left[\nabla_{2S} \cdot \boldsymbol{\Psi}(\boldsymbol{r}_2) \right] K(\boldsymbol{r}_2) \, \mathrm{d}S_2$$
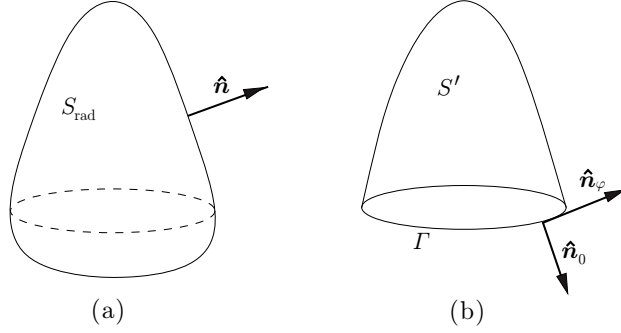
Figure 22: (a) The surface S_{rad} and its outward unit vector $\hat{\boldsymbol{n}}$. (b) The surface S' bounded by the curve Γ. The unit normal vectors are; $\hat{\boldsymbol{n}}_\varphi$ - tangent to Γ and S', $\hat{\boldsymbol{n}}_0$ tangent to S' and normal to Γ. That is $\hat{\boldsymbol{n}}_0 = \hat{\boldsymbol{n}}_\varphi \times \hat{\boldsymbol{n}}$.

$$
\stackrel{(3)}{=} \int_\Gamma \hat{\boldsymbol{n}}_0(\boldsymbol{r}_2) \cdot \big[\boldsymbol{\Psi}(\boldsymbol{r}_2) K(\boldsymbol{r}_2) \big] \, \mathrm{d}\Gamma - \iint_{S_{\mathrm{rad}}} \big[\nabla_{2S} \cdot \boldsymbol{\Psi}(\boldsymbol{r}_2) \big] K(\boldsymbol{r}_2) \, \mathrm{d}S_2
$$
$$
= - \iint_{S_{\mathrm{rad}}} \iint_{S_{\mathrm{rad}}} \big[\nabla_{2S} \cdot \boldsymbol{\Psi}(\boldsymbol{r}_2) \big] g(\boldsymbol{r}_1, \boldsymbol{r}_2) \big[\nabla_{1S} \cdot \boldsymbol{J}(\boldsymbol{r}_1) \big] \, \mathrm{d}S_1 \, \mathrm{d}S_2
$$

The nabla operator is divided into one part intrinsic to the surface and one part operating in the direction normal to the surface in step 1, *i.e.*, $\nabla_{2S} = \nabla_2 - \hat{\boldsymbol{n}}(\boldsymbol{r}_2)\big[\hat{\boldsymbol{n}}(\boldsymbol{r}_2) \cdot \nabla_2\big]$ [9, 48]. In step 2 the identity $\nabla_S \cdot (f\boldsymbol{a}) = f(\nabla_S \cdot \boldsymbol{a}) + (\nabla_S f) \cdot \boldsymbol{a}$ is utilized [48]. Step 3 uses the theorem of Gauss on surfaces where $\hat{\boldsymbol{n}}_0(\boldsymbol{r}_2)$ and Γ are depicted in Figure 22 [29]. The line integral over the closed surface is zero, since there is no bounding curve on S_{rad} [1].

Term 3:
$$
\iint_{S_{\mathrm{rad}}} \boldsymbol{\Psi}^{\mathrm{ort}}(\boldsymbol{r}_2) \cdot \left(\hat{\boldsymbol{n}}(\boldsymbol{r}_2) \times \iint_{S_{\mathrm{rad}}} \nabla_1 g(\boldsymbol{r}_1, \boldsymbol{r}_2) \times \boldsymbol{M}(\boldsymbol{r}_1) \, \mathrm{d}S_1 \right) \, \mathrm{d}S_2
$$
$$
= - \iint_{S_{\mathrm{rad}}} \boldsymbol{\Psi}(\boldsymbol{r}_2) \cdot \iint_{S_{\mathrm{rad}}} \nabla_1 g(\boldsymbol{r}_1, \boldsymbol{r}_2) \times \boldsymbol{M}(\boldsymbol{r}_1) \, \mathrm{d}S_1 \, \mathrm{d}S_2
$$
(A.1)

The gradient of the Green function cannot easily be moved to the test function. However, it is shown below that the singularity is removable.

We start by rewriting the expression, *i.e.*,

$$\iint\limits_{S_{\text{rad}}} \boldsymbol{\Psi}(\boldsymbol{r}_2) \cdot \iint\limits_{S_{\text{rad}}} \nabla_1 g(\boldsymbol{r}_1, \boldsymbol{r}_2) \times \boldsymbol{M}(\boldsymbol{r}_1) \, \mathrm{d}S_1 \, \mathrm{d}S_2$$

$$\overset{(1)}{=} \iint\limits_{S_{\text{rad}}} \boldsymbol{\Psi}(\boldsymbol{r}_2) \cdot \iint\limits_{S_{\text{rad}}} \nabla_1 g(\boldsymbol{r}_1, \boldsymbol{r}_2) \times \left[\hat{\boldsymbol{n}}(\boldsymbol{r}_1) \times \widetilde{\boldsymbol{M}}_{\text{S}}(\boldsymbol{r}_1) \right] \, \mathrm{d}S_1 \, \mathrm{d}S_2$$

$$= \iint\limits_{S_{\text{rad}}} \boldsymbol{\Psi}(\boldsymbol{r}_2) \cdot \iint\limits_{S_{\text{rad}}} \hat{\boldsymbol{n}}(\boldsymbol{r}_1) \left[\nabla_1 g(\boldsymbol{r}_1, \boldsymbol{r}_2) \cdot \widetilde{\boldsymbol{M}}_{\text{S}}(\boldsymbol{r}_1) \right] \, \mathrm{d}S_1 \, \mathrm{d}S_2$$

$$- \iint\limits_{S_{\text{rad}}} \boldsymbol{\Psi}(\boldsymbol{r}_2) \cdot \iint\limits_{S_{\text{rad}}} \widetilde{\boldsymbol{M}}_{\text{S}}(\boldsymbol{r}_1) \left[\nabla_1 g(\boldsymbol{r}_1, \boldsymbol{r}_2) \cdot \hat{\boldsymbol{n}}(\boldsymbol{r}_1) \right] \, \mathrm{d}S_1 \, \mathrm{d}S_2$$

(A.2)

where $\widetilde{\boldsymbol{M}}_{\text{S}}(\boldsymbol{r}_1)$ is introduced as $\boldsymbol{M}(\boldsymbol{r}_1) \equiv \hat{\boldsymbol{n}}(\boldsymbol{r}_1) \times \widetilde{\boldsymbol{M}}_{\text{S}}(\boldsymbol{r}_1)$, in step 1.

The gradient of the Green's function is, *cf.*, (2.2)

$$\nabla_1 g(\boldsymbol{r}_1, \boldsymbol{r}_2) = \frac{\mathrm{e}^{-\mathrm{j}k|\boldsymbol{r}_2 - \boldsymbol{r}_1|}}{4\pi} \frac{\boldsymbol{r}_2 - \boldsymbol{r}_1}{|\boldsymbol{r}_2 - \boldsymbol{r}_1|^2} \left[\frac{1}{|\boldsymbol{r}_2 - \boldsymbol{r}_1|} + \mathrm{j}k \right]$$

The singularity in $\frac{\boldsymbol{r}_2 - \boldsymbol{r}_1}{|\boldsymbol{r}_2 - \boldsymbol{r}_1|^2}$ is integrable. However, the first term has an additionally singularity $\frac{1}{|\boldsymbol{r}_2 - \boldsymbol{r}_1|}$ that needs to be dealt with.

To remove the singularity in the first term of (A.2), we show that $\boldsymbol{\Psi}(\boldsymbol{r}_2) \cdot \hat{\boldsymbol{n}}(\boldsymbol{r}_1) \leqslant K|\boldsymbol{r}_2 - \boldsymbol{r}_1|$ as $\boldsymbol{r}_1 \to \boldsymbol{r}_2$ and K is a constant. A Taylor expansion of $\hat{\boldsymbol{n}}(\boldsymbol{r}_1)$ at $\boldsymbol{r}_2$ gives

$$\boldsymbol{\Psi}(\boldsymbol{r}_2) \cdot \hat{\boldsymbol{n}}(\boldsymbol{r}_1) = \boldsymbol{\Psi}(\boldsymbol{r}_2) \cdot \hat{\boldsymbol{n}}(\boldsymbol{r}_2) + \boldsymbol{\Psi}(\boldsymbol{r}_2) \cdot \left[\mathbf{C} \cdot (\boldsymbol{r}_2 - \boldsymbol{r}_1) \right]$$

as $\boldsymbol{r}_1 \to \boldsymbol{r}_2$ and the differential is

$$\mathbf{C} = \begin{pmatrix} \frac{\partial n_{\text{x}}(\boldsymbol{r}_1)}{\partial x'} & \frac{\partial n_{\text{x}}(\boldsymbol{r}_1)}{\partial y'} & \frac{\partial n_{\text{x}}(\boldsymbol{r}_1)}{\partial z'} \\ \frac{\partial n_{\text{y}}(\boldsymbol{r}_1)}{\partial x'} & \frac{\partial n_{\text{y}}(\boldsymbol{r}_1)}{\partial y'} & \frac{\partial n_{\text{y}}(\boldsymbol{r}_1)}{\partial z'} \\ \frac{\partial n_{\text{z}}(\boldsymbol{r}_1)}{\partial x'} & \frac{\partial n_{\text{z}}(\boldsymbol{r}_1)}{\partial y'} & \frac{\partial n_{\text{z}}(\boldsymbol{r}_1)}{\partial z'} \end{pmatrix} \Bigg|_{\boldsymbol{r}_1 = \boldsymbol{r}_2}$$

The first term is zero since the test function is tangential to the surface which gives $|\boldsymbol{\Psi}(\boldsymbol{r}_2) \cdot \hat{\boldsymbol{n}}(\boldsymbol{r}_1)| \leqslant K(\boldsymbol{r}_2 - \boldsymbol{r}_1)$ as $\boldsymbol{r}_1 \to \boldsymbol{r}_2$ and the singularity in the first term of the integral is removed.

To remove the singular part in the second term in (A.2), we show that $\nabla_1 g(\boldsymbol{r}_1, \boldsymbol{r}_2) \cdot \hat{\boldsymbol{n}}(\boldsymbol{r}_1) \leqslant K \frac{1}{|\boldsymbol{r}_2 - \boldsymbol{r}_1|}$ and thus integrable. This is true since

$$\frac{|\hat{\boldsymbol{n}}(\boldsymbol{r}_1) \cdot [\boldsymbol{r}_2 - \boldsymbol{r}_1]|}{|\boldsymbol{r}_2 - \boldsymbol{r}_1|^3} \leqslant \frac{L}{|\boldsymbol{r}_2 - \boldsymbol{r}_1|}$$

when $\boldsymbol{r}_1 \to \boldsymbol{r}_2$ and L is a positive constant [9].

Term 4:

$$\iint\limits_{S_{\text{rad}}} \boldsymbol{\Psi}^{\text{ort}}(\boldsymbol{r}_2) \cdot \boldsymbol{M}(\boldsymbol{r}_2) \, \mathrm{d}S_2 = - \iint\limits_{S_{\text{rad}}} \left[\hat{\boldsymbol{n}}(\boldsymbol{r}_2) \times \boldsymbol{\Psi}(\boldsymbol{r}_2) \right] \cdot \boldsymbol{M}(\boldsymbol{r}_2) \, \mathrm{d}S_2$$

This term does not contain any singularity.

Appendix B   Parametrization of the surface

The surface is parameterized by the azimuth angle φ and the height coordinate along the surface v, *i.e.*, the position vector $\boldsymbol{r}$ can be expressed as

$$\boldsymbol{r}(\varphi, v) = \rho(v) \cos \varphi \, \hat{\boldsymbol{e}}_{\text{x}} + \rho(v) \sin \varphi \, \hat{\boldsymbol{e}}_{\text{y}} + z(v) \, \hat{\boldsymbol{e}}_{\text{z}}$$

Evaluation of $|\boldsymbol{r}_2 - \boldsymbol{r}_1|$ in cylindrical coordinates give

$$|\boldsymbol{r}(\varphi_2, v_2) - \boldsymbol{r}(\varphi_1, v_1)| = \sqrt{C(v_1, v_2) - 2\rho(v_1)\rho(v_2) \cos(\varphi_1 - \varphi_2)} \tag{B.1}$$

where $C(v_1, v_2) = \rho^2(v_1) + \rho^2(v_2) + [z(v_2) - z(v_1)]^2$.

Normalized basis vectors, convenient for the problem, are

$$\begin{cases} \hat{\boldsymbol{\varphi}} = \dfrac{\partial \boldsymbol{r}}{\partial \varphi} \Big/ |\dfrac{\partial \boldsymbol{r}}{\partial \varphi}| = -\sin \varphi \, \hat{\boldsymbol{e}}_{\text{x}} + \cos \varphi \, \hat{\boldsymbol{e}}_{\text{y}} \\[2mm] \hat{\boldsymbol{v}} = \dfrac{\partial \boldsymbol{r}}{\partial v} \Big/ |\dfrac{\partial \boldsymbol{r}}{\partial v}| \end{cases}$$

where

$$h_\varphi(v) \equiv \left| \frac{\partial \boldsymbol{r}}{\partial \varphi} \right| = \rho(v) \qquad h_{\text{v}}(v) \equiv \left| \frac{\partial \boldsymbol{r}}{\partial v} \right| = \sqrt{\left(\frac{\partial \rho(v)}{\partial v} \right)^2 + \left(\frac{\partial z(v)}{\partial v} \right)^2}$$

The Jacobian is given by

$$\mathcal{J}(v) = \left| \frac{\partial \boldsymbol{r}}{\partial \varphi} \times \frac{\partial \boldsymbol{r}}{\partial v} \right| = \rho(v) \sqrt{\left(\frac{\partial \rho(v)}{\partial v} \right)^2 + \left(\frac{\partial z(v)}{\partial v} \right)^2} = h_\varphi(v) h_{\text{v}}(v)$$

and the differential area element is

$$\mathrm{d}S = \mathcal{J}(v) \, \mathrm{d}\varphi \, \mathrm{d}v = \rho(v) h_{\text{v}}(v) \, \mathrm{d}\varphi \, \mathrm{d}v$$

The normalized basis vectors of the coordinate system are explicitly

$$\hat{\boldsymbol{\varphi}}(\varphi) = \frac{1}{\rho(v)} \frac{\partial \boldsymbol{r}}{\partial \varphi} = -\sin \varphi \, \hat{\boldsymbol{e}}_{\text{x}} + \cos \varphi \, \hat{\boldsymbol{e}}_{\text{y}}$$

$$\hat{\boldsymbol{v}}(\varphi, v) = \frac{1}{h_{\text{v}}(v)} \frac{\partial \boldsymbol{r}}{\partial v} = \frac{1}{h_{\text{v}}(v)} \left\{ \rho'(v) \cos \varphi \, \hat{\boldsymbol{e}}_{\text{x}} + \rho'(v) \sin \varphi \, \hat{\boldsymbol{e}}_{\text{y}} + z'(v) \hat{\boldsymbol{e}}_{\text{z}} \right\} \tag{B.2}$$

$$\hat{\boldsymbol{n}}(\varphi, v) = \hat{\boldsymbol{\varphi}}(\varphi) \times \hat{\boldsymbol{v}}(\varphi, v) = \frac{1}{h_{\text{v}}(v)} \left\{ z'(v) \cos \varphi \, \hat{\boldsymbol{e}}_{\text{x}} + z'(v) \sin \varphi \, \hat{\boldsymbol{e}}_{\text{y}} - \rho'(v) \hat{\boldsymbol{e}}_{\text{z}} \right\}$$

and the scalar products between them are

$$\hat{\boldsymbol{\varphi}}(\varphi_1) \cdot \hat{\boldsymbol{\varphi}}(\varphi_2) = \cos(\varphi_1 - \varphi_2)$$

$$\hat{\boldsymbol{\varphi}}(\varphi_1) \cdot \hat{\boldsymbol{v}}(\varphi_2, v_2) = -\frac{\rho'(v_2)}{h_{\text{v}}(v_2)} \sin(\varphi_1 - \varphi_2)$$

$$\hat{\boldsymbol{v}}(\varphi_1, v_1) \cdot \hat{\boldsymbol{\varphi}}(\varphi_2) = \frac{\rho'(v_1)}{h_v(v_1)} \sin(\varphi_1 - \varphi_2)$$

$$\hat{\boldsymbol{v}}(\varphi_1, v_1) \cdot \hat{\boldsymbol{v}}(\varphi_2, v_2) = \frac{1}{h_v(v_1)h_v(v_2)} \left\{ \rho'(v_1)\rho'(v_2) \cos(\varphi_1 - \varphi_2) + z'(v_1)z'(v_2) \right\}$$

$$\hat{\boldsymbol{\varphi}}(\varphi_1) \cdot \hat{\boldsymbol{n}}(\varphi_2, v_2) = -\frac{z'(v_2)}{h_v(v_2)} \sin(\varphi_1 - \varphi_2)$$

$$\hat{\boldsymbol{n}}(\varphi_1, v_1) \cdot \hat{\boldsymbol{\varphi}}(\varphi_2) = \frac{z'(v_1)}{h_v(v_1)} \sin(\varphi_1 - \varphi_2)$$

$$\hat{\boldsymbol{v}}(\varphi_1, v_1) \cdot \hat{\boldsymbol{n}}(\varphi_2, v_2) = \frac{1}{h_v(v_1)h_v(v_2)} \left\{ \rho'(v_1)z'(v_2) \cos(\varphi_1 - \varphi_2) - z'(v_1)\rho'(v_2) \right\}$$

$$\hat{\boldsymbol{n}}(\varphi_1, v_1) \cdot \hat{\boldsymbol{v}}(\varphi_2, v_2) = \frac{1}{h_v(v_1)h_v(v_2)} \left\{ z'(v_1)\rho'(v_2) \cos(\varphi_1 - \varphi_2) - \rho'(v_1)z'(v_2) \right\}$$

The surface divergence for the parametrization and coordinate system described above is [16]

$$\nabla_S \cdot \boldsymbol{F}(\varphi, v) = \frac{1}{\mathcal{J}(v)} \left\{ h_v(v) \frac{\partial}{\partial \varphi} F_\varphi(\varphi, v) + \frac{\partial}{\partial v} \left[\rho(v) F_v(\varphi, v) \right] \right\} \qquad \text{(B.3)}$$

where $F_x = \boldsymbol{F} \cdot \hat{\boldsymbol{x}}$, $x = \varphi, v$. That is, the surface divergences of the tangential basis vectors in (B.2) are given by

$$\nabla_S \cdot \hat{\boldsymbol{\varphi}}(\varphi) = \frac{1}{\mathcal{J}(v)} \frac{\partial}{\partial \varphi} \left[h_v(v)1 \right] = 0$$

$$\nabla_S \cdot \hat{\boldsymbol{v}}(\varphi, v) = \frac{1}{\mathcal{J}(v)} \frac{\partial}{\partial v} \left[\rho(v)1 \right] = \frac{\rho'(v)}{\mathcal{J}(v)} \qquad \text{(B.4)}$$

The Green function is parametrized as, cf., (2.2),

$$g(\varphi_1 - \varphi_2, v_1, v_2) = \frac{1}{4\pi} \frac{e^{-jk\sqrt{C(v_1,v_2)-2\rho(v_1)\rho(v_2)\cos(\varphi_1-\varphi_2)}}}{\sqrt{C(v_1, v_2) - 2\rho(v_1)\rho(v_2) \cos(\varphi_1 - \varphi_2)}}$$

as is the gradient of the Green function

$$\nabla_1 g(\boldsymbol{r}_2, \boldsymbol{r}_1) = g(\boldsymbol{r}_2, \boldsymbol{r}_1) \left(1 + jk|\boldsymbol{r}_2 - \boldsymbol{r}_1| \right) \frac{\boldsymbol{r}_2 - \boldsymbol{r}_1}{|\boldsymbol{r}_2 - \boldsymbol{r}_1|^2}$$

$$= g(\varphi_1 - \varphi_2, v_1, v_2) D(\varphi_1 - \varphi_2, v_1, v_2)$$

$$\left\{ \left[\rho(v_2) \cos \varphi_2 - \rho(v_1) \cos \varphi_1 \right] \hat{\boldsymbol{e}}_x + \left[\rho(v_2) \sin \varphi_2 - \rho(v_1) \sin \varphi_1 \right] \hat{\boldsymbol{e}}_y \right.$$

$$\left. + \left[z(v_2) - z(v_1) \right] \hat{\boldsymbol{e}}_z \right\}$$

where we used the notation

$$\begin{cases} C(v_1, v_2) = \rho^2(v_1) + \rho^2(v_2) + [z(v_2) - z(v_1)]^2 \\ D(\varphi_1 - \varphi_2, v_1, v_2) = \dfrac{1 + jk\sqrt{C(v_1, v_2) - 2\rho(v_1)\rho(v_2) \cos(\varphi_1 - \varphi_2)}}{C(v_1, v_2) - 2\rho(v_1)\rho(v_2) \cos(\varphi_1 - \varphi_2)} \end{cases} \qquad \text{(B.5)}$$

In the coordinate system, $\{\hat{\boldsymbol{\varphi}}, \hat{\boldsymbol{v}}, \hat{\boldsymbol{n}}\}$ the components of $\nabla_1 g(\varphi_1 - \varphi_2, v_1, v_2)$ are

$$\nabla_1 g\Big|_{\hat{\boldsymbol{\varphi}}} = \hat{\boldsymbol{\varphi}}(\boldsymbol{r}_1) \cdot \nabla_1 g(\boldsymbol{r}_2, \boldsymbol{r}_1) = -gD\, \rho(v_2) \sin(\varphi_1 - \varphi_2)$$

$$\nabla_1 g\Big|_{\hat{\boldsymbol{v}}} = \hat{\boldsymbol{v}}(\boldsymbol{r}_1) \cdot \nabla_1 g(\boldsymbol{r}_2, \boldsymbol{r}_1)$$

$$= gD\left\{ \frac{\rho'(v_1)\rho(v_2)}{h_{\mathrm{v}}(v_1)} \cos(\varphi_1 - \varphi_2) - \frac{\rho'(v_1)\rho(v_1) - z'(v_1)\big[z(v_2) - z(v_1)\big]}{h_{\mathrm{v}}(v_1)} \right\}$$

$$\nabla_1 g\Big|_{\hat{\boldsymbol{n}}} = \hat{\boldsymbol{n}}(\boldsymbol{r}_1) \cdot \nabla_1 g(\boldsymbol{r}_2, \boldsymbol{r}_1)$$

$$= gD\left\{ \frac{z'(v_1)\rho(v_2)}{h_{\mathrm{v}}(v_1)} \cos(\varphi_1 - \varphi_2) - \frac{\rho(v_1)z'(v_1) + \rho'(v_1)\big[z(v_2) - z(v_1)\big]}{h_{\mathrm{v}}(v_1)} \right\}$$

$$\text{(B.6)}$$

The arguments of $\nabla_1 g(\varphi_1 - \varphi_2, v_1, v_2)$, $g(\varphi_1 - \varphi_2, v_1, v_2)$ and $D(\varphi_1 - \varphi_2, v_1, v_2)$ are suppressed for simplicity.

Appendix C   Expansion in basis functions

The test functions and the currents are expanded in the basis functions described in (2.7). The two test functions are chosen as

$$\begin{cases} \boldsymbol{\Psi}_{ni}^{\varphi} = (\boldsymbol{a}_{ni}^{\varphi})^* = f_i^{\varphi}(v)\, \mathrm{e}^{-\mathrm{j}n\varphi}\hat{\boldsymbol{\varphi}} \\ \boldsymbol{\Psi}_{ni}^{\mathrm{v}} = (\boldsymbol{a}_{ni}^{\mathrm{v}})^* = f_i^{\mathrm{v}}(v)\, \mathrm{e}^{-\mathrm{j}n\varphi}\hat{\boldsymbol{v}} \end{cases}$$

where the star denotes complex conjugation. This gives, *cf.*, (B.3),

$$\begin{cases} \nabla_{\mathrm{S}} \cdot \boldsymbol{\Psi}_{ni}^{\varphi} = -\mathrm{j}n\dfrac{f_i^{\varphi}(v)}{\rho(v)}\mathrm{e}^{-\mathrm{j}n\varphi} \\[2mm] \nabla_{\mathrm{S}} \cdot \boldsymbol{\Psi}_{ni}^{\mathrm{v}} = \dfrac{\mathrm{e}^{-\mathrm{j}n\varphi}}{\mathcal{J}(v)}\dfrac{\partial}{\partial v}\big[\rho(v) f_i^{\mathrm{v}}(v)\big] \end{cases}$$

and

$$\begin{cases} \hat{\boldsymbol{n}} \times \boldsymbol{\Psi}_{ni}^{\varphi} = f_i^{\varphi}(v)\, \mathrm{e}^{-\mathrm{j}n\varphi}\hat{\boldsymbol{v}} \\ \hat{\boldsymbol{n}} \times \boldsymbol{\Psi}_{ni}^{\mathrm{v}} = -f_i^{\mathrm{v}}(v)\, \mathrm{e}^{-\mathrm{j}n\varphi}\hat{\boldsymbol{\varphi}} \end{cases}$$

with the integer indices $i = 1, \ldots, N_{\mathrm{z}}$ and n.

The current $\boldsymbol{J}$ is expanded as

$$\boldsymbol{J} = \sum_{m,j} \left\{ J_{mj}^{\varphi}\, \boldsymbol{a}_{mj}^{\varphi} + J_{mj}^{\mathrm{v}}\, \boldsymbol{a}_{mj}^{\mathrm{v}+} \right\}$$

$$= \sum_{m,j} \left\{ J_{mj}^{\varphi}\, f_j^{\varphi}(v)\, \mathrm{e}^{\mathrm{j}m\varphi}\hat{\boldsymbol{\varphi}} + J_{mj}^{\mathrm{v}}\, f_j^{\mathrm{v}}(v)\, \mathrm{e}^{\mathrm{j}m\varphi}\hat{\boldsymbol{v}} \right\}$$

which gives, *cf.*, (B.3),

$$\nabla_{\mathrm{S}} \cdot \boldsymbol{J} = \sum_{m,j} \mathrm{e}^{\mathrm{j}m\varphi} \left\{ \mathrm{j}m\frac{f_j^{\varphi}(v)}{\rho(v)}J_{mj}^{\varphi} + \frac{1}{\mathcal{J}(v)}\frac{\partial}{\partial v}\big[\rho(v) f_j^{\mathrm{v}}(v)\big]\, J_{mj}^{\mathrm{v}} \right\}$$

and

$$\hat{\boldsymbol{n}} \times \boldsymbol{J} = \sum_{m,j} \left\{ J^\varphi_{mj} f^\varphi_j(v) \, \mathrm{e}^{\mathrm{j}m\varphi} \hat{\boldsymbol{v}} - J^\mathrm{v}_{mj} f^\mathrm{v}_j(v) \, \mathrm{e}^{\mathrm{j}m\varphi} \hat{\boldsymbol{\varphi}} \right\}$$

with the integer indices $j = 1, \ldots, N_z$ and m, and $J^{\varphi/\mathrm{v}}_{mj}$ denoting the expansion coefficients. The magnetic current $\boldsymbol{M}$ is expanded in a similar way with expansion coefficients M_{mj}.

C.1   Evaluation of a cross product

In this appendix the cross product in (2.9) is evaluated, *i.e.*,

$$\begin{aligned}
\nabla_1 g(\boldsymbol{r}_2, \boldsymbol{r}_1) &\times \boldsymbol{M}(\boldsymbol{r}_1) = g(\varphi_1 - \varphi_2, v_1, v_2) D(\varphi_1 - \varphi_2, v_1, v_2) \\
&\cdot \Bigg(\Bigg\{ \Bigg[\frac{z'(v_1)\rho(v_2)}{h_\mathrm{v}(v_1)} \cos(\varphi_1 - \varphi_2) - \frac{\rho(v_1)z'(v_1) + \rho'(v_1)\big[z(v_2) - z(v_1)\big]}{h_\mathrm{v}(v_1)} \Bigg] \hat{\boldsymbol{v}}(\varphi_1, v_1) \\
&\quad + \Bigg[-\frac{\rho'(v_1)\rho(v_2)}{h_\mathrm{v}(v_1)} \cos(\varphi_1 + \varphi_2) + \frac{\rho'(v_1)\rho(v_1) - z'(v_1)\big[z(v_2) - z(v_1)\big]}{h_\mathrm{v}(v_1)} \Bigg] \hat{\boldsymbol{n}}(\varphi_1, v_1) \Bigg\} \\
&\quad \cdot \sum_{m,j} M^\varphi_{mj} f^\varphi_j(v_1) \, \mathrm{e}^{\mathrm{j}m\varphi_1} \\
&\quad + \Bigg\{ \Bigg[-\frac{z'(v_1)\rho(v_2)}{h_\mathrm{v}(v_1)} \cos(\varphi_1 - \varphi_2) + \frac{\rho(v_1)z'(v_1) + \rho'(v_1)\big[z(v_2) - z(v_1)\big]}{h_\mathrm{v}(v_1)} \Bigg] \hat{\boldsymbol{\varphi}}(\varphi_1) \\
&\quad - \rho(v_2) \sin(\varphi_1 - \varphi_2) \hat{\boldsymbol{n}}(\varphi_1, v_1) \Bigg\} \cdot \sum_{m,j} M^\mathrm{v}_{mj} f^\mathrm{v}_j(v_1) \, \mathrm{e}^{\mathrm{j}m\varphi_1} \Bigg)
\end{aligned}$$

$$\text{(C.1)}$$

where (2.8) and (B.6) are used. The function $D(\varphi_1 - \varphi_2, v_1, v_2)$ is labeled in (B.5).

Appendix D   Integration over φ

The integration in the angular direction of (2.6) and (2.9) is investigated in detail. Nine different integrals $I_\mathrm{a/A} - I_\mathrm{i/I}$ appear. The integrals from (2.6) and (2.9) have the same form, but the ones in (2.6) contain singularities and are denoted by upper-case indices. One of the integrals is studied in detail, while the others are listed at the end of this section. The cross product in (2.6) and (2.9) is evaluated separately in Appendix C.1.

The relevant integral is

$$I_\mathrm{b} = \int\limits_0^{2\pi}\int\limits_0^{2\pi} g(\varphi_1 - \varphi_2, v_1, v_2) \mathrm{e}^{-\mathrm{j}n\varphi_2} \mathrm{e}^{\mathrm{j}m\varphi_1} \cos(\varphi_1 - \varphi_2) \, \mathrm{d}\varphi_1 \, \mathrm{d}\varphi_2$$

A change of variable, $\varphi_1 = \varphi_2 + \phi$, gives

$$I_\mathrm{b} = \int\limits_0^{2\pi} g(\phi, v_1, v_2) \mathrm{e}^{\mathrm{j}m\phi} \cos(\phi) \int\limits_0^{2\pi} \mathrm{e}^{\mathrm{j}(m-n)\varphi_2} \, \mathrm{d}\varphi_2 \, \mathrm{d}\phi$$

The inner integral is zero if $m \neq n$. Therefore, the only interesting case is $n = m$, giving

$$I_b = 2\pi \int_0^{2\pi} g(\phi, v_1, v_2) \left[\cos(m\phi) + \mathrm{j}\sin(m\phi)\right] \cos(\phi) \,\mathrm{d}\phi$$

$$= 4\pi \int_0^\pi g(\phi, v_1, v_2) \cos(m\phi) \cos(\phi) \,\mathrm{d}\phi$$

$$= 2\pi \int_0^\pi g(\phi, v_1, v_2) \cos([m-1]\phi) \,\mathrm{d}\phi + 2\pi \int_0^\pi g(\phi, v_1, v_2) \cos([m+1]\phi) \cos \,\mathrm{d}\phi$$

using that $g(\phi, v_1, v_2)$ is an even function in ϕ.

The rest of the integrals in the angular direction of (2.9) are derived in the same manner and listed below.

$$I_a = \int_0^{2\pi}\int_0^{2\pi} g(\varphi_1 - \varphi_2, v_1, v_2) e^{\mathrm{j}m(\varphi_1 - \varphi_2)} \,\mathrm{d}\varphi_1 \,\mathrm{d}\varphi_2 = 4\pi \int_0^\pi g(\phi, v_1, v_2) \cos(m\phi) \,\mathrm{d}\phi$$

$$= 4\pi \, G_m(v_1, v_2)$$

$$I_b = \int_0^{2\pi}\int_0^{2\pi} g(\varphi_1 - \varphi_2, v_1, v_2) e^{\mathrm{j}m(\varphi_1 - \varphi_2)} \cos(\varphi_1 - \varphi_2) \,\mathrm{d}\varphi_1 \,\mathrm{d}\varphi_2$$

$$= 4\pi \int_0^\pi g(\phi, v_1, v_2) \cos(m\phi) \cos(\phi) \,\mathrm{d}\phi = 2\pi \left[G_{m-1}(v_1, v_2) + G_{m+1}(v_1, v_2)\right]$$

$$I_c = \int_0^{2\pi}\int_0^{2\pi} g(\varphi_1 - \varphi_2, v_1, v_2) e^{\mathrm{j}m(\varphi_1 - \varphi_2)} \sin(\varphi_1 - \varphi_2) \,\mathrm{d}\varphi_1 \,\mathrm{d}\varphi_2$$

$$= 4\pi\mathrm{j} \int_0^\pi g(\phi, v_1, v_2) \sin(m\phi) \sin(\phi) \,\mathrm{d}\phi = 2\pi\mathrm{j} \left[G_{m-1}(v_1, v_2) - G_{m+1}(v_1, v_2)\right]$$

$$I_d = \int_0^{2\pi}\int_0^{2\pi} g(\varphi_1 - \varphi_2, v_1, v_2) D(\varphi_1 - \varphi_2, v_1, v_2) e^{\mathrm{j}m(\varphi_1 - \varphi_2)} \,\mathrm{d}\varphi_1 \,\mathrm{d}\varphi_2$$

$$= 4\pi \int_0^\pi g(\phi, v_1, v_2) D(\phi, v_1, v_2) \cos(m\phi) \,\mathrm{d}\phi = 4\pi \, \mathcal{G}_m(v_1, v_2)$$

$$I_e = \int_0^{2\pi}\int_0^{2\pi} g(\varphi_1 - \varphi_2, v_1, v_2) D(\varphi_1 - \varphi_2, v_1, v_2) e^{\mathrm{j}m(\varphi_1 - \varphi_2)} \cos(\varphi_1 - \varphi_2) \,\mathrm{d}\varphi_1 \,\mathrm{d}\varphi_2$$

$$= 4\pi \int_0^\pi g(\phi, v_1, v_2) D(\phi, v_1, v_2) \cos(m\phi) \cos(\phi) \,\mathrm{d}\phi$$

$$= 2\pi\big[\mathcal{G}_{m-1}(v_1, v_2) + \mathcal{G}_{m+1}(v_1, v_2)\big]$$

$$I_f = \int\limits_0^{2\pi}\int\limits_0^{2\pi} g(\varphi_1 - \varphi_2, v_1, v_2)D(\varphi_1 - \varphi_2, v_1, v_2)\mathrm{e}^{\mathrm{j}m(\varphi_1-\varphi_2)}\sin(\varphi_1 - \varphi_2)\,\mathrm{d}\varphi_1\,\mathrm{d}\varphi_2$$

$$= 4\pi\mathrm{j}\int\limits_0^{\pi} g(\phi, v_1, v_2)D(\phi, v_1, v_2)\sin(m\phi)\sin(\phi)\,\mathrm{d}\phi$$

$$= 2\pi\mathrm{j}\big[\mathcal{G}_{m-1}(v_1, v_2) - \mathcal{G}_{m+1}(v_1, v_2)\big]$$

$$I_g = \int\limits_0^{2\pi}\int\limits_0^{2\pi} g(\varphi_1 - \varphi_2, v_1, v_2)D(\varphi_1 - \varphi_2, v_1, v_2)\mathrm{e}^{\mathrm{j}m(\varphi_1-\varphi_2)}\cos(\varphi_1 - \varphi_2)$$

$$\cdot \sin(\varphi_1 - \varphi_2)\,\mathrm{d}\varphi_1\,\mathrm{d}\varphi_2$$

$$= 2\pi\mathrm{j}\int\limits_0^{\pi} g(\phi, v_1, v_2)D(\phi, v_1, v_2)\sin(m\phi)\sin(2\phi)\,\mathrm{d}\phi$$

$$= \pi\mathrm{j}\big[\mathcal{G}_{m-2}(v_1, v_2) - \mathcal{G}_{m+2}(v_1, v_2)\big]$$

$$I_h = \int\limits_0^{2\pi}\int\limits_0^{2\pi} g(\varphi_1 - \varphi_2, v_1, v_2)D(\varphi_1 - \varphi_2, v_1, v_2)\mathrm{e}^{\mathrm{j}m(\varphi_1-\varphi_2)}\cos^2(\varphi_1 - \varphi_2)\,\mathrm{d}\varphi_1\,\mathrm{d}\varphi_2$$

$$= 2\pi\int\limits_0^{\pi} g(\phi, v_1, v_2)D(\phi, v_1, v_2)\cos(m\phi)\big[1 + \cos(2\phi)\big]\,\mathrm{d}\phi$$

$$= 2\pi\mathcal{G}_m(v_1, v_2) + \pi\big[\mathcal{G}_{m-2}(v_1, v_2) + \mathcal{G}_{m+2}(v_1, v_2)\big]$$

$$I_i = \int\limits_0^{2\pi}\int\limits_0^{2\pi} g(\varphi_1 - \varphi_2, v_1, v_2)D(\varphi_1 - \varphi_2, v_1, v_2)\mathrm{e}^{\mathrm{j}m(\varphi_1-\varphi_2)}\sin^2(\varphi_1 - \varphi_2)\,\mathrm{d}\varphi_1\,\mathrm{d}\varphi_2$$

$$= 2\pi\int\limits_0^{\pi} g(\phi, v_1, v_2)D(\phi, v_1, v_2)\cos(m\phi)\big[1 - \cos(2\phi)\big]\,\mathrm{d}\phi$$

$$= 2\pi\mathcal{G}_m(v_1, v_2) - \pi\big[\mathcal{G}_{m-2}(v_1, v_2) + \mathcal{G}_{m+2}(v_1, v_2)\big]$$

The new Green functions are defined as

$$G_m(v_1, v_2) = \int\limits_0^{\pi} g(\phi, v_1, v_2)\cos(m\phi)\,\mathrm{d}\phi$$

$$\mathcal{G}_m(v_1, v_2) = \int\limits_0^{\pi} g(\phi, v_1, v_2)D(\phi, v_1, v_2)\cos(m\phi)\,\mathrm{d}\phi$$

(D.1)

where $\phi = \varphi_1 - \varphi_2$, the function D is defined in (B.5), and m is an integer index. Observe that these Green functions are not singular as $\boldsymbol{r}_1$ and $\boldsymbol{r}_2$ are always different.

The angular integrals of (2.6), $I_A - I_I$, have the same appearance as $I_a - I_i$. However, the Green functions contain singularities and are denoted by $g_m(v_1, v_2)$

and $\mathfrak{g}_m(v_1, v_2)$. The numerical treatment of these singularities is addressed in Appendix E.

Appendix E   Singularities in the Greens functions

Two new Greens functions, *i.e.*,

$$
\begin{cases}
g_m(v_1, v_2) = \int\limits_0^\pi g(\phi, v_1, v_2)\, \cos(m\phi)\, \mathrm{d}\phi \\[3em]
\mathfrak{g}_m(v_1, v_2) = \int\limits_0^\pi g(\phi, v_1, v_2) D(\phi, v_1, v_2)\, \cos(m\phi)\, \mathrm{d}\phi
\end{cases}
$$

are defined in the derivation of the integral equation (2.6), where $g(\phi, v_1, v_2)$ is defined in (2.2), $D(\phi, v_1, v_2)$ in (B.5), and m is an integer index. These Green functions contain singularities. In this appendix, one way of handling these singularities is shown.

Integrals containing g_m have the form $\iint f(v_1, v_2) g_m(v_1, v_2)\, \mathrm{d}v_1\, \mathrm{d}v_2$. The integrand $g_m(v_1, v_2)$ has a logarithmic singularity, *i.e.*, $g_m(v_1, v_2) \sim \ln|v_1 - v_2|$, *i.e.*, the integral is of the type [6]

$$
\int_a^b f(x) \ln x\, \mathrm{d}x
$$

Changing variables $x = y^2$ gives an integral where the singularity is removed, *i.e.*,

$$
\int_{\sqrt{a}}^{\sqrt{b}} f(y^2) \ln y^2\ 2y\, \mathrm{d}y
$$

The second Green function contains a singularity of the third order, *i.e.*,

$$
\mathfrak{g}_m(v_1, v_2) = \int g(\phi, v_1, v_2) D(\phi, v_1, v_2) \cos(m\phi)\, \mathrm{d}\phi = \int \frac{\mathrm{e}^{-\mathrm{j}kR}\big[1 + \mathrm{j}kR\big]}{4\pi R^3} \cos(m\phi)\, \mathrm{d}\phi
$$

where $R = |\boldsymbol{r_2} - \boldsymbol{r_1}|$. This Green function occurs in two different combinations, either as

$$
\mathfrak{g}_{m-1}(v_1, v_2) - \mathfrak{g}_{m+1}(v_1, v_2)
$$

or

$$
f(v_1, v_2)\, \mathfrak{g}_m(v_1, v_2) + h(v_1, v_2)\big[\mathfrak{g}_{m-1}(v_1, v_2) + \mathfrak{g}_{m+1}(v_1, v_2)\big]
$$

The first combination can be rewritten as

$$\mathfrak{g}_{m-1}\left(v_1, v_2\right) - \mathfrak{g}_{m+1}(v_1, v_2) = 2\int_0^\pi g(\phi, v_1, v_2) D(\phi, v_1, v_2) \sin(m\phi)\sin(\phi)\,\mathrm{d}\phi$$

$$= \frac{1}{2\pi}\int_0^\pi \left\{\frac{\mathrm{e}^{-\mathrm{j}kR}}{R} + \mathrm{j}k\,\mathrm{e}^{-\mathrm{j}kR}\right\}\underbrace{\frac{\sin(m\phi)\sin(\phi)}{R^2}}_{\text{singularity removed}}\,\mathrm{d}\phi$$

$$= \frac{1}{2\pi}\int_0^\pi \left\{\underbrace{\frac{\mathrm{e}^{-\mathrm{j}kR}-1}{R}}_{\text{singularity removed}} + \underbrace{\frac{1}{R}}_{\text{analytically solved}} + \mathrm{j}k\,\mathrm{e}^{-\mathrm{j}kR}\right\}\frac{\sin(m\phi)\sin(\phi)}{R^2}\,\mathrm{d}\phi$$

That is, the singularities are removed.

The second combination is rewritten as

$$f(v_1, v_2)\,\mathfrak{g}_m\left(v_1, v_2\right) + h(v_1, v_2)\left[\mathfrak{g}_{m-1}(v_1, v_2) + \mathfrak{g}_{m+1}(v_1, v_2)\right]$$

$$= \int_0^\pi g(\phi, v_1, v_2) D(\phi, v_1, v_2)\Big[f(v_1, v_2) + h(v_1, v_2)\cos(\phi)\Big]\cos(m\phi)\,\mathrm{d}\phi$$

$$= \int_0^\pi \frac{1}{4\pi}\left\{\underbrace{\frac{\mathrm{e}^{-\mathrm{j}kR}-1}{R}}_{\text{singularity removed}} + \underbrace{\frac{1}{R}}_{\text{analytically solved}} + \mathrm{j}k\,\mathrm{e}^{-\mathrm{j}kR}\right\}$$

$$\cdot\Big[f(v_1, v_2) + h(v_1, v_2)\cos(\phi)\Big]\left[\frac{1}{R^2} - 2\,\underbrace{\frac{\sin^2\left(\frac{m\phi}{2}\right)}{R^2}}_{\text{singularity removed}}\right]\mathrm{d}\phi$$

Continuing with the term that still contains a singularity gives

$$\int_0^\pi \frac{1}{4\pi}\left\{\frac{\mathrm{e}^{-\mathrm{j}kR}-1}{R} + \frac{1}{R} + \mathrm{j}k\,\mathrm{e}^{-\mathrm{j}kR}\right\}\Big[f(v_1, v_2) + h(v_1, v_2)\cos(\phi)\Big]\frac{1}{R^2}\,\mathrm{d}\phi$$

$$= \int_0^\pi \frac{1}{4\pi}\left\{\frac{\mathrm{e}^{-\mathrm{j}kR}-1}{R} + \frac{1}{R} + \mathrm{j}k\,\mathrm{e}^{-\mathrm{j}kR}\right\}\left[\frac{f(v_1, v_2)}{R^2} + \frac{h(v_1, v_2)}{R^2} - \underbrace{2h(v_1, v_2)\frac{\sin^2\left(\frac{\phi}{2}\right)}{R^2}}_{\text{singularity removed}}\right]\mathrm{d}\phi$$

This means that the only term where the singularities are not removed so far is $\int_0^\pi g(\phi, v_1, v_2) D(\phi, v_1, v_2)[f(v_1, v_2) + h(v_1, v_2)]\,\mathrm{d}\phi$. To remove this last singularity we investigate the triple integral, *i.e.*, $\iiint \ldots \mathrm{d}\phi\,\mathrm{d}v_1\,\mathrm{d}v_2$ instead of performing the integrations over ϕ and v separately. The actual expressions of the terms containing

this last singularity are,*cf.*, Appendix G,

$$
\begin{cases}
\displaystyle\iint -\rho(v_1)z'(v_2)\,\mathfrak{g}_m\,(v_1,v_2) \\
\qquad + \Big[\rho(v_2)z'(v_2) - \rho'(v_2)[z(v_2)-z(v_1)]\Big]\dfrac{\mathfrak{g}_{m-1}(v_1,v_2) + \mathfrak{g}_{m+1}(v_1,v_2)}{2}\ \mathrm{d}v_1\,\mathrm{d}v_2 \\[4mm]
\displaystyle\iint -z'(v_1)\rho(v_2)\,\mathfrak{g}_m\,(v_1,v_2) \\
\qquad + \Big[\rho(v_1)z'(v_1) + \rho'(v_1)[z(v_2)-z(v_1)]\Big]\dfrac{\mathfrak{g}_{m-1}(v_1,v_2) + \mathfrak{g}_{m+1}(v_1,v_2)}{2}\ \mathrm{d}v_1\,\mathrm{d}v_2
\end{cases}
$$

Both integrals are treated in the same way, *i.e.*, only the first one is investigated in detail. Only the part of the Green functions containing the singularity is investigated

$$
\int\!\!\!\int\!\!\!\int_0^\pi -\rho(v_1)z'(v_2)g(\phi,v_1,v_2)D(\phi,v_1,v_2)
$$
$$
\qquad + \Big[\rho(v_2)z'(v_2) - \rho'(v_2)[z(v_2)-z(v_1)]\Big]g(\phi,v_1,v_2)D(\phi,v_1,v_2)\ \mathrm{d}\phi\,\mathrm{d}v_1\,\mathrm{d}v_2
$$
$$
= \int\!\!\!\int\!\!\!\int_0^\pi \Big[z'(v_2)[\rho(v_2)-\rho(v_1)] - \rho'(v_2)[z(v_2)-z(v_1)]\Big]\frac{\mathrm{e}^{-\mathrm{j}kR}\big[1+\mathrm{j}kR\big]}{4\pi R^3}\ \mathrm{d}\phi\,\mathrm{d}v_1\,\mathrm{d}v_2
$$
$$
\tag{E.1}
$$

Now, both $\rho(v_1)$ and $z(v_1)$ are expanded in its Taylor series about $v_1 = v_2$.

$$
\rho(v_1) = \rho(v_2) + \rho'(v_2)(v_1-v_2) + \frac{\rho''(v_2)}{2}(v_1-v_2)^2 + \mathcal{O}((v_1-v_2)^3)
$$
$$
z(v_1) = z(v_2) + z'(v_2)(v_1-v_2) + \frac{z''(v_2)}{2}(v_1-v_2)^2 + \mathcal{O}((v_1-v_2)^3)
$$

That is, in the vicinity of v_2, (E.1) can be written as

$$
\int\!\!\!\int\!\!\!\int_0^\pi \Big[z'(v_2)[-\rho'(v_2)(v_1-v_2) - \frac{\rho''(v_2)}{2}(v_1-v_2)^2]
$$
$$
\qquad - \rho'(v_2)[-z'(v_2)(v_1-v_2) - \frac{z''(v_2)}{2}(v_1-v_2)^2]\Big]\frac{\mathrm{e}^{-\mathrm{j}kR}\big[1+\mathrm{j}kR\big]}{4\pi R^3}\ \mathrm{d}\phi\,\mathrm{d}v_1\,\mathrm{d}v_2
$$
$$
= \frac{1}{2}\int\!\!\!\int\!\!\!\int_0^\pi \Big[-z'(v_2)\rho''(v_2) + \rho'(v_2)z''(v_2)\Big](v_1-v_2)^2\frac{\mathrm{e}^{-\mathrm{j}kR}\big[1+\mathrm{j}kR\big]}{4\pi R^3}\ \mathrm{d}\phi\,\mathrm{d}v_1\,\mathrm{d}v_2
$$
$$
= \frac{1}{8\pi}\int\!\!\!\int\!\!\!\int_0^\pi \Big[-z'(v_2)\rho''(v_2) + \rho'(v_2)z''(v_2)\Big]\underbrace{\frac{(v_1-v_2)^2}{R^2}}_{\text{singularity removed}}
$$
$$
\cdot \Big\{\underbrace{\frac{\mathrm{e}^{-\mathrm{j}kR}-1}{R}}_{\text{singularity removed}} + \underbrace{\frac{1}{R}}_{\text{analytically solved}} + \mathrm{j}k\,\mathrm{e}^{-\mathrm{j}kR}\Big\}\ \mathrm{d}\phi\,\mathrm{d}v_1\,\mathrm{d}v_2
$$

and all the singularities are removed.

Appendix F   Matrix formulation of the integral representation

In this section equation (2.9), *i.e.*,

$$
\begin{bmatrix} \hat{\boldsymbol{v}} \\ \hat{\boldsymbol{\varphi}} \end{bmatrix} \cdot \left\{ -\mathrm{j}\omega\mu_0 \iint\limits_{S_{\mathrm{rad}}} g(\boldsymbol{r}_1,\boldsymbol{r}_2)\boldsymbol{J}(\boldsymbol{r}_1)\,\mathrm{d}S_1 + \mathrm{j}\frac{1}{\omega\epsilon_0} \iint\limits_{S_{\mathrm{rad}}} \nabla_1 g(\boldsymbol{r}_1,\boldsymbol{r}_2)\big[\nabla_{1S}\cdot\boldsymbol{J}(\boldsymbol{r}_1)\big]\,\mathrm{d}S_1 \right.
$$

$$
\left. + \iint\limits_{S_{\mathrm{rad}}} \nabla_1 g(\boldsymbol{r}_1,\boldsymbol{r}_2)\times\boldsymbol{M}(\boldsymbol{r}_1)\,\mathrm{d}S_1 \right\} = \begin{bmatrix} \hat{\boldsymbol{v}}\cdot\boldsymbol{E}(\boldsymbol{r}_2) \\ \hat{\boldsymbol{\varphi}}\cdot\boldsymbol{E}(\boldsymbol{r}_2) \end{bmatrix} = \begin{bmatrix} E^{\mathrm{v}}(\varphi_2,v_2) \\ E^{\varphi}(\varphi_2,v_2) \end{bmatrix} \qquad \boldsymbol{r}_2\in S_{\mathrm{meas}}
$$

$$
\Longleftrightarrow
$$

$$
-\mathrm{j}\omega\mu_0\,I_1 + \mathrm{j}\frac{1}{\omega\epsilon_0}\,I_2 + I_3 = E
$$

is rewritten into a system of matrices. Start by writing I_1, I_2 and I_3 as

$$
(I_1)_{ij} = Z^{11\mathrm{a}}_{ij}J^{\mathrm{v}}_j + Z^{12\mathrm{a}}_{ij}J^{\varphi}_j
$$
$$
(I_2)_{ij} = Z^{11\mathrm{b}}_{ij}J^{\mathrm{v}}_j + Z^{12\mathrm{b}}_{ij}J^{\varphi}_j
$$
$$
(I_3)_{ij} = X^{11}_{ij}M^{\mathrm{v}}_j + X^{12}_{ij}M^{\varphi}_j
$$

for the $\hat{\boldsymbol{v}}$-component and

$$
(I_1)_{ij} = Z^{21\mathrm{a}}_{ij}J^{\mathrm{v}}_j + Z^{22\mathrm{a}}_{ij}J^{\varphi}_j
$$
$$
(I_2)_{ij} = Z^{21\mathrm{b}}_{ij}J^{\mathrm{v}}_j + Z^{22\mathrm{b}}_{ij}J^{\varphi}_j
$$
$$
(I_3)_{ij} = X^{21}_{ij}M^{\mathrm{v}}_j + X^{22}_{ij}M^{\varphi}_j
$$

for the $\hat{\boldsymbol{\varphi}}$-component. The indices are $j = 1,\dots,J$, where $J = N_{\mathrm{z}}$ and $i = 1,\dots,I$, where $I = N_{\mathrm{z}}^{\mathrm{meas}}$. This gives the matrix system,

$$
-\mathrm{j}\omega\mu_0\,[I_1] + \frac{\mathrm{j}}{\omega\epsilon_0}\,[I_2] + [I_3] =
$$

$$
\begin{bmatrix} -\mathrm{j}\omega\mu_0\,[Z^{11\mathrm{a}}] + \frac{\mathrm{j}}{\omega\epsilon_0}\,[Z^{11\mathrm{b}}] & -\mathrm{j}\omega\mu_0\,[Z^{12\mathrm{a}}] + \frac{\mathrm{j}}{\omega\epsilon_0}\,[Z^{12\mathrm{b}}] \\ -\mathrm{j}\omega\mu_0\,[Z^{21\mathrm{a}}] + \frac{\mathrm{j}}{\omega\epsilon_0}\,[Z^{21\mathrm{b}}] & -\mathrm{j}\omega\mu_0\,[Z^{22\mathrm{a}}] + \frac{\mathrm{j}}{\omega\epsilon_0}\,[Z^{22\mathrm{b}}] \end{bmatrix} \begin{bmatrix} [J^{\mathrm{v}}] \\ [J^{\varphi}] \end{bmatrix}
$$

$$
+ \begin{bmatrix} [X^{11}] & [X^{12}] \\ [X^{21}] & [X^{22}] \end{bmatrix} \begin{bmatrix} [M^{\mathrm{v}}] \\ [M^{\varphi}] \end{bmatrix} = \begin{bmatrix} [E^{\mathrm{v}}] \\ [E^{\varphi}] \end{bmatrix}
$$

$$
\Longleftrightarrow
$$

$$
\begin{bmatrix} [Z^{11}] & [Z^{12}] \\ [Z^{21}] & [Z^{22}] \end{bmatrix} \begin{bmatrix} [J^{\mathrm{v}}] \\ [J^{\varphi}] \end{bmatrix} + \begin{bmatrix} [X^{11}] & [X^{12}] \\ [X^{21}] & [X^{22}] \end{bmatrix} \begin{bmatrix} [M^{\mathrm{v}}] \\ [M^{\varphi}] \end{bmatrix} = \begin{bmatrix} [E^{\mathrm{v}}] \\ [E^{\varphi}] \end{bmatrix} \qquad \text{(F.1)}
$$

for all m. Expressions for the matrix elements $[Z^{kl}]$ and $[X^{kl}]$ are derived in the next section.

F.1　The impedance matrices

For a given value of the index m, the impedance matrices in (F.1) are given by
$Z_{ij}^{11} = -\mathrm{j}\omega\mu_0 Z_{ij}^{11\mathrm{a}} + \frac{\mathrm{j}}{\omega\epsilon_0} Z_{ij}^{11\mathrm{b}}$ where

$$
\begin{cases}
Z_{ij}^{11\mathrm{a}} = \dfrac{1}{h_\mathrm{v}(v_2)} \int f_j^\mathrm{v}(v_1)\rho(v_1)\Big\{\rho'(v_1)\rho'(v_2)I_\mathrm{b} + z'(v_1)z'(v_2)I_\mathrm{a}\Big\}\,\mathrm{d}v_1 \\[2mm]
\qquad = 2\int f_j^\mathrm{v}(v_1)\rho(v_1)z'(v_1)G_m(v_1,v_2)\,\mathrm{d}v_1 \\[2mm]
Z_{ij}^{11\mathrm{b}} = \dfrac{1}{h_\mathrm{v}(v_2)} \int \dfrac{\partial}{\partial v_1}\big[\rho(v_1)f_j^\mathrm{v}(v_1)\big]\Big\{\rho'(v_2)\rho(v_2)I_\mathrm{i} + \rho'(v_2)\rho(v_2)I_\mathrm{h} \\[2mm]
\qquad\qquad + z'(v_2)[z(v_2) - z(v_1)]I_\mathrm{d} - \rho(v_1)\rho'(v_2)I_\mathrm{e}\Big\}\,\mathrm{d}v_1 \\[2mm]
\qquad = 2\int \dfrac{\partial}{\partial v_1}\big[\rho(v_1)f_j^\mathrm{v}(v_1)\big]\big[z(v_2) - z(v_1)\big]\mathcal{G}_m(v_1,v_2)\,\mathrm{d}v_1
\end{cases}
$$

and $Z_{ij}^{12} = -\mathrm{j}\omega\mu_0 Z_{ij}^{12\mathrm{a}} + \frac{\mathrm{j}}{\omega\epsilon_0} Z_{ij}^{12\mathrm{b}}$ where

$$
\begin{cases}
Z_{ij}^{12\mathrm{a}} = -\dfrac{\rho'(v_2)}{h_\mathrm{v}(v_2)} \int f_j^\varphi(v_1)h_\mathrm{v}(v_1)\rho(v_1)I_\mathrm{c}\,\mathrm{d}v_1 = 0 \\[2mm]
Z_{ij}^{12\mathrm{b}} = \mathrm{j}\dfrac{m}{h_\mathrm{v}(v_2)} \int f_j^\varphi(v_1)h_\mathrm{v}(v_1)\Big\{\rho'(v_2)\rho(v_2)I_\mathrm{i} + \rho'(v_2)\rho(v_2)I_\mathrm{h} \\[2mm]
\qquad\qquad + z'(v_2)\big[z(v_2) - z(v_1)\big]I_\mathrm{d} - \rho(v_1)\rho'(v_2)I_\mathrm{e}\Big\}\,\mathrm{d}v_1 \\[2mm]
\qquad = 2\mathrm{j}\,m \int f_j^\varphi(v_1)h_\mathrm{v}(v_1)\big[z(v_2) - z(v_1)\big]\mathcal{G}_m(v_1,v_2)\,\mathrm{d}v_1
\end{cases}
$$

and $Z_{ij}^{21} = -\mathrm{j}\omega\mu_0 Z_{ij}^{21\mathrm{a}} + \frac{\mathrm{j}}{\omega\epsilon_0} Z_{ij}^{21\mathrm{b}}$ where

$$
\begin{cases}
Z_{ij}^{21\mathrm{a}} = \int f_j^\mathrm{v}(v_1)\rho(v_1)\rho'(v_1)I_\mathrm{c}\,\mathrm{d}v_1 \\[2mm]
\qquad = \mathrm{j}\int f_j^\mathrm{v}(v_1)\rho(v_1)\rho'(v_1)\big[G_{m-1}(v_1,v_2) - G_{m+1}(v_1,v_2)\big]\,\mathrm{d}v_1 \\[2mm]
Z_{ij}^{21\mathrm{b}} = \int \rho(v_1)\dfrac{\partial}{\partial v_1}\big[\rho(v_1)f_j^\mathrm{v}(v_1)\big]I_\mathrm{f}\,\mathrm{d}v_1 \\[2mm]
\qquad = \mathrm{j}\int \rho(v_1)\dfrac{\partial}{\partial v_1}\big[\rho(v_1)f_j^\mathrm{v}(v_1)\big]\big[\mathcal{G}_{m-1}(v_1,v_2) - \mathcal{G}_{m+1}(v_1,v_2)\big]\,\mathrm{d}v_1
\end{cases}
$$

and $Z_{ij}^{22} = -\mathrm{j}\omega\mu_0 Z_{ij}^{22\mathrm{a}} + \frac{\mathrm{j}}{\omega\epsilon_0} Z_{ij}^{22\mathrm{b}}$ where

$$
\begin{cases}
Z_{ij}^{22\mathrm{a}} = \int f_j^\varphi(v_1)h_\mathrm{v}(v_1)\rho(v_1)I_\mathrm{b}\,\mathrm{d}v_1 \\[2mm]
\qquad = \int f_j^\varphi(v_1)h_\mathrm{v}(v_1)\rho(v_1)\big[G_{m-1}(v_1,v_2) + G_{m+1}(v_1,v_2)\big]\,\mathrm{d}v_1 \\[2mm]
Z_{ij}^{22\mathrm{b}} = \mathrm{j}\,m \int f_j^\varphi(v_1)\rho(v_1)h_\mathrm{v}(v_1)I_\mathrm{f}\,\mathrm{d}v_1 \\[2mm]
\qquad = -m \int f_j^\varphi(v_1)\rho(v_1)h_\mathrm{v}(v_1)\big[\mathcal{G}_{m-1}(v_1,v_2) - \mathcal{G}_{m+1}(v_1,v_2)\big]\,\mathrm{d}v_1
\end{cases}
$$

and

$$X_{ij}^{11} = \int f_j^{\mathrm{v}}(v_1) \frac{\rho(v_1)}{h_{\mathrm{v}}(v_2)}$$
$$\cdot \Big[-\rho(v_1)z'(v_1)\rho'(v_2) - \rho'(v_1)\rho'(v_2)\big[z(v_2) - z(v_1)\big]$$
$$+ \rho'(v_1)\rho(v_2)z'(v_2) \Big] I_{\mathrm{f}} \; \mathrm{d}v_1$$
$$= \mathrm{j} \int f_j^{\mathrm{v}}(v_1)\rho(v_1)\rho'(v_1)\rho(v_2)\big[\mathcal{G}_{m-1}(v_1, v_2) - \mathcal{G}_{m+1}(v_1, v_2)\big] \; \mathrm{d}v_1$$

$$X_{ij}^{12} = \frac{1}{h_{\mathrm{v}}(v_2)} \int f_j^{\varphi}(v_1)\rho(v_1)h_{\mathrm{v}}(v_1)\Big(-\rho(v_1)z'(v_2)I_{\mathrm{d}}$$
$$+ \big[\rho(v_2)z'(v_2) - \rho'(v_2)[z(v_2) - z(v_1)]\big]I_{\mathrm{e}} \Big) \; \mathrm{d}v_1$$
$$= \int f_j^{\varphi}(v_1)\rho(v_1)h_{\mathrm{v}}(v_1)\Big(-2\rho(v_1)\mathcal{G}_m(v_1, v_2)$$
$$+ \rho(v_2)\big[\mathcal{G}_{m-1}(v_1, v_2) + \mathcal{G}_{m+1}(v_1, v_2)\big] \Big) \; \mathrm{d}v_1$$

$$X_{ij}^{21} = \int f_j^{\mathrm{v}}(v_1)\rho(v_1)\Big(-z'(v_1)\rho(v_2)I_{\mathrm{h}} + \big[\rho(v_1)z'(v_1) + \rho'(v_1)[z(v_2) - z(v_1)]\big]I_{\mathrm{e}}$$
$$- z'(v_1)\rho(v_2)I_{\mathrm{i}} \Big) \; \mathrm{d}v_1$$
$$= \int f_j^{\mathrm{v}}(v_1)\rho(v_1)\Big(-2z'(v_1)\rho(v_2)\mathcal{G}_m(v_1, v_2)$$
$$+ \big[\rho(v_1)z'(v_1) + \rho'(v_1)[z(v_2) - z(v_1)]\big]\big[\mathcal{G}_{m-1}(v_1, v_2) + \mathcal{G}_{m+1}(v_1, v_2)\big] \Big) \; \mathrm{d}v_1$$

$$X_{ij}^{22} = -\int f_j^{\varphi}(v_1)h_{\mathrm{v}}(v_1)\rho(v_1)\big[z(v_2) - z(v_1)\big]I_{\mathrm{f}} \; \mathrm{d}v_1$$
$$= -\mathrm{j} \int f_j^{\varphi}(v_1)h_{\mathrm{v}}(v_1)\rho(v_1)\big[z(v_2) - z(v_1)\big]\big[\mathcal{G}_{m-1}(v_1, v_2) - \mathcal{G}_{m+1}(v_1, v_2)\big] \; \mathrm{d}v_1$$

where the integrals $I_{\mathrm{a}} - I_{\mathrm{i}}$ are given in Appendix D and the Green functions are defined in (D.1).

Appendix G Matrix formulation of the integral equation

In this section equation (2.6), *i.e.*,

$$
j\omega\mu_0 \iint\limits_{S_{\mathrm{rad}}} \iint\limits_{S_{\mathrm{rad}}} \boldsymbol{\Psi}(\boldsymbol{r}_2) \cdot g(\boldsymbol{r}_1, \boldsymbol{r}_2) \boldsymbol{J}(\boldsymbol{r}_1) \, \mathrm{d}S_1 \, \mathrm{d}S_2
$$

$$
- j\frac{1}{\omega\epsilon_0} \iint\limits_{S_{\mathrm{rad}}} \iint\limits_{S_{\mathrm{rad}}} \left[\nabla_{2S} \cdot \boldsymbol{\Psi}(\boldsymbol{r}_2)\right] g(\boldsymbol{r}_1, \boldsymbol{r}_2) \left[\nabla_{1S} \cdot \boldsymbol{J}(\boldsymbol{r}_1)\right] \, \mathrm{d}S_1 \, \mathrm{d}S_2
$$

$$
- \iint\limits_{S_{\mathrm{rad}}} \iint\limits_{S_{\mathrm{rad}}} \boldsymbol{\Psi}(\boldsymbol{r}_2) \cdot \left[\nabla' g(\boldsymbol{r}_1, \boldsymbol{r}_2) \times \boldsymbol{M}(\boldsymbol{r}_1)\right] \, \mathrm{d}S_1 \, \mathrm{d}S_2 \qquad \text{(G.1)}
$$

$$
- \frac{1}{2} \iint\limits_{S_{\mathrm{rad}}} \left[\hat{\boldsymbol{n}}(\boldsymbol{r}_2) \times \boldsymbol{\Psi}(\boldsymbol{r}_2)\right] \cdot \boldsymbol{M}(\boldsymbol{r}_2) \, \mathrm{d}S_2 = 0
$$

$$
\Longleftrightarrow
$$

$$
j\omega\mu_0 \, I_4 - j\frac{1}{\omega\epsilon_0} \, I_5 - I_6 - \frac{1}{2} I_7 = 0
$$

is rewritten into a system of matrices. Start by writing I_4-I_7 as

$$
(I_4)_{ij} = Z_{ij}^{11\mathrm{A}} J_j^{\mathrm{v}} + Z_{ij}^{12\mathrm{A}} J_j^{\varphi}
$$
$$
(I_5)_{ij} = Z_{ij}^{11\mathrm{B}} J_j^{\mathrm{v}} + Z_{ij}^{12\mathrm{B}} J_j^{\varphi}
$$
$$
(I_6)_{ij} = X_{ij}^{11\mathrm{A}} M_j^{\mathrm{v}} + X_{ij}^{12\mathrm{A}} M_j^{\varphi}
$$
$$
(I_7)_{ij} = X_{ij}^{11\mathrm{B}} M_j^{\mathrm{v}} + X_{ij}^{12\mathrm{B}} M_j^{\varphi}
$$

when $\boldsymbol{\Psi} = \boldsymbol{\Psi}_{mi}^{\mathrm{v}}$ and

$$
(I_4)_{ij} = Z_{ij}^{21\mathrm{A}} J_j^{\mathrm{v}} + Z_{ij}^{22\mathrm{A}} J_j^{\varphi}
$$
$$
(I_5)_{ij} = Z_{ij}^{21\mathrm{B}} J_j^{\mathrm{v}} + Z_{ij}^{22\mathrm{B}} J_j^{\varphi}
$$
$$
(I_6)_{ij} = X_{ij}^{21\mathrm{A}} M_j^{\mathrm{v}} + X_{ij}^{22\mathrm{A}} M_j^{\varphi}
$$
$$
(I_7)_{ij} = X_{ij}^{21\mathrm{B}} M_j^{\mathrm{v}} + X_{ij}^{22\mathrm{B}} M_j^{\varphi}
$$

when $\boldsymbol{\Psi} = \boldsymbol{\Psi}_{mi}^{\varphi}$. The indices are $j = 1, \ldots, J$, where $J = N_{\mathrm{z}}$ and $i = 1, \ldots, I$, where $I = N_{\mathrm{z}}$. This give the matrix system,

$$
j\omega\mu_0 \, [I_4] - \frac{j}{\omega\epsilon_0} \, [I_5] - [I_6] - \frac{1}{2} \, [I_7] =
$$
$$
\begin{bmatrix} j\omega\mu_0 \left[Z^{11\mathrm{A}}\right] - \frac{j}{\omega\epsilon_0} \left[Z^{11\mathrm{B}}\right] & j\omega\mu_0 \left[Z^{12\mathrm{A}}\right] - \frac{j}{\omega\epsilon_0} \left[Z^{12\mathrm{B}}\right] \\ j\omega\mu_0 \left[Z^{21\mathrm{A}}\right] - \frac{j}{\omega\epsilon_0} \left[Z^{21\mathrm{B}}\right] & j\omega\mu_0 \left[Z^{22\mathrm{A}}\right] - \frac{j}{\omega\epsilon_0} \left[Z^{22\mathrm{B}}\right] \end{bmatrix} \begin{bmatrix} [J^{\mathrm{v}}] \\ [J^{\varphi}] \end{bmatrix}
$$
$$
+ \begin{bmatrix} -\left[X^{11\mathrm{A}}\right] - \frac{1}{2}\left[X^{11\mathrm{B}}\right] & -\left[X^{12\mathrm{A}}\right] - \frac{1}{2}\left[X^{12\mathrm{B}}\right] \\ -\left[X^{21\mathrm{A}}\right] - \frac{1}{2}\left[X^{21\mathrm{B}}\right] & -\left[X^{22\mathrm{A}}\right] - \frac{1}{2}\left[X^{22\mathrm{B}}\right] \end{bmatrix} \begin{bmatrix} [M^{\mathrm{v}}] \\ [M^{\varphi}] \end{bmatrix} = \begin{bmatrix} [0] \\ [0] \end{bmatrix}
$$

$$
\Longleftrightarrow
$$

$$\begin{bmatrix} [\mathcal{Z}^{11}] & [\mathcal{Z}^{12}] \\ [\mathcal{Z}^{21}] & [\mathcal{Z}^{22}] \end{bmatrix} \begin{bmatrix} [J^{\mathrm{v}}] \\ [J^{\varphi}] \end{bmatrix} + \begin{bmatrix} [\mathcal{X}^{11}] & [\mathcal{X}^{12}] \\ [\mathcal{X}^{21}] & [\mathcal{X}^{22}] \end{bmatrix} \begin{bmatrix} [M^{\mathrm{v}}] \\ [M^{\varphi}] \end{bmatrix} = \begin{bmatrix} [0] \\ [0] \end{bmatrix} \tag{G.2}$$

for all m. Expressions for the matrix elements $\left[\mathcal{Z}^{kl}\right]$ and $\left[X^{kl}\right]$ are derived in the next section.

G.1   The impedance matrices

For a given value of the index m, the impedance matrices in (G.2) are given by
$\mathcal{Z}_{ij}^{11} = \mathrm{j}\omega\mu_0 Z_{ij}^{11\mathrm{A}} - \frac{\mathrm{j}}{\omega\epsilon_0}Z_{ij}^{11\mathrm{B}}$ where

$$\begin{cases}
Z_{ij}^{11\mathrm{A}} = \iint f_i^{\mathrm{v}}(v_2)f_j^{\mathrm{v}}(v_1)\rho(v_2)\rho(v_1)\Big\{\rho'(v_2)\rho'(v_1)\,I_{\mathrm{B}} + z'(v_1)z'(v_2)\,I_{\mathrm{A}}\Big\}\,\mathrm{d}v_1\,\mathrm{d}v_2 \\[2mm]
\qquad = 4\pi \iint f_i^{\mathrm{v}}(v_2)f_j^{\mathrm{v}}(v_1)\rho(v_2)\rho(v_1) \\[2mm]
\qquad\qquad \cdot \Big\{\rho'(v_2)\rho'(v_1)\frac{g_{m-1}+g_{m+1}}{2} + z'(v_1)z'(v_2)g_m\Big\}\,\mathrm{d}v_1\,\mathrm{d}v_2 \\[2mm]
Z_{ij}^{11\mathrm{B}} = \iint \frac{\partial}{\partial v_2}\big[\rho(v_2)f_i^{\mathrm{v}}(v_2)\big]\frac{\partial}{\partial v_1}\big[\rho(v_1)f_j^{\mathrm{v}}(v_1)\big]\,I_{\mathrm{A}}\,\mathrm{d}v_1\,\mathrm{d}v_2 \\[2mm]
\qquad = 4\pi \iint \frac{\partial}{\partial v_2}\big[\rho(v_2)f_i^{\mathrm{v}}(v_2)\big]\frac{\partial}{\partial v_1}\big[\rho(v_1)f_j^{\mathrm{v}}(v_1)\big]\,g_m\,\mathrm{d}v_1\,\mathrm{d}v_2
\end{cases}$$

and $\mathcal{Z}_{ij}^{12} = \mathrm{j}\omega\mu_0 Z_{ij}^{12\mathrm{A}} - \frac{\mathrm{j}}{\omega\epsilon_0}Z_{ij}^{12\mathrm{B}}$ where

$$\begin{cases}
Z_{ij}^{12\mathrm{A}} = -\iint f_i^{\mathrm{v}}(v_2)f_j^{\varphi}(v_1)\rho'(v_2)\rho(v_2)\rho(v_1)h_{\mathrm{v}}(v_1)\,I_{\mathrm{C}}\,\mathrm{d}v_1\,\mathrm{d}v_2 \\[2mm]
\qquad = -\mathrm{j}\,4\pi \iint f_i^{\mathrm{v}}(v_2)f_j^{\varphi}(v_1)\rho'(v_2)\rho(v_2)\rho(v_1)h_{\mathrm{v}}(v_1)\frac{g_{m-1}-g_{m+1}}{2}\,\mathrm{d}v_1\,\mathrm{d}v_2 \\[2mm]
Z_{ij}^{12\mathrm{B}} = \mathrm{j}\,m \iint \frac{\partial}{\partial v_2}\big[\rho(v_2)f_i^{\mathrm{v}}(v_2)\big]f_j^{\varphi}(v_1)h_{\mathrm{v}}(v_1)\,I_{\mathrm{A}}\,\mathrm{d}v_1\,\mathrm{d}v_2 \\[2mm]
\qquad = \mathrm{j}\,4\pi m \iint \frac{\partial}{\partial v_2}\big[\rho(v_2)f_i^{\mathrm{v}}(v_2)\big]f_j^{\varphi}(v_1)h_{\mathrm{v}}(v_1)g_m\,\mathrm{d}v_1\,\mathrm{d}v_2
\end{cases}$$

and $\mathcal{Z}_{ij}^{21} = \mathrm{j}\omega\mu_0 Z_{ij}^{21\mathrm{A}} - \frac{\mathrm{j}}{\omega\epsilon_0}Z_{ij}^{21\mathrm{B}}$ where

$$\begin{cases}
Z_{ij}^{21\mathrm{A}} = \iint f_i^{\varphi}(v_2)f_j^{\mathrm{v}}(v_1)\rho(v_1)\rho'(v_1)\rho(v_2)h_{\mathrm{v}}(v_2)\,I_{\mathrm{C}}\,\mathrm{d}v_1\,\mathrm{d}v_2 \\[2mm]
\qquad = \mathrm{j}\,4\pi \iint f_i^{\varphi}(v_2)f_j^{\mathrm{v}}(v_1)\rho(v_1)\rho'(v_1)\rho(v_2)h_{\mathrm{v}}(v_2)\frac{g_{m-1}-g_{m+1}}{2}\,\mathrm{d}v_1\,\mathrm{d}v_2 \\[2mm]
Z_{ij}^{21\mathrm{B}} = -\mathrm{j}m \iint f_i^{\varphi}(v_2)h_{\mathrm{v}}(v_2)\frac{\partial}{\partial v_1}\big[\rho(v_1)f_j^{\mathrm{v}}(v_1)\big]\,I_{\mathrm{A}}\,\mathrm{d}v_1\,\mathrm{d}v_2 \\[2mm]
\qquad = -\mathrm{j}\,4\pi m \iint f_i^{\varphi}(v_2)h_{\mathrm{v}}(v_2)\frac{\partial}{\partial v_1}\big[\rho(v_1)f_j^{\mathrm{v}}(v_1)\big]\,g_m\,\mathrm{d}v_1\,\mathrm{d}v_2
\end{cases}$$

and $\mathcal{Z}_{ij}^{22} = \mathrm{j}\omega\mu_0 Z_{ij}^{22\mathrm{A}} - \frac{\mathrm{j}}{\omega\epsilon_0} Z_{ij}^{22\mathrm{B}}$ where

$$
\begin{cases}
Z_{ij}^{22\mathrm{A}} = \iint f_i^\varphi(v_2) f_j^\varphi(v_1) \rho(v_2) h_\mathrm{v}(v_2) \rho(v_1) h_\mathrm{v}(v_1)\, I_\mathrm{B}\, \mathrm{d}v_1\, \mathrm{d}v_2 \\[2mm]
\qquad = 4\pi \iint f_i^\varphi(v_2) f_j^\varphi(v_1) \rho(v_2) h_\mathrm{v}(v_2) \rho(v_1) h_\mathrm{v}(v_1) \dfrac{g_{m-1} + g_{m+1}}{2}\, \mathrm{d}v_1\, \mathrm{d}v_2 \\[3mm]
Z_{ij}^{22\mathrm{B}} = m^2 \iint f_i^\varphi(v_2) f_j^\varphi(v_1) h_\mathrm{v}(v_2) h_\mathrm{v}(v_1)\, I_\mathrm{A}\, \mathrm{d}v_1\, \mathrm{d}v_2 \\[2mm]
\qquad = 4\pi m^2 \iint f_i^\varphi(v_2) f_j^\varphi(v_1) h_\mathrm{v}(v_2) h_\mathrm{v}(v_1)\, g_m\, \mathrm{d}v_1\, \mathrm{d}v_2
\end{cases}
$$

and $\mathcal{X}_{ij}^{11} = -X_{ij}^{11\mathrm{A}} - \frac{1}{2}X_{ij}^{11\mathrm{B}}$ where

$$
\begin{cases}
X_{ij}^{11\mathrm{A}} = \iint f_j^\mathrm{v}(v_1) f_i^\mathrm{v}(v_2) \rho(v_1)\rho(v_2) \\[2mm]
\qquad \cdot \big[-\rho(v_1)z'(v_1)\rho'(v_2) - \rho'(v_1)\rho'(v_2)\big[z(v_2) - z(v_1)\big] + \rho'(v_1)\rho(v_2)z'(v_2)\big] I_\mathrm{F}\, \mathrm{d}v_1\, \mathrm{d}v_2 \\[2mm]
\qquad = 4\pi\mathrm{j} \iint f_j^\mathrm{v}(v_1) f_i^\mathrm{v}(v_2) \rho(v_1)\rho(v_2) \\[2mm]
\qquad \cdot \Big\{-\rho(v_1)z'(v_1)\rho'(v_2) - \rho'(v_1)\rho'(v_2)\big[z(v_2) - z(v_1)\big] + \rho'(v_1)\rho(v_2)z'(v_2)\Big\} \\[2mm]
\qquad \cdot \dfrac{\mathfrak{g}_{m-1}(v_1, v_2) - \mathfrak{g}_{m+1}(v_1, v_2)}{2}\, \mathrm{d}v_1\, \mathrm{d}v_2 \\[2mm]
X_{ij}^{11\mathrm{B}} = 0
\end{cases}
$$

and $\mathcal{X}_{ij}^{12} = -X_{ij}^{12\mathrm{A}} - \frac{1}{2}X^{12\mathrm{B}}$ where

$$
\begin{cases}
X_{ij}^{12\mathrm{A}} = \iint f_j^\varphi(v_1) f_i^\mathrm{v}(v_2) \rho(v_1)\rho(v_2) h_\mathrm{v}(v_1) \Big(-\rho(v_1)z'(v_2) I_\mathrm{D} \\[2mm]
\qquad + \big[\rho(v_2)z'(v_2) - \rho'(v_2)[z(v_2) - z(v_1)]\big] I_\mathrm{E}\Big)\, \mathrm{d}v_1\, \mathrm{d}v_2 \\[2mm]
\qquad = 4\pi \iint f_j^\varphi(v_1) f_i^\mathrm{v}(v_2) \rho(v_1)\rho(v_2) h_\mathrm{v}(v_1) \Big(-\rho(v_1)z'(v_2)\, \mathfrak{g}_m\,(v_1, v_2) \\[2mm]
\qquad + \big[\rho(v_2)z'(v_2) - \rho'(v_2)[z(v_2) - z(v_1)]\big] \dfrac{\mathfrak{g}_{m-1}(v_1, v_2) + \mathfrak{g}_{m+1}(v_1, v_2)}{2}\Big)\, \mathrm{d}v_1\, \mathrm{d}v_2 \\[2mm]
X_{ij}^{12\mathrm{B}} = -2\pi \int f_i^\mathrm{v}(v_2) f_j^\varphi(v_2) \rho(v_2) h_\mathrm{v}(v_2)\, \mathrm{d}v_2
\end{cases}
$$

and $\mathcal{X}_{ij}^{21} = -X_{ij}^{21A} - \frac{1}{2}X_{ij}^{21B}$ where

$$
\begin{cases}
X_{ij}^{21A} = \iint f_j^{\mathrm{v}}(v_1)f_i^{\varphi}(v_2)\rho(v_1)\rho(v_2)h_{\mathrm{v}}(v_2)\Big(-z'(v_1)\rho(v_2)I_{\mathrm{H}} \\
\qquad\qquad + \big[\rho(v_1)z'(v_1)+\rho'(v_1)[z(v_2)-z(v_1)]\big]I_{\mathrm{E}} - z'(v_1)\rho(v_2)I_{\mathrm{I}}\Big)\,\mathrm{d}v_1\,\mathrm{d}v_2 \\
\qquad = 4\pi\iint f_j^{\mathrm{v}}(v_1)f_i^{\varphi}(v_2)\rho(v_1)\rho(v_2)h_{\mathrm{v}}(v_2)\Big(-z'(v_1)\rho(v_2)\,\mathfrak{g}_m\,(v_1,v_2) \\
\qquad\qquad + \big[\rho(v_1)z'(v_1)+\rho'(v_1)[z(v_2)-z(v_1)]\big]\dfrac{\mathfrak{g}_{m-1}(v_1,v_2)+\mathfrak{g}_{m+1}(v_1,v_2)}{2}\Big)\,\mathrm{d}v_1\,\mathrm{d}v_2 \\
X_{ij}^{21B} = 2\pi\displaystyle\int f_i^{\varphi}(v_2)f_j^{\mathrm{v}}(v_2)\rho(v_2)h_{\mathrm{v}}(v_2)\,\mathrm{d}v_2
\end{cases}
$$

and $\mathcal{X}_{ij}^{22} = -X_{ij}^{22A} - \frac{1}{2}X_{ij}^{22B}$ where

$$
\begin{cases}
X_{ij}^{22A} = -\iint f_j^{\varphi}(v_1)f_i^{\varphi}(v_2)\rho(v_1)\rho(v_2)h_{\mathrm{v}}(v_1)h_{\mathrm{v}}(v_2)\big[z(v_2)-z(v_1)\big]I_{\mathrm{F}}\,\mathrm{d}v_1\,\mathrm{d}v_2 \\
\qquad = -4\pi\mathrm{j}\iint f_j^{\varphi}(v_1)f_i^{\varphi}(v_2)\rho(v_1)\rho(v_2)h_{\mathrm{v}}(v_1)h_{\mathrm{v}}(v_2)\big[z(v_2)-z(v_1)\big] \\
\qquad\qquad \cdot \dfrac{\mathfrak{g}_{m-1}(v_1,v_2)-\mathfrak{g}_{m+1}(v_1,v_2)}{2}\,\mathrm{d}v_1\,\mathrm{d}v_2 \\
X_{ij}^{22B} = 0
\end{cases}
$$

where the integrals $I_{\mathrm{A}} - I_{\mathrm{I}}$ are given in Appendix D and the Green functions are singular versions of the ones defined in (D.1). The numerical treatment of the singularities in the integrals is addressed in Appendix E.

References

[1] R. A. Adams. *Calculus: a complete course.* Addison-Wesley, Reading, MA, USA, third edition, 1995.

[2] M. Andersson. Software for analysis of radome performance. In *Proc. International Conference on Electromagnetics in Advanced Applications (ICEAA'05),* pages 537–539, Torino, Italy, 2005.

[3] R. Aster, B. Borchers, and C. Thurber. *Parameter Estimation and Inverse Problems.* Academic Press, New York, 2005.

[4] C. A. Balanis. *Antenna Theory.* John Wiley & Sons, New York, second edition, 1997.

[5] C. A. Balanis. *Advanced Engineering Electromagnetics.* John Wiley & Sons, New York, 1989.

[6] A. Bondeson, T. Rylander, and P. Ingelström. *Computational Electromagnetics*. Springer-Verlag, Berlin, 2005.

[7] C. Cappellin, O. Breinbjerg, and A. Frandsen. Properties of the transformation from the spherical wave expansion to the plane wave expansion. *Radio Sci.*, **43**(1), 2008.

[8] C. Cappellin, A. Frandsen, and O. Breinbjerg. Application of the SWE-to-PWE antenna diagnostics technique to an offset reflector antenna. *IEEE Antennas and Propagation Magazine*, **50**(5), 204–213, 2008.

[9] D. Colton and R. Kress. *Integral Equation Methods in Scattering Theory*. John Wiley & Sons, New York, 1983.

[10] L. E. Corey and E. B. Joy. On computation of electromagnetic fields on planar surfaces from fields specified on nearby surfaces. *IEEE Trans. Antennas Propagat.*, **29**(2), 402–404, 1981.

[11] T. F. Eibert and C. H. Schmidt. Multilevel fast multipole accelerated inverse equivalent current method employing Rao-Wilton-Glisson discretization of electric and magnetic surface currents. *IEEE Trans. Antennas Propagat.*, **57**(4), 1178–1185, 2009.

[12] J. Fridén, H. Isaksson, B. Hansson, and B. Thors. Robust phase-retrieval for quick whole-body SAR assessment using dual plane amplitude-only data. *Electronics Letters*, **45**(23), 1155–1157, 2009.

[13] M. G. Guler and E. B. Joy. High resolution spherical microwave holography. *IEEE Trans. Antennas Propagat.*, **43**(5), 464–472, 1995.

[14] J. E. Hansen, editor. *Spherical Near-Field Antenna Measurements*. Number 26 in IEE electromagnetic waves series. Peter Peregrinus Ltd., Stevenage, UK, 1988. ISBN: 0-86341-110-X.

[15] D. S. Jones. *Acoustic and Electromagnetic Waves*. Oxford University Press, New York, 1986.

[16] D. S. Jones. *Methods in Electromagnetic Wave Propagation*. IEEE Press, Piscataway, NJ, second edition, 1994.

[17] R. E. Kleinman and G. F. Roach. Boundary integral equations for the three-dimensional Helmholtz equation. *SIAM Review*, **16**(2), 214–236, 1974.

[18] J. A. Kong. *Electromagnetic Wave Theory*. John Wiley & Sons, New York, 1986.

[19] D. J. Kozakoff. *Analysis of Radome-Enclosed Antennas*. Artech House, Boston, London, 1997.

[20] R. Kress. *Linear Integral Equations.* Springer-Verlag, Berlin Heidelberg, second edition, 1999.

[21] G. Kristensson. *Elektromagnetisk vågutbredning.* Studentlitteratur, Lund, 1999. (In Swedish).

[22] F. Las-Heras, B. Galocha, and Y. Alvarez. On the sources reconstruction method application for array and aperture antennas diagnostics. *Microwave Opt. Techn. Lett.*, **51**(7), 1664–1668, 2009.

[23] F. Las-Heras, M. R. Pino, S. Loredo, Y. Alvarez, and T. K. Sarkar. Evaluating near-field radiation patterns of commercial antennas. *IEEE Trans. Antennas Propagat.*, **54**(8), 2198–2207, 2006.

[24] J.-J. Laurin, J.-F. Zürcher, and F. E. Gardiol. Near-field diagnostics of small printed antennas using the equivalent magnetic current approach. *IEEE Trans. Antennas Propagat.*, **49**(5), 814–828, 2001.

[25] J. Lee, E. M. Ferren, D. P. Woollen, and K. M. Lee. Near-field probe used as a diagnostic tool to locate defective elements in an array antenna. *IEEE Trans. Antennas Propagat.*, **36**(6), 884–889, 1988.

[26] E. A. Marengo and A. J. Devaney. The inverse source problem of electromagnetics: Linear inversion formulation and minimum energy solution. *IEEE Trans. Antennas Propagat.*, **47**(2), 410–412, February 1999.

[27] J. R. Mautz and R. F. Harrington. Radiation and scattering from bodies of revolution. *Appl. Scientific Research*, **20**(1), 405–435, 1969.

[28] N. Morita, N. Kumagai, and J. R. Mautz. *Integral Equation Methods for Electromagnetics.* Artech House, Boston, London, 1990.

[29] C. Müller. *Foundations of the Mathematical Theory of Electromagnetic Waves.* Springer-Verlag, Berlin, 1969.

[30] M. Nieto-Vesperinas. *Scattering and diffraction in physical optics.* World Scientific Publisher, Singapore, second edition, 2006.

[31] S. Nordebo, M. Gustafsson, and K. Persson. Sensitivity analysis for antenna near-field imaging. *IEEE Trans. Signal Process.*, **55**(1), 94–101, January 2007.

[32] K. Persson and M. Gustafsson. Reconstruction of equivalent currents using a near-field data transformation – with radome applications. *Progress in Electromagnetics Research*, **54**, 179–198, 2005.

[33] K. Persson and M. Gustafsson. Reconstruction of equivalent currents using the scalar surface integral representation. Technical Report LUTEDX/(TEAT-7131)/1–25/(2005), Lund University, Department of Electrical and Information Technology, P.O. Box 118, S-221 00 Lund, Sweden, 2005. http://www.eit.lth.se.

[34] A. F. Peterson, S. L. Ray, and R. Mittra. *Computational Methods for Electromagnetics.* IEEE Press, New York, 1998.

[35] A. J. Poggio and E. K. Miller. Integral equation solutions of three-dimensional scattering problems. In R. Mittra, editor, *Computer Techniques for Electromagnetics.* Pergamon, New York, 1973.

[36] Y. Rahmat-Samii, L. I. Williams, and R. G. Yaccarino. The UCLA bi-polar planar-near-field antenna-measurement and diagnostics range. *IEEE Antennas and Propagation Magazine*, **37**(6), 16–35, December 1995.

[37] D. J. Rochblatt and B. L. Seidel. Microwave antenna holography. *IEEE Trans. Microwave Theory Tech.*, **40**(6), 1294–1300, 1992.

[38] T. K. Sarkar and A. Taaghol. Near-field to near/far-field transformation for arbitrary near-field geometry utilizing an equivalent electric current and MoM. *IEEE Trans. Antennas Propagat.*, **47**(3), 566–573, March 1999.

[39] J. A. Shifflett. CADDRAD: A physical opics radar/radome analysis code for arbitrary 3D geometries. *IEEE Antennas and Propagation Magazine*, **6**(39), 73–79, 1997.

[40] R. A. Shore and A. D. Yaghjian. Dual surface electric field integral equation. Air Force Research Laboratory Report, 2001. No. AFRL-SN-HS-TR-2001-013.

[41] R. A. Shore and A. D. Yaghjian. Dual-surface integral equations in electromagnetic scattering. *IEEE Trans. Antennas Propagat.*, **53**(5), 1706–1709, 2005.

[42] S. Silver. *Microwave Antenna Theory and Design*, volume 12 of *Radiation Laboratory Series.* McGraw-Hill, New York, 1949.

[43] J. Song and W. Chew. FMM and MLFMA in 3-D and fast Illinois solver code. In W. Chew, J.-M. Jin, E. Michielssen, and J. Song, editors, *Fast and Efficient Algorithms in Computational Electromagnetics*, pages 77–118. Artech House, 2001.

[44] J. C.-E. Sten and E. A. Marengo. Inverse source problem in the spheroidal geometry: Vector formulation. *IEEE Trans. Antennas Propagat.*, **56**(4), 961–969, 2008.

[45] G. Strang. *Introduction to applied mathematics.* Wellesley-Cambridge Press, Box 157, Wellesley MA 02181, 1986.

[46] S. Ström. Introduction to integral representations and integral equations for time-harmonic acoustic, electromagnetic and elastodynamic wave fields. In V. V. Varadan, A. Lakhtakia, and V. K. Varadan, editors, *Field Representations and Introduction to Scattering*, volume 1 of *Handbook on Acoustic, Electromagnetic and Elastic Wave Scattering*, chapter 2, pages 37–141. Elsevier Science Publishers, Amsterdam, 1991.

[47] F. Thérond, J. C. Bolomey, N. Joachmowicz, and F. Lucas. Electromagnetic diagnosis technique using spherical near-field probing. In *Proc. EUROEM'94*, pages 1218–1226, Bordeaux, France, 1994.

[48] J. G. van Bladel. *Electromagnetic Fields*. IEEE Press, New York, 2007.

[49] A. D. Yaghjian. An overview of near-field antenna measurements. *IEEE Trans. Antennas Propagat.*, **34**(1), 30–45, January 1986.

[50] A. Ziyyat, L. Casavola, D. Picard, and J. C. Bolomey. Prediction of BTS antennas safety perimeter from NF to NF transformation: an experimental validation. In *Proc. Antenna Measurement Techniques Association (AMTA)*, pages 22–26, Denver, US, 2001.